POLITECNICO
MILANO 1863

SCUOLA DI INGEGNERIA INDUSTRIALE
E DELL'INFORMAZIONE

Control of an Over-Actuated Vehicle for Autonomous Driving and Energy Optimization

Development of a cascade controller to solve the control allocation problem in real-time on autonomous driving vehicle

GIANMARCO GRANDI

Tesi di Laurea Magistrale in Automation and Control Engineering - Ingegneria dell'Automazione

Student ID: 952604
Advisor: Prof. Luca Bascetta
Co-advisors: Prof. Mikael Nybacka
Academic Year: 2021-22

Abstract

An over-actuated vehicle is a system that presents more control variables than degrees of freedom. Therefore, more than one configuration of the control input can drive the system to a desired state in the state space, and this redundancy can be exploited to fulfill other tasks or solve further problems. In particular, nowadays, challenges concerning electric vehicles regarding their autonomy and solutions to reduce energy consumption are becoming more and more attractive. OA vehicles, on this problem, offer the possibility of using the redundancy to choose the control input, among possible ones, so as to minimize energy consumption.

In this regard, the research objective is to investigate different techniques to control, in real-time, an over-actuated autonomous driving vehicle to guarantee trajectory following and stability with the aim of minimizing energy consumption. The research project focuses on a vehicle able to drive and steer the four wheels (4WD, 4WS) independently. This work extends the contribution of previous theoretical energy-based research developed by providing a control algorithm that must work in real-time on a prototype vehicle (RCV-E) developed at the ITRL within KTH with the over-actuation investigated. To this end, the control algorithm has to balance the complexity of a multi-input system, the optimal allocation objectives, and the agility to run in real-time on the MicroAutoBox II - dSPACE system mounted on the vehicle.

The solution proposed is a two-level controller which handles separately high and low-rate dynamics with an adequate level of complexity. The upper level is responsible for trajectory following and energy minimization. The allocation problem is solved in two steps. An LTV-MPC solves the trajectory-following problem and allocates the forces at the wheels considering the wheel energy losses due to longitudinal and lateral sliding. The second step re-allocates the longitudinal forces between the front and rear axles by considering each vehicle side independently to minimize energy loss in the motors. The lower level is responsible for transforming the forces at the wheels into torques and steering angles; it runs at a faster rate than the upper level to account for the high-frequency dynamics of the wheels.

Last, the overall control strategy is tested in simulation concerning the trajectory-following and energy minimization performance, and after on MircoAutoBox II mounted on the RCV-E to assess the real-time performance.

Keywords

LTV-MPC (Linear Time-Varying Model Predictive Controller), Trajectory following, Energy consumption, Vehicle stability, Vehicle model, Real-time performance.

Sommario

Un veicolo sovra-attuato è un sistema che presenta più variabili di controllo che gradi di libertà. Pertanto, più di una configurazione dell'ingresso di controllo può portare il sistema a uno stato desiderato nello spazio degli stati e questa ridondanza può essere sfruttata per svolgere altri compiti o risolvere ulteriori problemi. In particolare, al giorno d'oggi le sfide relative ai veicoli elettrici per quanto riguarda la loro autonomia e le soluzioni per ridurre il consumo energetico stanno diventando sempre più interessanti. I veicoli sovra-attuati, riguardo a questo problema, offrono la possibilità di utilizzare la ridondanza per scegliere l'ingresso di controllo, tra quelli possibili, che minimizza i consumi energetici.
A questo proposito, l'obiettivo della ricerca è studiare diverse tecniche per controllare, in tempo reale, un veicolo a guida autonoma sovra-attuato per garantire l'inseguimento della traiettoria e la stabilità con l'obiettivo di minimizzare il consumo energetico.
Questo studio si concentra su un veicolo in grado di guidare e sterzare le quattro ruote (4WD, 4WS) in modo indipendente, ed estende il contributo delle precedenti ricerche teoriche fornendo un algoritmo di controllo che deve funzionare in tempo reale su un prototipo di veicolo (RCV-E) sviluppato presso l'ITRL all'interno del KTH, che presenta la sovra-attuazione studiata. A tal fine, l'algoritmo di controllo deve bilanciare la complessità di un sistema a più ingressi, gli obiettivi di allocazione dell'azione di controllo ottimale e l'agilità di funzionamento in tempo reale sul sistema MicroAutoBox II - dSPACE montato sul veicolo.
La soluzione proposta è un controllore a due livelli che gestisce separatamente le dinamiche ad alta e bassa frequenza. Il livello superiore è responsabile dell'inseguimento della traiettoria e della minimizzazione dell'energia. Il problema di allocazione viene risolto in due fasi. Un LTV-MPC risolve il problema dell'inseguimento della traiettoria e assegna le forze alle ruote tenendo conto delle perdite di energia agli pneumatici dovute al loro scorrimento longitudinale e laterale. Il secondo passo rialloca le forze longitudinali tra l'asse anteriore e quello posteriore considerando ciascun lato del veicolo in modo indipendente per minimizzare le perdite di energia nei motori. Il livello inferiore è responsabile della trasformazione delle forze alle ruote in coppia e angolo di sterzo; funziona a una più alta frequenza rispetto al livello superiore per tenere conto delle dinamiche veloci delle ruote.
Infine, la strategia di controllo viene testata in simulazione per quanto riguarda le prestazioni di inseguimento della traiettoria e di minimizzazione

dell'energia, e successivamente su MircoAutoBox II montato sull'RCV-E per valutare le prestazioni in tempo reale.

Parole chiave

LTV-MPC (Controllo a predizione del modello lineare tempo variabile), Inseguimento di traiettoria, Consumo energetico, Stabilità del veicolo, Modello del veicolo, Prestazioni in tempo reale.

Acknowledgments

This research project concludes an academic journey I had longed for even before starting university; therefore, I would like to dedicate this work to all the people who have supported me over these years.
I would like to sincerely thank my supervisor Prof. Mikael Nybacka, from KTH Royal Institute of Technology, for the opportunity I received to investigate this topic and for guiding me in carrying out this project.
I would like to express my gratitude to Prof. Luca Bascetta, from Politecnico di Milano, who guided me throughout the double degree experience and this research project.
A big thank you goes to Wenliang Zhang and Lin Zhao, from KTH Royal Institute of Technology, for their advice and assistance throughout my research.
I also wish to express my thankfulness to Prof. Jonas Mårtensson, from KTH Royal Institute of Technology, for his availability to act as my examiner.
I wish also to acknowledge the help provided by Daniel Arnström and Jacob Röing to help me finalize this project.
My most profound gratitude goes to my parents. They kept me motivated throughout the path I chose for myself and helped me to secure my future.
My gratitude also goes to my friends, who have been close to me despite the distance and with whom I have spent beautiful moments during these years.
Finally, a special thank you goes to my grandparents, uncles, and cousins for their support and love over the years.

Milan, April 2023
Gianmarco Grandi

Contents

1 Introduction **1**
1.1 Background . . . 1
1.1.1 Trajectory following and autonomous driving . . . 1
1.1.2 Over-actuated vehicle . . . 2
1.1.3 KTH-Research Concept Vehicle (KTH-RCV) . . . 4
1.1.4 Importance of energy optimization . . . 5
1.2 Problem . . . 6
1.2.1 Research question . . . 6
1.2.2 Hypothesis . . . 6
1.3 Purpose . . . 7
1.3.1 Social, ethical and environmental aspects . . . 7
1.4 Goals . . . 8
1.5 Research Methodology . . . 8
1.6 Delimitations . . . 9
1.7 Structure of the thesis . . . 10

2 Related works **11**
2.1 Over-actuation control . . . 11
2.2 Over-actuation at KTH with a focus on energy optimization . . . 13
2.3 Over-Actuated vehicles with a focus on energy optimization . . . 15
2.4 Vehicle stability . . . 16
2.4.1 Over-actuation for stability purposes . . . 17
2.5 Over-actuation for stability and energy minimization purposes 19

3 Analysis of the control tasks **21**
3.1 Simulation environment . . . 21
3.2 Trajectory following strategy . . . 22
3.2.1 How the controller performs trajectory following . . . 24
3.3 Sources of power consumption . . . 29

3.3.1 Comparison of Power losses . . . 33
3.4 Stability Considerations . . . 36
3.4.1 Rollover stability . . . 36
3.4.2 Yaw Stability . . . 37
3.4.3 Wheel Stability . . . 38

4 System model **39**
4.1 Vehicle model . . . 39
4.2 Tire model . . . 43

5 Trajectory-following control strategy **51**
5.1 LTV-MPC for trajectory-following . . . 52
5.2 Two-level control strategy . . . 53
5.3 Results . . . 59
5.4 Integral action on the the longitudinal velocity . . . 64

6 Energy minimization control strategy **69**
6.1 Control strategy . . . 69
6.2 Results on energy minimization . . . 72

7 Implementation on the RCV **78**
7.1 Implementation of the LTV-MPC in dSPACE . . . 78
7.2 Real-time performance of the controller . . . 80

8 Conclusions and Future works **81**
8.1 Conclusions . . . 81
8.1.1 Trajectory-following . . . 81
8.1.2 Energy minimization . . . 82
8.1.3 Real-time performance . . . 83
8.2 Future works . . . 83

References **85**

A RCV's engine efficiency characteristic **97**

B LTV-MPC equations **99**

C Energy minimization strategy: full simulation results tables **104**

List of Figures

1.1 RCV-E developed at the ITRL within KTH. 5

3.1 Side view of the test vehicle in simulation. 22
3.2 Representation of path moving sideways. 23
3.3 Trajectory specification. 24
3.4 Trajectory sampling over the prediction horizon. 25
3.5 Vehicle lateral deviation from the trajectory. 27
3.6 Different road profiles. a) Is a road where the vehicle follows different profiles of velocity. b) Is a straight road where the vehicle accelerates, travels at constant speed, and then brakes. c) Is a circle road, where steady state cornering is investigated. 35

4.1 Vehicle state representation. 40
4.2 Forces acting on the Center of Gravity (CoG) of the car. 41
4.3 Forces acting on the wheels. 42
4.4 Longitudinal tire forces representation. a) Represents the acceleration and braking phase at $5\ m/s^2$ and $-8\ m/s^2$ for the left front and rear wheels. The right side is symmetrical because the car was driving straight. b) Represents the braking phase at $-10\ m/s^2$ for the left front and rear wheels. In these figures, the linear model is not represented because it has a divergent behaviour and was out of scale. 47
4.5 Longitudinal tire forces representation during steady-state straight driving at $100\ km/h$. The linear and Dugoff models are superimposed in the figures. 48
4.6 Lateral tire forces representation. a) Shows the lateral tire forces estimation during steady-state cornering. b) Shows the lateral tire forces estimation during a "snake" section. 50

5.1 MPC prediction. Sampling time 0.1s, initial speed 5 m/s, wheel torque 100Nm, front steering angles 0.1 rad, rear steering angles -0.05 rad. 54
5.2 MPC prediction. Sampling time 0.02s, initial speed 5 m/s, wheel torque 100Nm, front steering angles 0.1 rad, rear steering angles -0.05 rad. 55
5.3 MPC prediction. Sampling time 0.1s, initial speed 4 m/s, wheel torque 100N, front steering angle 0.1 rad, rear steering angle -0.05 rad. 56
5.4 Structure of the controller. 57
5.5 Two-level model. a) Is the model utilized by the LTV-MPC. b) Is the model utilized by the lower level controller to allocate the forces for each wheel. 58
5.6 Friction circle constraint applied to the wheel's forces in the vehicle's reference frame. 59
5.7 Vehicle velocity and reference velocity during Straight driving maneuver. 64
5.8 System structure with the integral action to the LTV-MPC. . . 64

6.1 System structure with the engine energy optimization step. . . 71
6.2 Comparison of the tire longitudinal slip ratio during maneuver d) when the vehicle weight distribution is considered b) and when it is not a). 75
6.3 Comparison of the tire sideslip angles during maneuver e) when the vehicle weight distribution is considered b) and when it is not a). 75

A.1 RCV-E PMSM efficiency map. 97
A.2 Variation of the RCV-E engines efficiency map for the Tesla motors used in simulation. 98

List of Tables

3.1 Vehicle parameters. 22
3.2 Vehicle parameters in IPG CarMaker for the energy tests. . . . 34
3.3 Energy consumed due to longitudinal slip, cornering resistance, and engine efficiency in different maneuvers. 35
3.4 Vehicle parameters for the maximum lateral acceleration of the car before experiencing rollover. 37

4.1 Vehicle parameters in IPG CarMaker for the tire forces experiment. 43
4.2 RMSE of the longitudinal tire forces compared to the measured ones in IPG CarMaker. The RMSE in the table is the average between the RMSEs computed for each wheel. . . 45
4.3 RMSE of the lateral tire forces compared to the measured ones in IPG CarMaker. The RMSE in the table is the average between the RMSEs computed for each wheel. 48

5.1 Eigenvalue of the system $[v_x, v_y, \dot{\theta}]$ linearized in different points. 56
5.2 Results of the two-level controller for the trajectory following performance on the Mix Road Fig. 3.6a. 61
5.3 Results of the two-level controller for the trajectory following performance on the Straight Road Fig. 3.6b. 61
5.4 Results of the two-level controller for the trajectory following performance for steady-state cornering condition long 80 m on the Circle Road Fig. 3.6c. 62
5.5 Steady-state velocity of the vehicle during straight driving and cornering. During straight driving the reference velocity is 130 km/h, during cornering is 50 km/h. 63

5.6 Steady-state velocity of the vehicle during straight driving and cornering when an integral action is applied. During straight driving the reference velocity is 130 km/h, during cornering is 50 km/h. The Yaw Max value is the maximum yaw angle that the vehicle has during hard braking from 130 km/h to 0 km/h. 67

6.1 Energy consumed by the LTV-MPC with parameters (Th=1.5 s, Ts=0.15 s, N=10) during the different Maneuvers a)-e). Three cases are reported: B) the base version with no energy minimization implementation, W) when only the vehicle's weight distribution is considered, E) when also the engine efficiency optimization is included. 77

7.1 Execution time of the controller on dSPACE - MicroAutoBox II. 80

C.1 Energy consumed by the LTV-MPC with different combinations of the prediction horizon during Maneuver a). Three cases are reported: B) the base version with no energy minimization implementation, W) when only the vehicle's weight distribution is considered, E) when also the engine efficiency optimization is included. 105

C.2 Energy consumed by the LTV-MPC with different combinations of the prediction horizon during Maneuver b). Three cases are reported: B) the base version with no energy minimization implementation, W) when only the vehicle's weight distribution is considered, E) when also the engine efficiency optimization is included. 106

C.3 Energy consumed by the LTV-MPC with different combinations of the prediction horizon during Maneuver c). Three cases are reported: B) the base version with no energy minimization implementation, W) when only the vehicle's weight distribution is considered, E) when also the engine efficiency optimization is included. 107

C.4 Energy consumed by the LTV-MPC with different combinations of the prediction horizon during Maneuver d). Three cases are reported: B) the base version with no energy minimization implementation, W) when only the vehicle's weight distribution is considered, E) when also the engine efficiency optimization is included. 108

C.5 Energy consumed by the LTV-MPC with different combinations of the prediction horizon during Maneuver e). Three cases are reported: B) the base version with no energy minimization implementation, W) when only the vehicle's weight distribution is considered, E) when also the engine efficiency optimization is included. 109

List of acronyms and abbreviations

4WB	Four-Wheel Braking
4WD	Four-Wheel Driving
4WS	Four-Wheel Steering
ABS	Anti-lock Braking System
AFS	Active Front-wheel Steering
API	Application programming interface
CA	Control Allocation
CoG	Center of Gravity
DoF	Degree of Freedom
DT	Direct Torque model
DYC	Direct Yaw moment Control
ESC	Electronic Stability Control
EV	Electric Vehicle
ITRL	Integrated Transport Research Lab
KTH	Kungliga Tekniska Högskolan - Royal Institute of Technology
LD	Lateral Deviation
LP	Linear Program
LTV-MPC	Linear Time-Varying MPC
MPC	Model Predictive Controller
OA	Over-Actuated
OA	Over-Actuation
PMSM	Permanent Magnet Synchronous Motor
QP	Quadratic Program

RCV	KTH-Research Concept Vehicle
RCV-E	KTH-Research Concept Vehicle E
RMSE	Root Mean Square Error
SMC	Sliding Mode Control
VEL	Longitudinal Velocity
YAW	Yaw angle

Chapter 1

Introduction

This chapter describes the specific problem that this thesis addresses, the context of the problem, the goals of this thesis project, and outlines the structure of the thesis.
Section 1.1 describes the background of the thesis project. Section 1.2 describes the problems that guide this project and state the research question that this thesis intends to answer. Section 1.3 explains the purpose of this project and its social, ethical and environmental contribution. Section 1.4 lists the sub-goals that the project goes through to fulfill its purpose. Section 1.5 explains the research methodology utilized for the research in this project. Section 1.6 defines the boundaries and limits of the thesis project. Section 1.7 provides a structure of the thesis report.

1.1 Background

1.1.1 Trajectory following and autonomous driving

Autonomous driving vehicles are becoming more and more interesting because of their driver-assistance capabilities, but as we look to the future, their real purpose is to replace the driver and allow him or her to focus on other things that are often the cause of distraction. An autonomous driving vehicle is required to estimate the route it has to pursue, the obstacles present along it, and decide the driving mode to use along the path. This can be achieved using an environment detection algorithm and a trajectory planner that evaluates all these conditions and translates them into the choice of a reference trajectory that the car has to follow. In robotics [1], a *path* is a term for how to get from one *pose* (defined by vehicle position and its direction) to another. A

trajectory is a *path* with the specification of the speed (even if not constant) that must be traveled. Therefore, a car performing trajectory following will have to proceed autonomously along the reference path at the required speed. To pursue the trajectory reference provided by the planner, a vehicle adopts a trajectory-following strategy, namely a more or less complex control algorithm that requests the car an adequate actuation to follow as close as possible the trajectory reference. To go a little deeper into the topic, a trajectory can be specified in different ways. Some basic possibilities are:

- Through a series of points in the space represented by the vector (vehicle position, heading, speed) that the car has to be close each time.
- Through a series of points in the space represented by the pose vector (vehicle position, heading) and an additional term representing the time instant at which every pose has to be reached. The time instant related to the travel distance between points indirectly provides the velocity.
- Through a mathematical function that represents a continuous definition of the car's position within the space, the desired heading, and the speed that the vehicle has to track. In addition, to better mimic real situations, a car driving on a street that follows a trajectory must stay within the road boundaries, so additional constraints can be added along with the trajectory specification. These constraints represent the maximum error allowed by the car to deviate from the trajectory reference.

Further, the control algorithm to pursue the path at the given speed is responsible for replacing the driver to perform autonomous driving. Depending on the vehicle structure and, in particular, its actuation (wheel torque and steering), the complexity may vary. The more actuators there are, the more complex the algorithm will be to select the best vehicle actuation, and this will play a decisive challenge for real-time purposes. The case of over-actuated vehicles is an example of this problem and will be better explained in the following section.

1.1.2 Over-actuated vehicle

A rigid body in the space has six Degrees of Freedom (DoFs), three for the translation (x,y,z) and three for the rotation (yaw, pitch, roll). A vehicle can be approximated to a rigid body in three-dimensional space and having thus six DoFs, but it can also be further approximated by considering only its planar

motion, which is the most predominant. In this case, the vehicle model reduces the number of DoFs to three (x,y, yaw) without loosing much accuracy [2].
Generally speaking, road cars can be controlled through longitudinal acceleration/deceleration and front-wheel steering, and the actuation cannot control the three DoFs independently. Road vehicles are generally constrained by Ackermann kinematics and can only follow an Ackermann-constrained path because of the low number of actuators.
Over-Actuated (OA) vehicles, on the other hand, offer more freedom in this respect. They have more control inputs than DoFs to control, and this means that, first, different DoFs can be controlled independently, and second, multiple actuators can be employed for the same DoF, generating redundancy in the choice of the actuation. Because of this redundancy, infinite control input combinations drive the car equivalently through its DoFs. The problem now is to have a criterion to select a control action among the infinite ones. Actually, this is not an issue but an advantage: it is now possible to choose the control action, among the infinite ones, that fulfills other tasks or solves additional problems.
For example, over-actuation can be exploited to drive the vehicle along the desired trajectory and, as a further task, improve its stability. This is done by defining stability margins and selecting the optimal control action that better stays within these margins. Another example of an additional task is the minimization of the energy consumed by the vehicle while performing trajectory-following. An estimation of all the sources of energy loss can be performed, and the optimal control action is selected to minimize the energy loss.
There are multiple levels of over-actuation, depending on the actual DoFs to be controlled and the configuration of the actuator, the solutions are different. Not only vehicle pose (x,y, heading) can be directly controlled, but also specific vehicle dynamics, such as lateral dynamics, where the DoFs investigated are the yaw rate and the side slip angle [3, 4]. Therefore, depending on the controlled system or subsystem, the number of DoFs can vary, and if the number of actuators affecting the system is higher than DoFs, the system is defined Over-Actuated (see Section 2.1 for details).
Control techniques to increase the number of actuators in vehicles compared to usual road cars are:

- Torque vectoring (4WD, 4WB), which distributes the torque on the four wheels independently to each other and consequently reduces the dependency of the vehicle's rotation from the longitudinal translation.

- Four-Wheel Steering (4WS), where also rear wheels are involved, improves the vehicle's steering and provides the possibility to translate the vehicle laterally without affecting rotation.
- Active camber and active suspension improve the availability of force allocation to the wheels, providing better maneuverability and performance in critical conditions.

1.1.3 KTH-Research Concept Vehicle (KTH-RCV)

The KTH-Research Concept Vehicle E (RCV-E) is an over-actuated vehicle built at the Integrated Transport Research Lab (ITRL) at KTH in 2012 [5]. This vehicle has four in-wheel electric motors with electric individual steering wheels (4WS), traction/braking (4WD-4WB), active camber, and active suspensions. A peculiarity of in-wheel electric engines is that no transmission is required to convey motion from the engines to the wheels, resulting in lower power losses due to friction. The high level of over-actuation allows for a wide range of experimental evaluations in several fields. As a result, research (Section 2.2) is addressed to study how different combinations of over-actuation affect driving performance, safety, and energy consumption and how redundancy can be exploited to improve them. The vehicle mount as control software a dSPACE unit (MicroAutoBox II 1401/1513) [6] that uses a CAN bus for transmitting the signals through sensors and actuators. MicroAutoBox is the control interface developed by dSPACE to control prototyping vehicles; it handles sensors and actuators and is responsible for scheduling the processes at the defined rate.

Figure 1.1: RCV-E developed at the ITRL within KTH.

1.1.4 Importance of energy optimization

The future of electric vehicles will be likely certain, especially with the European decree *Fit for 55* [7], car manufacturers will only be allowed to produce zero-emission vehicles from 2035. For this purpose, the transition to electric will have to compensate for discrepancies with combustion vehicles, like vehicles' energy autonomy. Several components of the power-train influence the autonomy of electric vehicles, the energy density of the batteries, the power transmission from the engine to the wheels, and the efficiency of the electric motors. The energy density of batteries is not comparable to that of fossil fuels, which is why combustion vehicles have a significant autonomy advantage. Nonetheless, the efficiency of electric engines is substantially higher than that of combustion engines, thanks in part to the ability to use regenerative braking to recover some of the energy. However, this advantage is not enough to even out the disparity.
Therefore, research on electric vehicles becomes fundamental from the energy improvement aspect. The advantage electric vehicles have from a future perspective is that they are suitable for more precise control of the actuation than combustion-engine vehicles, allowing researchers to study novel energy optimization technologies ahead of 2035.

1.2 Problem

As Over-Actuated vehicles, by definition, have more actuators than Degree of Freedom, they offer the advantage of exploiting the redundancy of the control action to fulfill additional tasks. As regards the importance of energy minimization in electric vehicles, explained in Section 1.1.4, actuation redundancy can play a relevant role. Besides, autonomous driving represents the future of road vehicles, where a structured control strategy will replace the driver's duties. Merging these two fields, the problem of combining autonomous drive with energy minimization for an OA vehicle arises. In particular, the research topic of this project is to develop a control strategy for an OA vehicle that guarantees trajectory-following and solves the allocation problem while reducing energy consumption. However, for road cars, additional constraints must be considered and guaranteed. The control action must be such to ensure stability during driving so that there is no risk for the vehicle to behave unexpectedly. It represents an additional constraint for the controller, but stability is critical to ensure passenger safety. In addition, the possibility of testing such a controller on an OA vehicle developed within the KTH adds additional demands. The control strategy for properly working on the RCV-E [5] must be such to run in real-time. Here, the necessity to develop a sufficiently agile and fast controller to cope with this problem. The requirement to balance between complexity in a control strategy that must accomplish multiple tasks, i.e., trajectory-following and allocation over many actuators, and agility to function in real-time on an embedded platform [6] is the central problem that will guide this research project.

1.2.1 Research question

How can different control techniques guarantee trajectory following and stability with the aim of optimizing the energy consumption required in an Over-Actuated electric vehicle (RCV-E [5]) in real-time?

1.2.2 Hypothesis

The control techniques and in particular the solution that will be implemented can effectively work in real-time on the RCV-E [5].

1.3 Purpose

The objective of this project is to advance research on Over-Actuated vehicles, with a focus on trajectory-following and energy optimization. Previous works within KTH [8, 9] analyzed the convenience of Over-Actuation to improve energy consumption and stability. Their goal (see also Chapter 2) is to investigate how over-actuation affects forces allocation at the wheels to fulfill a given task. In particular, active camber control and torque allocation (torque vectoring) characterize the actuation in previous works. This research project intends to build on them and develop a controller that solves the problem presented in Section 1.2. The purpose of the research derives from the necessity to have an embedded implementation on the RCV-E of a controller able to allocate an optimal control action on multiple actuators. This contribution can provide the basics for the experimentation on the RCV-E for control that employs an optimal solver to choose the control action.
Besides, the benefits are also related to the relevance of energy consumption. This project plays a role in the environmental problem of energy shortage and clean energy requests. From the necessity to investigate multiple solutions to reduce power consumption in transportation, Over-Actuation in vehicles represents one of the candidates to contribute to solving this condition. The following paragraph (Section 1.3.1) shows the benefits of this research on social and ethical aspects from a more tangible perspective.

1.3.1 Social, ethical and environmental aspects

This thesis project intends to advance the research on OA electric vehicles with energy minimization purposes. According to the European plan for the green transition *Fit for 55* [7], cars and vans will have to guarantee zero CO2 emission since 2035. This proposal is one of the many stated in this package, and all aim of ensuring that EU policies are in line with the climate goals agreed by the Council and the European Parliament.
The main option to satisfy the zero-emission car's goal is to rely on electric and hydrogen cars. Therefore, research on electric vehicles becomes essential to face all people's necessities by 2035, and one of these necessities is the electric vehicles' autonomy. This project study intends to face this problem and advance the research to minimize the consumption of electric vehicles, in particular exploiting the Over-Actuation.
Minimizing the energy consumption of electric vehicles has results from both social and environmental perspectives. It will make electric vehicles more

appealing because it improves their autonomy, and long-distance travel will become more sustainable for people. This will facilitate also the transition from the combustion to electric engines by 2035. In addition, the improvement in energy consumption impacts the environment independently from European regulations. The reduction of the energy lost while driving entails less energy utilized and fewer resources employed for driving cars.

1.4 Goals

To find an answer to the research question Section 1.2.1 and develop a control algorithm able to run in real-time on the RCV-E [5], the thesis project will go through different steps and fulfill intermediate goals:

1. Investigate the possible sources of energy consumption and understand which are more affected by the Over-Actuation (4WD, 4WB, 4WS) and which highly influence the total amount of energy employed on the vehicle.

2. Adopt a car model for the over-actuated vehicle. Previous research projects (Chapter 2) studied and analyzed the effect of different vehicle models on over-actuation control. In this thesis project, an adequate car model will be chosen to take into account the predominant dynamics of the vehicle and neglect others less relevant to reduce the complexity. The model will have to take into account the actuation of the vehicle and consider the relevant sources of energy consumption as investigated at point 1).

3. Develop and tune a control algorithm to fulfill the primary tasks of trajectory following and vehicle stability. Simultaneously it must handle the control input allocation by solving an optimization problem such that the vehicle exploits the minimum amount of energy.

4. Embed the controller on the RCV-E [5], investigate different options for this scope, and properly tune the controller for real-time purposes.

1.5 Research Methodology

The scope of this thesis is to face a specific goal (Section 1.3) and subgoals (Section 1.4) to give an answer and solve a specific problem (Section 1.2). A qualitative research methodology [10] will be adopted in order to understand

and assess the different models, algorithms, and tools to reach the goal. Besides, large data sets do not concern the scope of the research, and the assessments will be carried out on smaller amounts of data collected during tests. The framework of the degree project is predominantly constituted by analytical and applied research methods [10]. The work starts from existing knowledge, both from previous research projects and from control theory fundaments. Later, after examining a set of circumstances, the results are addressed to the specific goal of implementing a controller with real-time purposes. The thesis work aimed to develop a control algorithm, and an inductive research approach [10] is adopted since is recommended in the development of artifacts. Besides, this research approach better fits with qualitative methods used during the projects, and no deduction of the best control strategy from large data sets was possible within the characteristics of this thesis project.

1.6 Delimitations

The boundaries within which this thesis project takes place are related to its different parts. As regards the trajectory-following objective, the vehicle is expected to stay as close as possible to the provided references, but no constraints on its position are considered. Although a correct tuning of the control action should guarantee a good trajectory-following, the boundaries of the road are disregarded. This represents a limit of this research's results that affects real applications where the presence of additional vehicles or road conditions presume the inclusion of the constraints.
Besides, regarding energy minimization, this project is mainly focused on exploiting Over-Actuation for energy consumption goals when a positive traction force is required. Therefore, although the vehicle's kinetic energy recovery in braking conditions may also be affected by a different torque allocation at the wheels, it is not considered within the scope of this research.
Finally, concerning the implementation of the controller on the RCV-E, only tests to validate the controller regarding real-time purposes were performed. These tests were held in a stand-still condition, without driving the vehicle, because it was not possible to validate the controller's performance on the RCV-E from the point of view of trajectory tracking and energy minimization. These validations were carried out only in simulation.

1.7 Structure of the thesis

Chapter 2 presents the literature study and works concerning over-actuation, vehicle stability, and energy consumption. Chapter 3 analyzes the controller's tasks, i.e., trajectory-following, power consumption, and stability, and presents how they are included in the control strategy. Chapter 4 defines the vehicle model the controller utilizes, considering the actuation available (4WD, 4WS) and the driving objectives. Chapter 5 describes the control strategies chosen to perform trajectory-following and presents the simulation results on the performance. Chapter 6 introduces the energy minimization control strategies and shows the improvements obtained. Chapter 7 discusses the problems and the solution to embed the controller on dSPACE - MicroAutoBox II [6]. Besides, it shows the real-time performance and the limits of the control strategy on the RCV-E. Finally, Chapter 8 draws conclusions and opens new challenges for future work.

Chapter 2

Related works

This chapter describes the relevant work on which this thesis intends to build. In particular, Section 2.1 presents a brief overview of the general control techniques adopted to manage Over-Actuation. Section 2.2 presents previous works within KTH that investigate Over-Actuated vehicles with a focus on energy consumption. Section 2.3 analyzes all the other relevant work on Over-Actuation (OA) for energy optimization. Section 2.4 introduce vehicle stability and identifies previous projects on OA vehicles for stability purposes. Last, Section 2.5 presents works that combines energy minimization and stability.

2.1 Over-actuation control

Over-Actuated systems find wide use in aircraft vehicles. One of the advantages for which they are exploited is the use of actuator redundancy to improve safety in case of failure [11, 12]. However, in the case of failure-free situations, the control systems of aircraft and road vehicles have both the objective to use redundancy to solve further tasks and improve driving or flying conditions. Here, controllers aim to solve the allocation problem, which for linear problems, is formulated as follows [13]:

$$\begin{aligned} Bu &= d_{des} \\ u_{min} \leq u &\leq u_{max} \\ \dot{u} &\leq \dot{u}_{max} \end{aligned} \tag{2.1}$$

d_{des} is the desired virtual control input, i.e. the desired overall control action.
u is the real control variable, i.e. the input to the actual actuators.
B is the matrix that link the real control action to the desired one.

A necessary condition for a system to be Over-Actuated is that the number of columns of B must be greater than the number of its rows [13]. Depending on the freedom of choice that Over-Actuation allows and the operational constraints on actuators, like saturation, different control approaches can be adopted: from the simplest to more complex ones.
When it is obvious how to combine two or more redundant control effectors, explicit ganging [13] represents a good solution. It uses a linear combination of the redundant control effectors to reduce the control space dimension of an Over-Actuated system.
An approach that weakly exploits the redundancy is to use one actuator to control a controllable variable until saturation occurs, then a second actuator supports the previous one. This method is referred to as Daisy Chaining [13, 14].
Another direct approach is to use the pseudo-inverse of matrix B to find the u solution, and an iterative method called Redistributed Pseudo Inverse [13, 14] can be adopted to handle actuator saturation.
The solution most widely used in literature is optimization, which is formulated as follows [13]:

$$\begin{aligned} \min_{u} \; & J = ||Bu - d_{des}|| \\ s.t. \quad & u_{min} \leq u \leq u_{max} \end{aligned} \tag{2.2}$$

The norm used depends on the algorithm used to perform minimization, with 1-norm and INF-norm the problem results in a Linear Program (LP) [14]. A very common solution is to formulate the problem Eq. 2.2 as a Quadratic Program (QP) and write it as a 2-norm.
In the case where the control effectors are not saturated, the redundancy of Over-Actuation may produce multiple solutions that lead to $J = 0$, and a secondary objective can be introduced to select the final control action [13, 14]. Fixed u_p as the preferred control action, the problem can be reformulated as a Mixed Optimization [13]:

$$\begin{aligned} \min_{u} \; & J = ||Bu - d_{des}|| + v||u - u_p|| \\ s.t. \quad & u_{min} \leq u \leq u_{max} \end{aligned} \tag{2.3}$$

For nonlinear effector models, formulated as follows [14]:

$$\begin{aligned} &\min_{u} J(u) \\ s.t. \quad &F(u) = 0, G(u) \geq 0 \end{aligned} \tag{2.4}$$

one option is to linearize the equations locally, to represent the model as an affine model [15] and to solve it locally as a linear model. The other option is to solve a nonlinear optimization [14].
This list represents a theoretical introduction to the Over-Actuated control allocation methods, whereas applications on vehicles is presented in the following sections.

2.2 Over-actuation at KTH with a focus on energy optimization

This project intends to build on the work of P. Sun [8, 16, 17]. In his Doctoral Thesis [8], he explores the energy-efficient control methods and models for OA Electric Vehicles (EVs). Besides particular attention to camber control for this purpose, an analysis of front steering wheels (FWS) and torque vectoring (4WD-4WB) to directly control the yaw moment DYC for stability and energy efficiency purposes is carried out [8, 16, 17]. The result of an offline optimal torque distribution to minimize the power consumption is exploited to relate the engine efficiency with the yaw moment (Mz) at steady-state cornering [16, 17]. Besides, a stability region based on yaw rate and side slip angle is defined, and a sliding mode control is adopted to select the stability yaw moment (Mz) [16, 17].
In [17], a comparison between the energy-efficiency DYC and the stability DYC under double lane change at different speeds is made. The first distributes the torque so that the average power consumption is reduced, whereas the second guarantees a smaller yaw rate and side slip angles but it cost higher power consumption even under light maneuvers. A trade-off is proposed with a switching principle [16] that moves the control set from DYC for energy minimization to DYC for stability in the case of safety-critical maneuvers. This solution guarantees stability, reduces power consumption, compared to the only stability DYC case, and is also promising for real-time purposes.
In J. Edrén's work [9], a general investigation of the over-actuation possibilities has been outlined. Different types of vehicle and tire models are analyzed from the point of view of real-world fidelity and computational performance. The effect of camber, active suspension and torque allocation on over-actuated vehicles is examined to improve performance and safety. First, a force

allocation algorithm based on optimization is presented, then a simplified one, which geometrically allocates the longitudinal and lateral forces and yaw moment to the wheels proportionally to their possibility to generate force. Later, evaluations on a small-scale prototype vehicle are realized. Importance is also given to energy optimization in [18], where different variants of actuation (combinations of steering and torque allocation) are investigated during non-safety-critical cornering situations. Results suggest a front-wheel torque drive vehicle with torque vectoring combined with four-wheel steering. It was noticed that the largest contribution to the reduction of energy consumption during cornering is provided by rear-axle steering: compared to traditional road car driving, the improvements are about 10%. In [19], Edrén focuses the research topic particularly on force allocation at the wheels, investigating the problem for a small-scale prototype.
In S. Bath's thesis [20], front and rear axle camber angles combined with front and rear axle steering angles are used to stabilize the vehicle lateral dynamics (yaw rate and side slip angle) while minimizing the cornering resistance for energy minimization purposes on an over-actuated vehicle. Dynamic Programming (DP) is used to derive an offline optimal solution that is useful as a benchmark for energy reduction dissipation. Later, a Model Predictive Controller (MPC) formulation starting from the DP results is responsible for the online tracking of the car reference states yaw rate and side slip angle. The MPC [21] implementation on a KTH-Research Concept Vehicle (RCV) [22] is performed.
In M. M. Davari's work [23], tire energy losses are studied to improve the energy efficiency of over-actuated vehicles under the effect of camber angle, side slip angle, and slip rate. He investigated different tire models for energy purposes, and a high-fidelity semi-physical non-linear tire model called Extended Brush tyre Model was developed [24]. Half-car model [25], bicycle model [26,27], and 3-DoF vehicle model [28] were used for tire energy loss analysis. In addition, the effect of the road tarmac [29] on tire losses was considered. In the end, control allocation strategies exploit Dynamic Programming and MPC to optimally control over-actuation, and tests on RCV [22] were performed to investigate separately the vehicle's actuation on different maneuvers.

2.3 Over-Actuated vehicles with a focus on energy optimization

Research studies on over-actuated vehicles for energy optimization are outlined here; the goal is to estimate the sources of power consumption in the car and adopt a control allocation strategy that reduces this consumption. As in [30], the control allocation scheme allocates torque and steering angles to track the vehicle's planar velocities (vx, vy, yaw rate) provided by the upper-level controller. The solution proposed is a two-step optimization where two cost functions are optimized simultaneously; one for reference tracking and one for the engine's energy minimization. A two-step optimization simplifies the tuning compared to the case where only one cost function is used. However, this solution showed lower efficiency in terms of speed, and to speed up the search for the minimum a tuned-offline heuristic function was used to approximate the energy consumed.
A technique to minimize power consumption in a four-wheel driving vehicle is to distribute the torque between the front and rear axles according to the necessities. Different studies adopted this solution based on engine efficiency characteristics [31–37]. In [31], an OA vehicle with in-wheel electric motors exploits a control strategy to allocate the total reference torque on the two axles, and the optimal allocation ratio can be obtained offline from experimental data. Results show that for straight driving at a constant speed, two-wheel drive is more efficient than four-wheel drive. A similar approach is proposed in [32, 33], where the two sides of the car, left and right, are considered independent to better track the reference yaw moment beyond the longitudinal force. The power optimization relies on the motor efficiency, and the allocation ratio per side can be obtained from an offline generated table based on experimental data as in [31]. The same results as in [31] show that when the torque required is low, the optimized solution is the two-wheel-driving mode. In [33], when the two-wheel-driving mode is preferred, the allocation is on the front wheels to lower the over-steering behavior. In [34], a search algorithm based on the golden section method is proposed to allocate the total torque on the two axles. It is an iterative method to find the minimum of a function, namely the engine power consumption, inside a specified interval. A linear derivation of the wheel slip ratio is considered in the problem formulation because tests were performed on a high-friction road, and no stability boundaries on the slip ratio were added. Optimal axle torque allocation is adopted in [35], where the friction losses are included in

the problem formulation to estimate the additional amount of torque to apply at the wheels. Particular attention is also added to avoid opposing torque between the front and the rear axle to prevent inferior energy efficiency. For low-torque requests, the optimization leads to the use of only one axle. Conflicting results are obtained in [36], where the torque allocation between the front and rear axle for power minimization purposes leads to equally distributed torques on the axles. This is due to the efficiency characteristics of the PMSM. In [37], it is described a novel efficiency torque distribution on the two axles, the aim is to minimize the power losses by providing the requested wheel torque and yaw moment. An analytical solution that fits the engine power losses with a third-order polynomial curve is compared with two offline optimization solutions. The results of the online optimization strategy are very close to the more sophisticated offline optimization control strategies.
Further works to improve energy consumption are focused on the minimization of tire energy losses. In particular, driving on the outer wheels of a vehicle [38], similar to [18], reduces the cornering resistance and, consequently, the energy consumed by the tires. This result is verified by an optimization performed with a simpler four-wheeled handling model. In [39], an online control system is proposed in order to improve the vehicle's energy efficiency by minimizing tire power losses: tire slip resistance, and rolling losses. The controller developed, named Tire Inflation Pressure Regulation System (TIPReS), regulates the tire pressure, which affects both the rolling losses and the tire slip resistance. For the estimation of the latter term, an inverse tire model derives the slip rate from the longitudinal tire force using a second-order polynomial fitting curve. This model improves online optimization to compute the best tire pressure. In [40], a semi-empirical tire slip energy model is developed to easily estimate the slip energy online with high accuracy.
Section 2.5 presents further works on energy minimization that take into account also vehicle stability.

2.4 Vehicle stability

Electronic Stability Control (ESC) is a massive innovation and has become essential in nowadays' vehicles. The impact on vehicle crashes is astonishing: results indicate that the ESC prevents about 40% of all crashes involving loss control [41, 42]. Vehicle stability control systems prevent vehicles from spinning, drifting out, and rolling over [43]. In particular, systems responsible for preventing vehicles from skidding and spinning out are often referred to as yaw stability control systems, and strategies like Torque Vectoring

(4WD, 4WB) and Four-Wheel Steering (4WS) can highly affect the yaw stability for an over-actuated vehicle. ESC is also responsible for the vehicle's longitudinal stability in terms of wheel slipping or locking. Therefore, tire stability is necessary to ensure vehicle stability. As proof of this, vehicle stability (longitudinal, yaw, and roll over stability) can be referred to as a comprehensive indication of the four tires' force state [44], and it is evaluated and predicted from the forces acting on the wheels and the driver's input. In summary, vehicle stability is critical and depends on the stability of its components, such as tires.
The following section discusses the state-of-the-art of stability-optimized over-actuated vehicles.

2.4.1 Over-actuation for stability purposes

Yaw stability control has been highly investigated in W. Zhang's work. In his Doctoral thesis [45], he shows how path-following and yaw-stability performance in critical maneuvers are improved using over-actuation. Different vehicles and tire models are analyzed at various levels of complexity depending on the specific application. Both torque vectoring [46] and active camber control [47] to directly control yaw moment (DYC) are analyzed. The controllers based on MPC are designed to compare one-level to two-level structured torque allocation controllers, as well as rule-based and optimal solutions, and assess their performance to achieve yaw stability [46]. Active camber control can produce extra lateral tire forces and overcome their saturation on normal actuation during critical situations. It can be seen that active camber results in higher tire usage, which contributes to performance improvement.
Other works adopting Direct Yaw moment Control (DYC) follow.
In [48], a hierarchical control strategy to control lateral vehicle dynamics (yaw rate and lateral slip angle) is presented. A top layer that uses a feed-forward and feedback controller provides the reference yaw moment (Mz) to the allocation step that, together with the desired longitudinal force from the driver, allocates the torques at the wheels. The allocation step is an MPC that starts from a pre-allocated solution, exploits torque vectoring, and keeps the wheel slip ratio in the stability area. A similar control hierarchical structure is proposed in [49], where the upper-level exploits Sliding Mode Control (SMC), and the allocation problem also handles camber angles.SMC is adopted also in [50] for the higher-level controller, while the lower level uses a cost function where the forces on the axles are proportional to the vertical load. DYC is also addressed

in [51], where a comparison between three toque allocation controllers during different maneuvers is presented. Optimal torque distribution with as objective the maximization of the stability margin given by the friction circle performs better in all cases than the average torque distribution and than the torque distribution proportional to the wheels load. A further structured control algorithm for yaw stability is proposed [52]. The driver requests steering and velocity references, so the forces and the yaw moment on the car's Center of Gravity (CoG) are computed with an adaptive robust controller for reference tracking. The allocation problem is solved using torque vectoring and rear steering to improve yaw stability while limiting the forces on the wheels by the friction circle. In [53], an MPC allocation approach is adopted to track reference yaw moment and longitudinal force at the car's CoG; it relies on a pre-allocation step that computes the torques using the pseudo-inverse of the geometrical vehicle structure matrix. Attention is given to limiting the longitudinal tire slip and reducing the input utilization. Similar attention is paid in [54], but a different solution from DYC is proposed. An MPC stabilizes the two-state system (side slip angle and yaw rate) using wheel torque and front wheel steering without computing the yaw moment required for the yaw stability. The reference yaw rate is computed from the steering angle using the bicycle model, and the reference side slip angle is set ideally to zero. The same approach is proposed in [55], where the friction circle is considered to guarantee tire stability. A nonlinear MPC [56] is used to control the wheel torque to keep the longitudinal slip angles in a safety region and to the desired value for the traction force generation. In [57], the concern is given to the side slip angles, where constraints are used to maintain vehicle stability. A high emphasis on tire stability is given in [58], where the allocation problem is performed by assigning slip rate and side slip angles as virtual controls to the wheels to follow forces and yaw moment at the CoG of the vehicle computed by a higher-level SMC. Using these virtual inputs, it is possible to directly limit them to the stable region such that the friction ellipse nonlinear constraint can be decoupled into two linear constraints because the slips depend linearly on the friction coefficient.
A combination between Active Front-wheel Steering (AFS) and Direct Yaw moment Control is adopted to perform yaw stability control of the vehicle [59] and [60].

2.5 Over-actuation for stability and energy minimization purposes

In the following works, vehicle stability and power consumption reduction are achieved simultaneously. The combination of these two goals is realized by exploiting over-actuation on EVs, often mixing solutions presented in Sections 2.3 and 2.4.1.

In [61, 62], a first step torque allocation algorithm is realized to allocate the requested longitudinal force on the wheels using the in-wheel engine characteristic in order to minimize the power consumption. A further allocation step starts from this result to find a close solution that bounds the longitudinal slip ratio within linear boundaries and provides the requested total traction force. Lateral forces are also considered [63] and estimated to limit the longitudinal forces at the wheels by defining a stability region within the friction circle. The tire slip dynamic is omitted in the interest of real-time performance, and an MPC solution is adopted to track longitudinal force and yaw moment at the CoG while considering the engine efficiency map to lower the power consumption.

Yaw stability is also taken into account in [64, 65]. A hierarchical control structure is proposed [64] and exploits the upper level (SMC) to control the yaw rate and the side slip angle *beta* and provides references to the lower level, which allocates the wheel torques for reference tracking and power minimization. The allocation differentiates the solution depending on the situation: it exploits a rule-based strategy when steering and a motor efficiency optimization when driving straight. Similarly, in [65], the middle layer (MPC) controls yaw stability and supplies longitudinal force and yaw moment references to the lower level, which minimizes power consumption in terms of engine efficiency and tire slip power losses.

In Y. Chen's work, different control techniques are analyzed to handle the asymmetry between energy consumption during driving and regenerative braking [66–69]. In [66], after developing a torque allocation algorithm for virtual variables tracking and energy optimization during driving and regenerative braking, he formulated the problem solution in order to handle the two modes. In [67, 68], he proposed a KKT-based algorithm to find the global minimum for both single and dual-mode energy-efficient Control Allocation (CA) problems. Comparison [69] between the previous solution with a rule-based one and the KKT-based CA algorithm consumed the least energy among the three methods thanks to global optimization.

Chapter 3

Analysis of the control tasks

This chapter aims to analyze the different tasks the controller has to fulfill, i.e., trajectory-following, energy minimization, and vehicle stability, and how the control strategy intends to include each. Section 3.1 introduces the simulation environment, explaining its features and the changes needed to model an Over-Actuated vehicle. Section 3.2 describes how the trajectory-following problem is defined, which references are tracked, and how the problem is solved in the control strategy. Section 3.3 explores the sources of power consumption in electric vehicles, and stands out those that can be influenced by over-actuation (4WD-4WS). These are compared to one another from the simulation results to see how much they affect energy consumption. Section 3.4 analyses the sources of instability and considers which are fundamental to be guaranteed and which are less affected by the driving conditions.

3.1 Simulation environment

This research project was carried out to obtain usable and implementable results on a real vehicle. Before implementation and testing on the RCV-E, validation was performed in IPG CarMaker [70], a simulation software for virtual test driving for automobiles and light-duty vehicles. IPG CarMaker provides the opportunity to be integrated into the MATLAB/Simulink environment [71], where the IPG CarMaker features were added to the Simulink environment using S-functions and MATLAB/Simulink API functions. "CarMaker for Simulink" [71] offers the possibility to apply changes to the IPG CarMaker environment, namely modify the vehicle model, change the vehicle's parameters, replace the vehicle driver with a controller, and log data from IPG CarMaker's simulation.

The vehicle used during the simulation is a Tesla Model 3, Figure 3.1, whose principal parameters are shown in Table 3.1.
In Simulink, different changes to the test car are applied to match the characteristics of the Over-Actuation considered. The vehicle power-train is changed to request an individual torque to the four wheels. Four Permanent Magnet Synchronous Motor (PMSM) are modeled to mimic the behavior of the in-wheel engines of the RCV-E as the torque-speed efficiency characteristic (Appendix A). Besides, the Tesla's four wheels are adapted such that the controller can steer them independently.

Figure 3.1: Side view of the test vehicle in simulation.

Tesla Model 3	
Parameter [Unit]	**Value**
Mass $[kg]$	2108
Total yaw inertia $[kgm^2]$	3954.3
CoG height $[m]$	0.545
Wheelbase $[m]$	2.97
Track width $[m]$	1.68
Wheel radius $[m]$	0.33
Engine maximum torque available $[Nm]$	230

Table 3.1: Vehicle parameters.

3.2 Trajectory following strategy

This section explains how the trajectory is defined within the context of this project, how the reference points are sampled from it, and how the controller

is configured to follow the references. Besides, a brief overview of other projects dealing with trajectory-following will be presented along with the additional considerations to introduce for a vehicle able to move sideways without affecting its direction (yaw angle).

The objective of the vehicle is to follow a given trajectory, so path coordinates (x, y) must be provided. The car will have to remain as much as possible close to these reference coordinates while performing autonomous driving. Besides, since the Over-Actuation allows the RCV-E to control rotation and lateral motion independently from each other, the desired vehicle direction θ can be arbitrarily provided as an additional reference to track. One advantage of having this DoF tunable by a path planner is that it is possible to force lateral motion, with the vehicle yaw angle fixed, to improve vehicle stability as in a double-lane change. The reference path coordinates may slide sideways while the reference heading remains unchanged, as in Figure 3.2. If this is not the case, then the desired reference heading θ can be defined as the linking direction between two consecutive points (x_1, y_1) and (x_2, y_2). Last, the vehicle has to follow the path with the desired admissible velocity. In the context of this project, the main movement of the car is longitudinal, so only the longitudinal reference speed v_x is required, however, the solution proposed can also be easily adapted if a lateral velocity reference is to be provided.

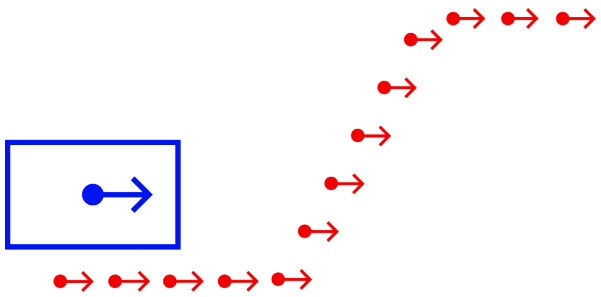

Figure 3.2: Representation of path moving sideways.

Now, the vehicle has to follow a trajectory made by four elements (x, y, θ, v_x), and as explained in Section 1.1.1, the planner sends the references for the controller, which can be described in multiple ways. In this thesis, a point-to-point trajectory is chosen (Figure 3.3), with each point represented by the vector (x, y, θ, v_x). However, this is not a binding choice; as a matter of fact, the framework of the control algorithm presented in this project is also flexible to other trajectory representations and does not depend on the used

one. In fact, the controller (see Chapter 5) presents an interface that allows it to select only a few points to perform prediction along the given path. It will be sufficient to adapt this interface to the type of representation the planner provides. In addition, for point-to-point trajectory, denser points approximate better a continuous path and guarantee a smoother reference to follow. On the contrary, if the distance between points is higher, the controller will be less bound by the references and consequently less precise in following the trajectory.

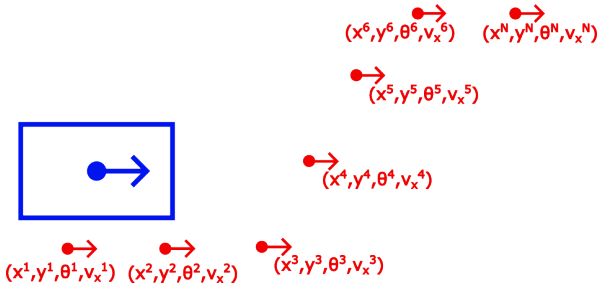

Figure 3.3: Trajectory specification.

3.2.1 How the controller performs trajectory following

This section explains the strategy adopted by the controller to track the reference trajectory.

As it will be better explained later (see Section 3.6), the control strategy used in this project relies on MPC for the trajectory-following task. MPC exploits prediction along the path to decide the control action, and a solution to select references along the trajectory is needed. From a point-to-point trajectory, N points along the prediction horizon must be sampled, with N the number of prediction steps of the MPC.
To sample them, the nearest trajectory point to the car's current position is located (Figure 3.4a). From it, the first reference is selected to have a distance of $T_s * v_x$ along the path, and the subsequent references will be sampled to have a distance $T_s * v_x$ from their previous one. In particular, T_s represents the sampling time, whereas v_x is the longitudinal reference velocity of the previous reference point. As a result, the distance $T_s * v_x$ is not constant and depends on the varying reference velocity v_x along the path and the sampling time T_s which can also be chosen as not constant.
Besides, the trajectory representation consists of a discrete number of points.

Therefore, to move along the path of a distance $T_s * v_x$ and select the next reference from the previous one, the crow-flies distance between two consecutive points is used until the sum of these distances exceeds $T_s * v_x$ (Figure 3.4b). The selected reference will be the last point that does not exceed the distance $T_s * v_x$.

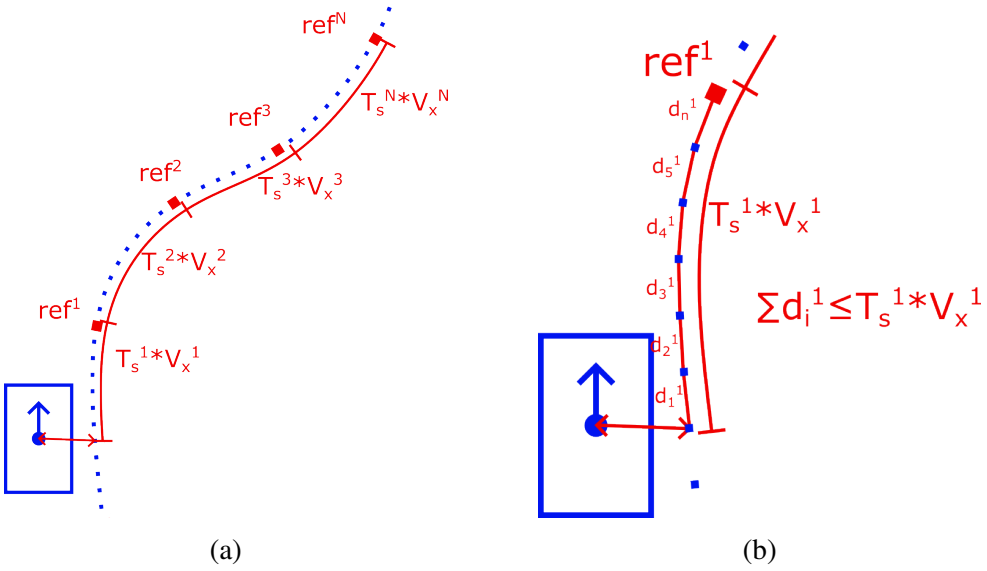

(a) (b)

Figure 3.4: Trajectory sampling over the prediction horizon.

From the N references provided to the controller, a control strategy for trajectory-following has to be derived.
The vehicle state is defined by its position in the global reference frame (x_{car}, y_{car}), heading direction, and the three planar velocities, i.e., lateral, longitudinal, and yaw rate, in the vehicle reference frame.

$$x = \begin{bmatrix} x_{car} \\ y_{car} \\ \theta \\ v_x \\ v_y \\ \dot{\theta} \end{bmatrix} \tag{3.1}$$

The simplest option is to ask the MPC to lower the difference between the reference position, heading direction, and longitudinal speed with the corresponding vehicle's states, as in Equation 3.2. However, in this way, the

tracking of the position reference will also affect the longitudinal velocity of the car. In fact, the more aggressively the controller is while tracking the next reference position, the faster it will drive the vehicle despite the speed reference. Proper tuning can find a trade-off in this problem, but a more reliable solution can be developed. The idea consists of separating the control of the lateral and longitudinal dynamics of the vehicle and exploiting the speed reference to control the longitudinal dynamics and the lateral deviation from the trajectory to control the lateral dynamics.

$$\min \begin{bmatrix} \overline{x} \\ \overline{y} \\ \overline{\theta} \\ \overline{v_x} \end{bmatrix} - \begin{bmatrix} 1 & 0 & 0 & 0 & 0 & 0 \\ 0 & 1 & 0 & 0 & 0 & 0 \\ 0 & 0 & 1 & 0 & 0 & 0 \\ 0 & 0 & 0 & 1 & 0 & 0 \end{bmatrix} \begin{bmatrix} x \\ y \\ \theta \\ v_x \\ v_y \\ \dot{\theta} \end{bmatrix} \tag{3.2}$$

where $[\overline{x}, \overline{y}, \overline{\theta}, \overline{v_x}]^T$ is the next reference vector, and $[x, y, \theta, v_x, v_y, \dot{\theta}]^T$ is the vehicle's state.

This control strategy is also widely used in literature. Previous research projects [72–74] define the vehicle model as the error model where the lateral distance of the vehicle from the reference trajectory and the difference between the vehicle yaw angle and the reference yaw angle become states of the new system. In particular, works [72, 73] define a spatial-based vehicle model where the error states are a function of the position along the path, whereas [74] also considers forces at the wheels. These projects model a front wheel-steering vehicle and account for a path that can only run in the direction of its reference yaw angle to be compatible with the car considered. Therefore, the car's lateral displacement is dependent on its heading and cannot slide sideways, as the RCV-E does, and the reference path has only the yaw angle as a fundamental component to track because no lateral sliding is admissible. In this case, it is possible to write the vehicle's lateral deviation from the reference path as a function of the yaw angle error, defined as the difference between the car's and the path's yaw angles.
The vehicle error model has as a reference frame the path to follow, and the MPC aims to minimize the two states of the system since they represent the error from the reference. For the case of the RCV-E and a reference trajectory that can slide sideways, the MPC tracking is more complicated. The lateral deviation no longer depends only on the yaw angle error, and the reference

path cannot be defined only by its yaw reference: the position of the points is independent of their yaw angle. As a result, the vehicle error model utilized in the previous works must be extended to account for the car's and path's lateral velocities.
A different approach to separate the lateral and longitudinal dynamics of the vehicle is proposed in [75]. Here, the control of a standard road car is no longer dependent on the error model and exploits the vehicle lateral dynamics model to track the given trajectory. The work minimizes the distance between the lateral position, as the predicted output, and the road center line as follows.

$$J = ||Y(k) - R(k)||^2 \tag{3.3}$$

In this thesis project, a similar approach to [75] is used.
The objective function intends to minimize the vehicle's lateral deviation LD from the reference position and track the reference yaw angle θ_r and the longitudinal velocity v_{xr}. Therefore, the output of the system (y) and the reference to track (r) are:

$$\begin{aligned} y^i &= \begin{bmatrix} LD \\ \theta \\ v_x \end{bmatrix} \\ r^i &= \begin{bmatrix} 0 \\ \theta_r \\ v_{xr} \end{bmatrix} \end{aligned} \tag{3.4}$$

where i is the i-th step along the prediction horizon

The lateral deviation LD is the difference between the predicted position of the vehicle and the corresponding i-th reference pose, as in Figure 3.5.

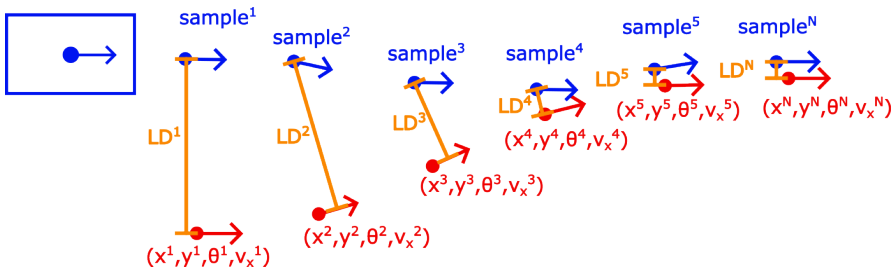

Figure 3.5: Vehicle lateral deviation from the trajectory.

Given the i-th position of the car along the prediction horizon (x_c^i, y_c^i) and

the pose of the i-th reference point $(x_r^i, y_r^i, \theta_r^i)$, the lateral deviation is computed according to Equation 3.5.

$$LD = -x_c^i \sin\theta_r^i + y_c^i \cos\theta_r^i + x_r^i \sin\theta_r^i - y_r^i \cos\theta_r^i \tag{3.5}$$

From Equation 3.5, it is possible to identify two terms dependent on the vehicle state and two that only depend on the reference i-th. Since the objective of the controller is to have $LD = 0$, Equation 3.5 can be written as a function of the vehicle state as follows:

$$[-\sin\theta_r^i, \cos\theta_r^i] \begin{bmatrix} x_c^i \\ y_c^i \end{bmatrix} = -x_r^i \sin\theta_r^i + y_r^i \cos\theta_r^i \tag{3.6}$$

$$[-\sin\theta_r^i, \cos\theta_r^i, 0, 0, 0, 0]x^i = -x_r^i \sin\theta_r^i + y_r^i \cos\theta_r^i \tag{3.7}$$

Combining Equation 3.7 with Equation 3.4, the output of the system and the reference to track can be rewritten as:

$$y^i = C^i x^i$$

$$r^i = \begin{bmatrix} -x_r^i \sin\theta_r^i + y_r^i \cos\theta_r^i \\ \theta_r^i \\ v_{xr}^i \end{bmatrix} \tag{3.8}$$

$$with \quad C^i = \begin{bmatrix} -\sin\theta_r^i & \cos\theta_r^i & 0 & 0 & 0 & 0 \\ 0 & 0 & 1 & 0 & 0 & 0 \\ 0 & 0 & 0 & 1 & 0 & 0 \end{bmatrix}$$

where x^i is the vehicle state (Eq 3.1) computed at the i-th step over the prediction horizon.

Combining all the outputs of the system at each step of the prediction horizon,

and doing the same with the references, one obtains:

$$Y(k) = \begin{bmatrix} y^1(k) \\ y^2(k) \\ \vdots \\ y^N(k) \end{bmatrix}$$
$$R(k) = \begin{bmatrix} r^1(k) \\ r^2(k) \\ \vdots \\ r^N(k) \end{bmatrix} \tag{3.9}$$

where k is the time at which the prediction is realized, and N is the number of steps the prediction horizon is made of.

The cost function in the MPC for the trajectory following task will be realized as Equation 3.3.
Chapter 5, will present the optimization phase to minimize the cost function for trajectory following.

3.3 Sources of power consumption

This section considers the sources of power consumption of an Electric Vehicle and analyzes those that can be affected and reduced by over-actuation.

The sources of energy consumption that depend on the forces acting on the vehicle, whether combustion or electric, are listed in [76]. Forces presented in the paper are:

1. Air resistance against the vehicle.

$$F_{air} = \frac{1}{2}\rho_a C_D A_f (v + v_{wind})^2 \tag{3.10}$$

ρ_a is the mass density of the air.
C_D is the aerodynamic drag coefficient.
A_f is the frontal area of the vehicle.
v is the longitudinal vehicle velocity.
v_{wind} is the frontal wind velocity.

2. Free rolling resistance forces at the tires.

$$F_{roll} = \sum_{i=1}^{4} f_r F_{Ni} \tag{3.11}$$

f_r is the rolling resistance coefficient under free rolling.
F_{Ni} is the normal load on the tire i.

3. The acceleration force action on the vehicle.

$$F_{acc} = M\delta a \tag{3.12}$$

M is the vehicle mass.
δ is the rotational inertia factor.
a is the vehicle acceleration in m/s^2.

4. The grade related force.

$$F_{grade} = Mg\sin\theta \tag{3.13}$$

M is the vehicle mass.
g is the gravitational acceleration.
θ is the slope (positive uphill).

All these sources of energy loss are not directly affected by vehicle over-actuation. In fact, the first term depends only on the aerodynamics coefficient, the properties of the air, the wind, and car speed. Speed is a term that is given as a reference and that the vehicle has to track, and it does not depend on the choice of the actuation. The second term depends on the vehicle mass and the tire rolling resistance coefficient f_r, which is mainly constant, but with further evaluation, the only dependence is from the speed [77]. Also, vehicle acceleration is not directly dependent on over-actuation, of course, it highly affects the vehicle power consumption, but it is more dependent on the aggressiveness of the controller in tracking the reference speed rather than on the torque allocation. An evaluation of the controller aggression will be carried out in Chapter 5, but it is not a source of energy loss that will be minimized in this thesis project because it is preferable to consider the drive

mode (comfort o sport) as a varying parameter that the vehicle's user can select at will. Last, the grade force F_{grade} depends only on the road slope and is the additional force needed to drive uphill. It is a necessary force in addition to the acceleration force F_{acc}, and the same reasoning as before applies. However, in this project, all tests will be conducted on a surface with no inclination.
Beyond these contributions, tires dissipate power due to the sliding part of the contact zone. As presented in [39], the traction force due to tire slip is opposed to the sliding velocity of the contact patch and dissipates power.

5. Power consumed due to opposite direction of the traction force with the contact patch velocity.

$$\begin{aligned} &P_\sigma = -F_x v_s \\ &where \quad v_s = r\omega - v_x = \sigma_x r\omega \end{aligned} \tag{3.14}$$

F_x is the longitudinal force at the contact patch.
v_x is the wheel's longitudinal velocity.
r is the wheel's radius.
ω is the wheel's rotational velocity.
σ_x is the longitudinal slip ratio.
Equation 3.14 can be written as a function of the tire slip ratio as:

$$P_\sigma = -F_x \sigma_x r\omega \tag{3.15}$$

If the longitudinal slip ratio σ_x remains within the stable region, then it is possible to approximate the longitudinal force F_x as linearly dependent to σ_x [43], and Equation 3.15 becomes:

$$P_\sigma = -C_{\sigma_x} F_z r\omega \sigma_x^2 \tag{3.16}$$

C_{σ_x} is the normalized longitudinal slip stiffness.

This power depends on the tire slip ratio, which is directly affected by the torque at the wheels. Therefore, it will be further evaluated, and its contribution to the total energy consumed will be analyzed.

Tire cornering resistance is also a further source of power consumption [18, 38]. Thanks to the lateral sliding movement of the wheel due to a lateral component of the velocity, the tire is able to generate a lateral force opponent to the motion. The sliding is the source of energy loss, and it must be considered.

6. Power consumed by the cornering resistance.

$$P_y = F_y v_y \tag{3.17}$$

P_y is the power consumed by the cornering resistance.
F_y is the cornering resistance.
v_y is the lateral velocity of the wheel.

For small slip angles α it is possible to write the lateral force F_y as linear function of α [43] as:

$$F_y = -C_\alpha F_z \alpha \tag{3.18}$$

C_α is the cornering stiffness.
α is the side slip angle or slip angle.

Same can be done for the wheel's lateral velocity v_y. The wheel's slip angle α is defined as:

$$\alpha = \arctan \frac{v_y}{v_x} \tag{3.19}$$

v_x is the longitudinal velocity of the wheel.

If α is small, then Equation 3.19 can be linearly approximated as

$$\alpha = \frac{v_y}{v_x} \tag{3.20}$$

The lateral velocity can be written as function of α as:

$$v_y = v_x \alpha \tag{3.21}$$

From Equations 3.18 and 3.21, Equation 3.17 can be rewritten as:

$$P_y = -C_\alpha F_z v_x \alpha^2 \tag{3.22}$$

This power depends on the slip angle, which is directly affected by the steering angle of the wheels. Therefore, it will be further evaluated, and its contribution to the total energy consumed will be analyzed.

Important contribution to the power loss is due to the engine efficiency, i.e. the difference between the Electrical Power taken from the battery and the

Mechanical Power provided at the shaft.

7. Energy loss in the engine.

$$P_{enginePowerLoss} = P_{El} - P_{Mech} \tag{3.23}$$

P_{El} is the Electrical Power provided to the engine.
P_{Mech} is the Mechanical Power provided at the shaft.

In literature (Chapter 2), the engine losses are estimated both analytically, computing the power loss in the copper [30, 36], or empirically, exploiting the engine efficiency map [31–33, 35, 61, 63, 64] or directly measuring the Electrical Power and Mechanical Power [34].
In this project, the engine efficiency map (Appendix A) was available and it has been utilized for the engine power loss estimation.
Since the engine efficiency is not constant but depends on the rotational speed and torque at the shaft, and the vehicle utilizes in-wheel engines (see Section 1.1.3), then the energy loss contribution can be affected by the vehicle actuation.

8. Power losses in the transmission.
   As previously said (Section 1.1.3), the vehicle possess in-wheel engines, so there is no transmission and, consequently, no losses due to it.

9. Regenerative braking.
   In the end, another important energy source that helps reduce energy consumption is regenerative braking. It represents an efficient way to recover energy and is already implemented in nowadays road electric vehicle. However, this project work does not take it into account, but focuses more on how over-actuation can reduce energy consumption while driving.

3.3.1 Comparison of Power losses

This Section presents a comparison between the power losses affected by over-actuation, i.e., longitudinal slip losses, power consumed by cornering resistance, and engine power losses. Simulation is exploited to analyze the

three sources of power consumption during different maneuvers: a) driving on a mixed-profile road, b) straight driving (acceleration and steady-state driving), and c) steady-state cornering, as reported in Figure 3.6. In a), the vehicle travels a profile long $560\ m$ where straight and corner sectors are combined. The lateral acceleration is limited to $6\ m/s^2$, and when not constrained by that, it reaches a speed of $90\ km/h$ with a maximum longitudinal acceleration of $5\ m/s^2$. In b), the vehicle accelerates at $5\ m/s^2$ from $0\ km/h$ to $100\ km/h$ and keeps the speed until $400\ m$ when it brakes to stop. In c), only the sector at steady-state cornering long $80\ m$ is analyzed. The vehicle faces the 30m-radius curve with a lateral acceleration of $6m/s^2$ and a constant speed of $47.9\ km/h$. Tests are realized in the IPG CarMaker environment on a vehicle test (Table 3.2) with front steering wheels and torque distributed on all four wheels, where in-wheel engines are modeled.
Here, the energy lost during maneuvers is computed as the time integral of the power from Equations 3.15, 3.17, and 3.23. Longitudinal slip losses are measured only at positive torque values because regenerative braking is not taken into account, and hence energy must be wasted while braking. The RCV-E's engine efficiency characteristic in Figure A.1 is scaled for simulation tests to match the torques and angular velocities available in the vehicle test, keeping the efficiency profile unchanged, as shown in Figure A.2.
Table 3.3 reports the three values of energy consumption for each maneuver.

Tesla Model 3 - FWS, 4WD	
Parameter [Unit]	**Value**
Mass $[kg]$	2108
Total yaw inertia $[kgm^2]$	3954.3
Wheel radius $[m]$	0.33
Engine maximum torque available $[Nm]$	230
Engine maximum angular velocity $[rad/s]$	1000
Gear ratio $[-]$	9.73

Table 3.2: Vehicle parameters in IPG CarMaker for the energy tests.

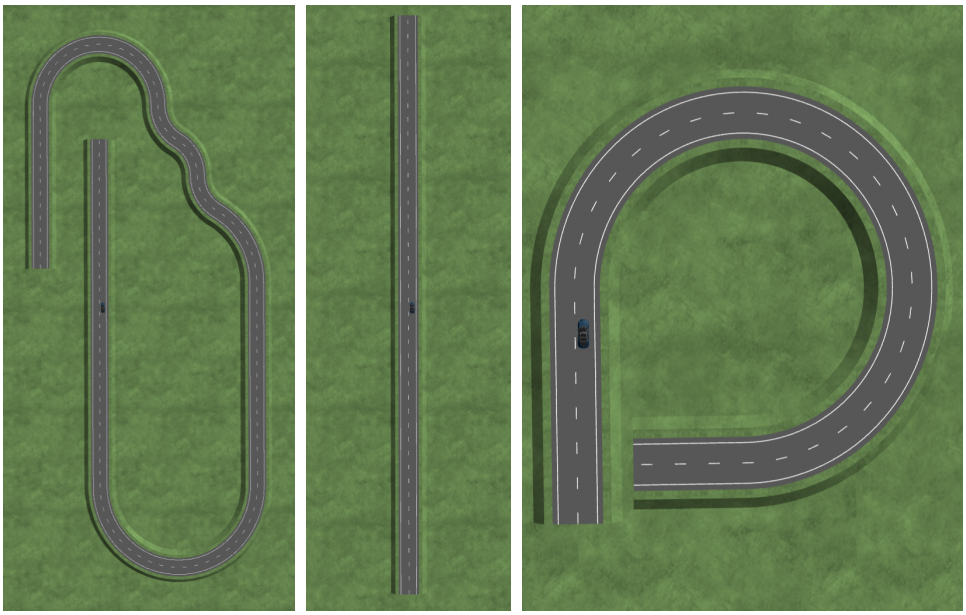

(a) (b) (c)

Figure 3.6: Different road profiles. a) Is a road where the vehicle follows different profiles of velocity. b) Is a straight road where the vehicle accelerates, travels at constant speed, and then brakes. c) Is a circle road, where steady state cornering is investigated.

Energy consumption		
Road	**Source of energy loss due to:**	**Value [kJ]**
Mixed Road (Fig. 3.6a)	Longitudinal slip (Eq 3.15)	14.3
	Cornering resistance (Eq 3.17)	125
	Engine efficiency (Eq 3.23)	344
Straight Road (Fig. 3.6b)	Longitudinal slip (Eq 3.15)	12.0
	Cornering resistance (Eq 3.17)	0.02
	Engine efficiency (Eq 3.23)	266
Circle Road (Fig. 3.6c) Steady-state cornering only	Longitudinal slip (Eq 3.15)	0.130
	Cornering resistance (Eq 3.17)	49.0
	Engine efficiency (Eq 3.23)	47.8

Table 3.3: Energy consumed due to longitudinal slip, cornering resistance, and engine efficiency in different maneuvers.

From Table 3.3, it can be stated that the losses due to longitudinal slip

have less impact on overall energy consumption. Increasing also the maximum longitudinal acceleration during straight and mixed driving to $8\ m/s^2$, the losses due to the slip ratio reach $18.6\ kJ$ and $25.6\ kJ$ respectively, and still play a less relevant role. The cornering resistance losses regard more on the overall energy consumption; a comparison to the other energy terms can be seen in the mixed road where they count for one-third of the energy loss in the engine. This term represents the more significant contribution to the energy loss that can be affected by OA, as also stated in [30], and its minimization will produce the most relevant result in the overall energy minimization.

3.4 Stability Considerations

This Section analyzes the sources of instability for a road vehicle and explains how the stability conditions are considered for a 4WS, 4WD vehicle.
As mentioned in Section 2.4, the main sources of instability for a vehicle are caused by rollover, skidding, and spinning. The first case refers to a vehicle that lifts its inner wheels off the ground when cornering, and this phenomenon is mainly caused by a high-positioned CoG. The other two terms refer to the risk of a vehicle over-steering or under-steering when cornering, and controllers that aim to prevent this are called Yaw Stability control systems. Besides, to properly control the vehicle and guarantee yaw and rollover stability, the wheels force request has to be bounded considering the limitations of the vehicle and road conditions. The following subsections discuss more in detail the three mentioned vehicle stability conditions: rollover, yaw, and tire stability.

3.4.1 Rollover stability

Generally, rollover for road cars is usually not a problem. From [43], can be used the static stability factor to compute an approximated value of the maximum lateral acceleration the vehicle can withstand before experiencing rollover.

$$a_{y\_lift-off} = \frac{l_w}{2h} g \tag{3.24}$$

l_w is the track width.
h is the height of the CoG.

For the vehicle model used in the simulation and for the RCV-E (Table 3.4), the lateral acceleration experienced during cornering is significantly below the

limit value in Eq. 3.24, and therefore, there is no need to consider sources of rollover instability.

	Tesla Model 3	RCV
Parameter [Unit]	**Value**	**Value**
Track width $[m]$	1.68	1.6
CoG height from ground $[m]$	0.545	0.6
$a_{y\_lift-off}$ limit $[m/s^2]$	15.12	13.08

Table 3.4: Vehicle parameters for the maximum lateral acceleration of the car before experiencing rollover.

3.4.2 Yaw Stability

Yaw stability is also focused on the vehicle's lateral dynamics and is monitored using the state variables of yaw rate and the car's side slip angle β, as extensively discussed in Section 2.4.1. However, a vehicle with four steering wheels that can move deliberately sideways is not comparable to a road car constrained laterally by its kinematics. A distinction must be made between straight driving and cornering. During cornering, a 4WS vehicle, as explained in [78], does not need a body sideslip angle β different from zero to generate lateral forces at the rear wheels because these are generated as the wheels are steered by an angle relative to their velocity vector. As a result, a vehicle with four wheel-steering can improve Yaw Stability by more efficiently minimizing the body sideslip angle, as investigated in works [3, 4].
A different scenario regards straight driving and lane-change maneuvers in particular. In this situation, introducing a nonzero body sideslip angle facilitates the maneuvers. As discussed in [78], the vehicle's ability to crab, i.e., steering front and rear wheels in the same direction, accelerates the response of the vehicle's lateral acceleration compared to the case of front wheel-steering. The reason is that lateral forces do not need to wait for the dynamics of the vehicle's rotation around its CoG because they are generated at the moment the wheels begin to steer. As a result, the 4WS vehicles can make lane changes more stably and with less correction by the driver since the lateral acceleration response is shorter. Lane-change maneuvers are also investigated in [79] within KTH, where the vehicle (RCV) was not supposed to be driven by a driver, but an MPC was responsible to perform the maneuver. Here, the crabbing angle β (the body sideslip angle) was meant to be a nonzero reference to guide the vehicle in sideways movements.

In addition to these considerations, as stated in Section 3.2.1, the vehicle must track the desired yaw angle while performing trajectory-following, and this results in a double advantage. First, the vehicle is forced to maintain its direction while performing lane changes and exploits the vehicle's crab ability, and second, it guarantees the vehicle to remain tangentially positioned to the turning path and works as a kind of integral yaw rate reference.
Last, to properly guarantee Yaw Stability, the body sideslip angle has to be minimized during cornering. However, minimizing it has the same result as minimizing the vehicle's lateral velocity when the longitudinal speed is fixed. As mentioned in Section 3.2.1, to perform trajectory-following, the lateral deviation from the reference trajectory is minimized, and applying an additional reference on the vehicle's lateral dynamics, as the one of limiting vy, could partially override the effect of the previous one without additional benefits. In fact, lateral movements are feasible for the RCV-E, and limiting them may result in a superfluous constraint as soon as the lateral displacement and the yaw direction are perfectly tracked.

3.4.3 Wheel Stability

Tire stability concerns the ability of wheels to generate forces and depends on the tire-road friction coefficient μ and the vertical load F_z. In fact, the combination of the lateral and longitudinal forces that can be generated is limited by the so-called friction circle, as in Equation 3.25.

$$F_x^2 + F_y^2 = \mu F_z^2 \tag{3.25}$$

This constraint expresses the relation between the longitudinal and lateral forces, which not only depend on their respective slip values but also on one another. Therefore, counting on this constraint assure feasible requested forces at the wheels and limits them to the stable region.

Chapter 4

System model

This chapter introduces the vehicle model used by the controller (Chapter 5). A compromise is sought to consider all the relevant dynamics and exclude unnecessary ones in the name of simplicity. A less complex model allows the controller to handle fewer variables and achieve better real-time performance, whereas a more complex model assures a more accurate estimation.
This section is divided into two parts: the first part chooses and justifies the vehicle type, and the second assesses numerous tire models and chooses one of them.

4.1 Vehicle model

In this thesis project, the vehicle will be treated as a rigid body with predominant motion in the plane [2]. Only the translation in the plane and the rotation along the z-axis will be regarded (Figure 4.1), whereas the vehicle roll, pitch, and vertical motion will not be part of the system states. Even if the 6 degrees of freedom system was considered sufficient for optimization in [9], an additional simplification was deemed to improve real-time performance on an embedded system [5]. The vehicle state will be represented by its pose and

velocities in the plane, as follows

$$x = \begin{bmatrix} x_{car} \\ y_{car} \\ \theta \\ v_x \\ v_y \\ \dot{\theta} \end{bmatrix} \tag{4.1}$$

where the pose of the car CoG (x_{car}, y_{car}, and θ) are in the global reference frame, whereas the velocities (v_x, v_y, and $\dot{\theta}$) in the vehicle reference frame centered in the CoG of the car, as in Figure 4.1.

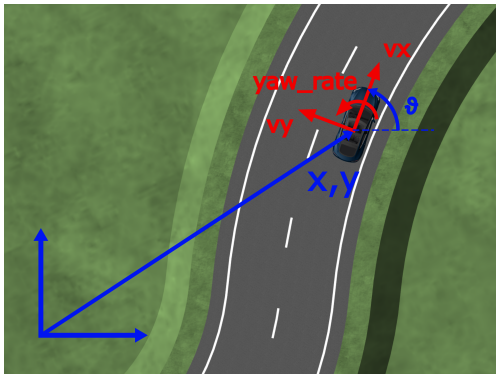

Figure 4.1: Vehicle state representation.

From these considerations, the vehicle system equations are:

$$\begin{aligned} \dot{x}_{car} &= v_x \cos\theta - v_y \sin\theta \\ \dot{y}_{car} &= v_x \sin\theta + v_y \cos\theta \\ \dot{\theta} &= \dot{\theta} \\ \dot{v_x} &= v_y\dot{\theta} + \frac{F_x}{m} \\ \dot{v_y} &= -v_x\dot{\theta} + \frac{F_y}{m} \\ \ddot{\theta} &= \frac{M_z}{J} \end{aligned} \tag{4.2}$$

m is the mass of the car.
J is the yaw moment of inertia of the car

F_x is the longitudinal force acting on the CoG of the car as in Figure 4.3.
F_y is the lateral force acting on the CoG of the car as in Figure 4.3.
M_z is the yaw moment acting on the CoG of the car as in Figure 4.3.

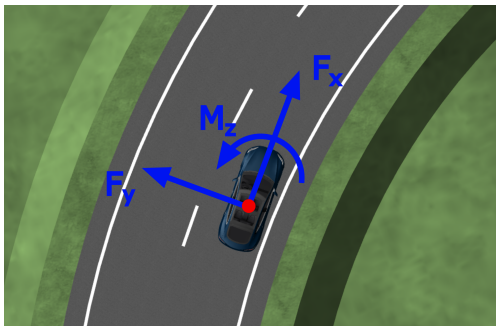

Figure 4.2: Forces acting on the CoG of the car.

Forces in the CoG depend on the forces generated by the wheels. To properly exploit the over-actuation of a Four-Wheel Steering (4WS) and Four-Wheel Driving (4WD) vehicle, all sources of actuation must be taken into account. It follows that a single-track vehicle model (also known as the bicycle model) [45] cannot be used, as it compacts the left-hand side with the right-hand side into one track and reduces the actuation redundancy. Besides, it has been noticed in the literature [18, 38] that separately controlling the torque of the inner and outer track on the vehicle while cornering could affect the power consumption caused by cornering resistance. Thus, a double-track vehicle model [45] is chosen because it can include all the actuation of the RCV-E and separate the left with the right wheel track of the vehicle. In addition to the model utilized in [45], the rear-wheel steering angles are also included,

and forces at the CoG are as in the following equation:

$$\begin{aligned}
F_x &= F_{x,FL}\cos\delta_{FL} + F_{x,FR}\cos\delta_{FR} + F_{x,RR}\cos\delta_{RR} + F_{x,RL}\cos\delta_{RL} - \\
&\quad - F_{y,FL}\sin\delta_{FL} - F_{y,FR}\sin\delta_{FR} - F_{y,RR}\sin\delta_{RR} - F_{y,RL}\sin\delta_{RL} \\
F_y &= F_{x,FL}\sin\delta_{FL} + F_{x,FR}\sin\delta_{FR} + F_{x,RR}\sin\delta_{RR} + F_{x,RL}\sin\delta_{RL} - \\
&\quad + F_{y,FL}\cos\delta_{FL} + F_{y,FR}\cos\delta_{FR} + F_{y,RR}\cos\delta_{RR} + F_{y,RL}\cos\delta_{RL} \\
M_z &= F_{x,FL}(-l_l\cos\delta_{FL} + l_f\sin\delta_{FL}) + F_{y,FL}(l_f\cos\delta_{FL} + l_l\sin\delta_{FL}) + \\
&\quad + F_{x,FR}(l_r\cos\delta_{FR} + l_f\sin\delta_{FR}) + F_{y,FR}(l_f\cos\delta_{FR} - l_r\sin\delta_{FR}) + \\
&\quad + F_{x,RR}(l_r\cos\delta_{RR} - l_b\sin\delta_{RR}) + F_{y,RR}(-l_b\cos\delta_{RR} - l_r\sin\delta_{RR}) + \\
&\quad + F_{x,RL}(-l_l\cos\delta_{RL} - l_b\sin\delta_{RL}) + F_{y,RL}(-l_b\cos\delta_{RL} + l_l\sin\delta_{RL})
\end{aligned} \tag{4.3}$$

where
$F_{x,i}$ is the longitudinal force on the i-th wheel, with i=FL, FR, RR, RL,
$F_{y,i}$ is the lateral force on the i-th wheel,
δ_i is the steering angle of the i-th wheel,
l_f is the distance between the CoG of the car and the front axle,
l_b is the distance between the CoG of the car and the rear axle,
l_l is the distance between the CoG of the car and the left wheels track,
l_r is the distance between the CoG of the car and the right wheels track.

Figure 4.3 show the vehicle model utilized.

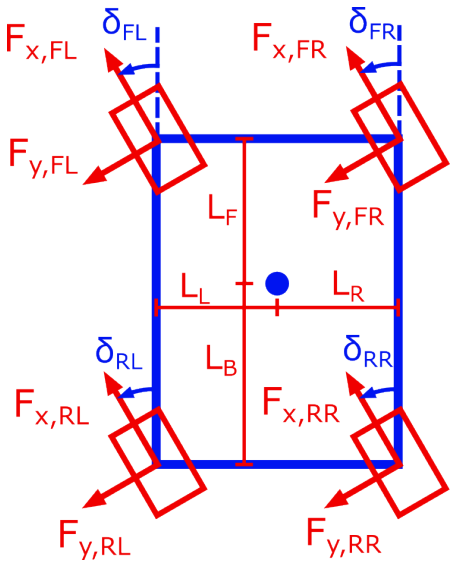

Figure 4.3: Forces acting on the wheels.

4.2 Tire model

Forces at the wheels are functions of the longitudinal slip ratio σ_x and the side slip angle α_i. There are several models for estimating tire forces, including the Direct Torque model (DT), the linear model [43] the Dugoff model (Dugoff, et. al., 1969) [43], and the Magic Formula model (Pacejka and Bakker, 1993) [43]. In this thesis, an analysis to evaluate them in terms of accuracy and simplicity for real-time applications is conducted. The analysis is performed in simulation using the IPG CarMaker environment, and the various models are compared to one another. The tests are carried out as follows.
The driver implemented in CarMaker drives the vehicle test, whose parameters are listed in Table 4.1, on various roadways, as shown in Figure 3.6 with the same acceleration profile reported in Section 3.3.1.

Tesla Model 3	
Parameter [Unit]	**Value**
Mass $[kg]$	2108
Total yaw inertia $[kgm^2]$	3954.3
Distance from front axis to CoG $[m]$	1.43
Distance from rear axis to CoG $[m]$	1.54
Track width $[m]$	1.68
CoG height from ground $[m]$	0.578
Wheel radius $[m]$	0.33
Tire cornering stiffness C_α $[N/rad]$	14.5
Longitudinal tire stiffness C_σ $[-]$	32

Table 4.1: Vehicle parameters in IPG CarMaker for the tire forces experiment.

Longitudinal and lateral tire forces are evaluated as follows.
For the tire longitudinal forces F_{xi}, a direct torque actuation model (Eq 4.4), a slip ratio linear model (Eq 4.5), and the Dugoff model (Eq 4.6) are examined. The longitudinal forces obtained by these models are compared with the actual longitudinal forces measured during the three simulations, and the RMSE values are reported in Table 4.2. The model implemented in CarMaker to simulate the behavior of the tires is a Pacejka model (Magic Formula 5.2). For the wheel lateral forces F_{yi}, the same approach is used. The side slip angle linear model (Eq 4.5) and the Dugoff model (Eq 4.6) are investigated and compared with the actual lateral forces measured during the

three simulations, and the RMSE values are reported in Table 4.3. For the Circle Road (Fig 3.6c) values corresponds only to the steady state cornering phase because acceleration and braking are investigated in the other Roads. During the tests, the values of σ_x and F_z for each wheel are assumed to be measured, while the values of α are computed geometrically from the the vehicles velocities v_x, v_y and $\dot{\theta}$. The direct torque actuation model is defined in the following equation

$$F_{xi} = \frac{T_i}{r_w} \tag{4.4}$$

Where r_w is the wheel radius. The linear tire model is

$$\begin{aligned} F_{xi} &= C_\sigma F_{z,i} \sigma_{x,i} \\ F_{yi} &= C_\alpha F_{z,i} (\delta_i - \alpha_i) \end{aligned} \tag{4.5}$$

where C_σ is the longitudinal tire stiffness, C_α is the cornering stiffness of the tire, F_z is the vertical force on the tire.

The Dugoff's model of the forces at the tires is

$$\begin{aligned} F_{xi} &= C_\sigma \frac{\sigma_{x,i}}{1+\sigma_{x,i}} f(\lambda) \\ F_{xi} &= C_\alpha \frac{\tan\alpha_i}{1+\sigma_{x,i}} f(\lambda) \\ where& \\ \lambda &= \frac{\mu F_{z,i}(1+\sigma_{x,i})}{2\{(C_\sigma \sigma_{x,i})^2 + (C_\alpha \tan\alpha_i)^2\}^{\frac{1}{2}}} \\ and& \\ f(\lambda) &= \begin{cases} (2-\lambda)\lambda, & \lambda < 1 \\ 1, & \lambda \geq 1 \end{cases} \end{aligned} \tag{4.6}$$

where μ is the tire-road friction coefficient.

Longitudinal Forces F_x		
Road	**Model**	**RMSE**
Mixed Road (Fig. 3.6a)	Direct Torque (Eq 4.4)	72.9
	Linear Model (Eq 4.5)	181.1
	Dugoff Model (Eq 4.6)	126.5
Straight Road (Fig. 3.6b)	Direct Torque (Eq 4.4)	84.1
	Linear Model (Eq 4.5)	365.6
	Dugoff Model (Eq 4.6)	194.6
Circle Road (Fig. 3.6c) Steady-state cornering only	Direct Torque (Eq 4.4)	47.6
	Linear Model (Eq 4.5)	63.2
	Dugoff Model (Eq 4.6)	41.7

Table 4.2: RMSE of the longitudinal tire forces compared to the measured ones in IPG CarMaker. The RMSE in the table is the average between the RMSEs computed for each wheel.

From the results in Table 4.2, it can be derived that the DT model is generally the most accurate. Especially, from a deeper analysis, it approximates better than the other ones the values of F_x during the acceleration and braking phases ($5\ m/s^2$ acceleration, $-8\ m/s^2$ braking), as can be noticed in Figure 4.4a. However, by requesting a stronger deceleration phase, the system becomes unstable, and in the nonlinear area, the Dugoff model has the best results (Figure 4.4b), whereas the linear model diverges to unrealistic values because the slip ratio is in the unstable nonlinear region. The RMSE values for F_x during the deceleration phase on Road 2 at $-10\ m/s^2$ are [DT=2243.3, Dugoff=517.4, Linear=1.29×10^5]. It should be mentioned that the tests were performed without a braking stability control system (ABS), and stability solutions, discussed in Section 3.4, will have to be taken into account in the control to keep the system in the stable area as one of the objects of the research. Despite this, the linear model has the worst results during acceleration and braking when F_x is high and reaches values close to F_z ($\mu = 1$) but remains in the stable area (Figure 4.4a). In fact, the linear region exists only for small values of σ_x, and while approaching the maximum values of the longitudinal force, the relation becomes nonlinear. Differently, the DT model does not seem to suffer from this problem as soon as the system remains in the stable area.
During straight steady-state driving, the models that depend on the slip ratio have better results than the DT model (Figure 4.5). The RMSE values for

F_x during steady-state driving at 100 km/h on Straight Road (Fig. 3.6b) are [DT=43.2, Dugoff=1.87, Linear=1.82]. The DT model generally estimates a longitudinal force above the measured one, this is because the measure of slip ratio allows the two models to consider the information of the rolling losses, which results in a lower force at the tires for the same torque.
From this reflection, under the assumption of tire stability (Section 3.4), the option that presents a good balance between accuracy and simplicity is the **Direct Torque model** (Eq. 4.4). So, no tire dynamics will be considered for the wheel longitudinal force generation, as in previous works [33, 37, 40, 61–63].

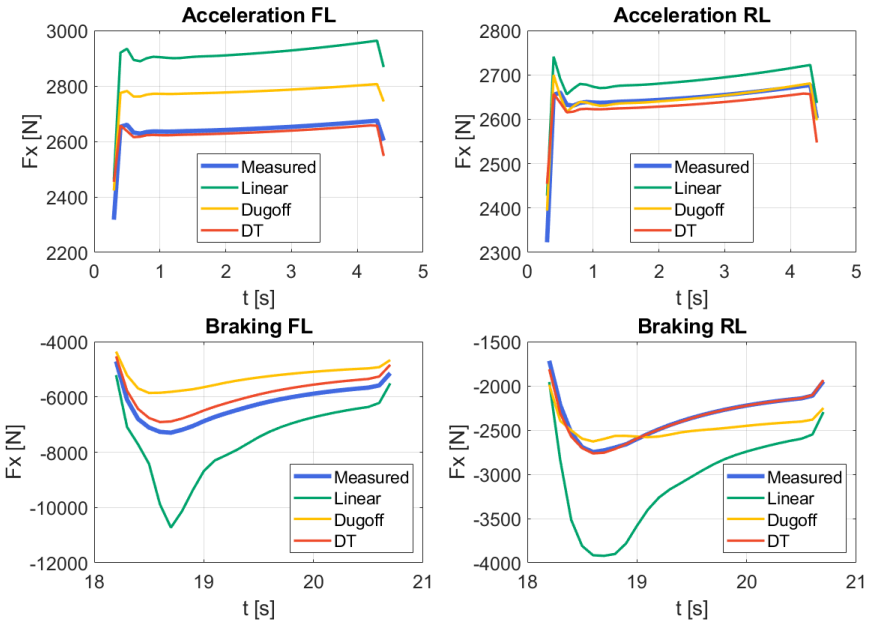

(a)

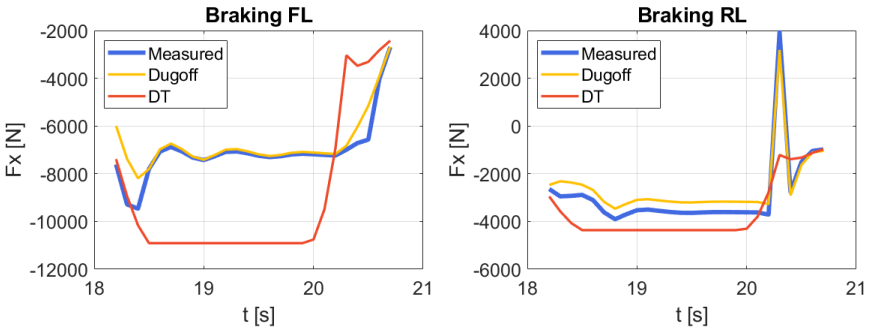

(b)

Figure 4.4: Longitudinal tire forces representation. a) Represents the acceleration and braking phase at $5\ m/s^2$ and $-8\ m/s^2$ for the left front and rear wheels. The right side is symmetrical because the car was driving straight. b) Represents the braking phase at $-10\ m/s^2$ for the left front and rear wheels. In these figures, the linear model is not represented because it has a divergent behaviour and was out of scale.

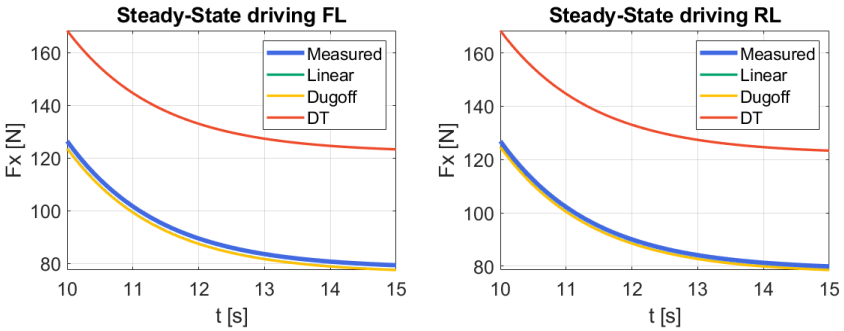

Figure 4.5: Longitudinal tire forces representation during steady-state straight driving at 100 km/h. The linear and Dugoff models are superimposed in the figures.

Lateral Forces F_y		
Road	**Model**	**RMSE**
Mixed Road (Fig. 3.6a)	Linear Model (Eq 4.5)	262.2
	Dugoff Model (Eq 4.6)	262.3
Straight Road (Fig. 3.6b)	Linear Model (Eq 4.5)	209.5
	Dugoff Model (Eq 4.6)	209.7
Circle Road (Fig. 3.6c) t=6.6s-13.0s	Linear Model (Eq 4.5)	260.9
	Dugoff Model (Eq 4.6)	237.8

Table 4.3: RMSE of the lateral tire forces compared to the measured ones in IPG CarMaker. The RMSE in the table is the average between the RMSEs computed for each wheel.

From Table 4.3, one noticeable aspect to highlight is that during straight driving (Straight Road Fig. 3.6b), the two models present a relevant RMSE for estimating the lateral tire forces F_y. The reason is that there is an offset between the estimated lateral forces, around zero when straight driving, and the measured ones, a value compatible with the RMSE. The offset is negative for the left wheels and positive for the right wheels. Assumptions suggest the effect of an additional angle, such as the Toe or Camber angle, however since this is an average offset of 200 N per side (which balances itself out) further investigation was not done.
Beyond this result, the most interesting case to analyze lateral forces is during cornering and so Circle Road (Fig. 3.6c). Here, the two models estimate more precisely the lateral forces at the inner wheels, whereas the overall error derives

mainly from the outer track, as in Figure 4.6a. The same behavior can be observed during the "snake" section in the Mix Road (Fig. 3.6a), as can be seen in Figure 4.6b.
To conclude, results show no significant differences between the two models, and both can estimate lateral forces effectively. As a result, the **Linear model** (Eq. 4.5) is the optimal alternative because fewer parameters need to be measured, and the future implementation of the algorithm requires fewer sensors. Besides, the wheel's sideslip angle α can be computed geometrically from the vehicle's velocities in the CoG $(v_x, v_y, \dot{\theta})$.

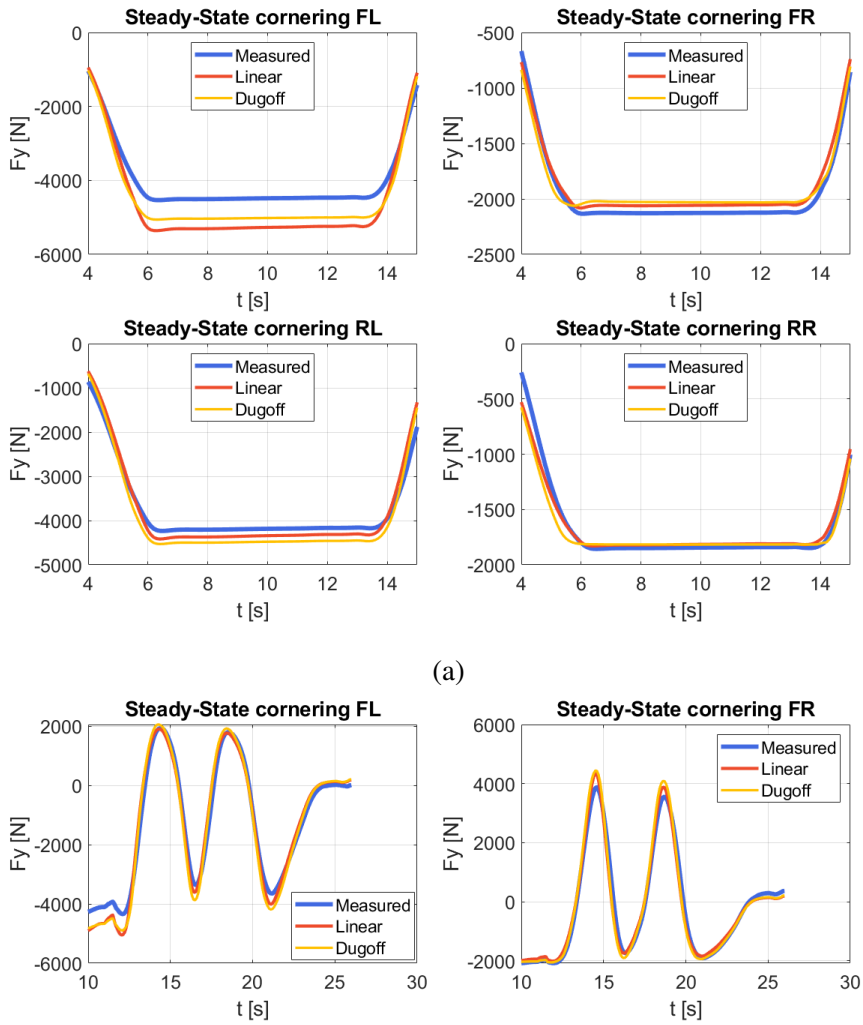

(a)

(b)

Figure 4.6: Lateral tire forces representation. a) Shows the lateral tire forces estimation during steady-state cornering. b) Shows the lateral tire forces estimation during a "snake" section.

Chapter 5

Trajectory-following control strategy

This Chapter introduces the main issues concerning the control strategies adopted to reach the purpose of the thesis (Section 1.3): perform trajectory-following while guaranteeing vehicle stability and minimizing energy consumption. In particular, the controller will be implemented on the RCV-E (Chapter 7), and it must be sufficiently agile and fast to prevent over-run errors in its execution. However, the complexity of handling multiple tasks can be critical to real-time performance. Therefore, before introducing solutions to minimize energy consumption, the structure of the controller must be defined to address an embedded implementation and drive the vehicle along the desired trajectory.
This project develops a control strategy based on MPC to perform trajectory-following because it predicts the state of the car along the route. Besides, optimal control is a necessary solution when exploiting the redundancy of Over-Actuation to accomplish additional tasks. In this regard, preliminary considerations must be made.
The first part of this Chapter deals with the nonlinearities in the vehicle model concerning the MPC (Section 5.1), and the second one (Section 5.2) introduces the problem related to the control rate of the different components of the system. Faster dynamics must be controlled with a sufficiently high sample rate, while slower dynamics can be handled less quickly and exploit optimal control.
Later, Section 5.3 presents the results of these solutions, while Section 5.4 introduces and demonstrates the benefit of an integral action on the longitudinal velocity to better follow the reference.

5.1 LTV-MPC for trajectory-following

From Section 3.2, the MPC is responsible to track the lateral deviation, the yaw angle, and the longitudinal velocity references by minimizing the cost function defined in the Equations 3.3 and 3.9. However, the system model, defined in Chapter 4, is nonlinear, and consequently, the MPC cost function has to be solved by a nonlinear optimizer. From simulations, the outcomes highlight the unfeasibility of a nonlinear MPC for trajectory following if the algorithm has to guarantee real-time performance and, in order not to give up the use of vehicle state prediction along the route, it was decided to opt for a Linear Time-Varying MPC (LTV-MPC).
At each control-sample step, the MPC algorithm linearizes the system's equations using a first-order Taylor approximation along the predicted state trajectory computed at the previous sample time. As a result, at time k, N triplets [A_{k+i}, B_{k+i}, C_{k+i}] are obtained, with $i = 0, ..., N-1$ and N the prediction horizon steps. The linearized system becomes as in the following equation

$$\begin{cases} x(k+i+1) = A_{k+i}x(k+i) + B_{k+i}u(k+i) + G_{k+i} \\ y(k+i) = C_{k+i}x(k+i) \end{cases} \qquad i = 0, ..., N-1 \tag{5.1}$$

where

$$\begin{aligned} G_{k+i} = f(\hat{x}(k+i|k), u^o(k+i|k-1)) - \\ - (A_{k+i}\hat{x}(k+i|k) + B_{k+i}u^o(k+i|k)) \end{aligned} \tag{5.2}$$

is the linearization error computed at time k along the prediction horizon.

Defining the predicted output $Y(k)$, the reference values $R(k)$, and the control

action $U(k)$ along the predicted horizon N as:

$$Y(k) = \begin{bmatrix} y(k+1) \\ y(k+2) \\ \vdots \\ y(k+N) \end{bmatrix} \quad U(k) = \begin{bmatrix} u(k) \\ u(k+1) \\ \vdots \\ u(k+N-1) \end{bmatrix} \quad R(k) = \begin{bmatrix} r(k+1) \\ r(k+2) \\ \vdots \\ r(k+N) \end{bmatrix} \tag{5.3}$$

The LTV-MPC can be formulated as a quadratic problem, as follows.

$$\begin{aligned} \min_{U(k)} J \quad &= [R(k) - Y(k)]^T Q_0 [R(k) - Y(k)] + U^T(k) R_0 U(k) \\ s.t. \quad & x(k+i+1) = A_{k+i} x(k+i) + B_{k+i} u(k+i) + G_{k+i} \\ & y(k+i) = C_{k+i} x(k+i) \\ & LB \leq V \cdot U(k) \leq UB \\ & \forall\, i = 0, \ldots, N-1 \end{aligned} \tag{5.4}$$

where Q_0 and R_0 are the positive definite weight matrices, V is a matrix for the constraints definition, and LB and UB are the lower and upper bounds of the constraints.

Please refer to Appendix B for the mathematical derivation of LTV-MPC equations that can be directly implemented into code.

5.2 Two-level control strategy

Chapter 4 presented the system model that includes the vehicle's and the tire's behavior, whose dynamics are different. As a result, when simulating the prediction of the vehicle states along the prediction horizon, problems arise, even employing the nonlinear system model. Using a time step relatively high, comparable with $0.1\ s$, the state prediction turns out to be incorrect and often divergent, especially at low speeds, as shown in Figures 5.1. Whereas, with a higher sample rate ($0.02\ s$), the problem is reduced or disappears, as in

Figure 5.2. Here, the results are obtained by discretizing the system model and estimating the wheel's sideslip angles with the car's velocities in the CoG $(v_x, v_y, \dot{\theta})$ in such a way predicting the state of the vehicle allows predicting the wheels' sideslip angles along the horizon. A constant input is applied to the system model, and the states along the prediction horizon are derived.

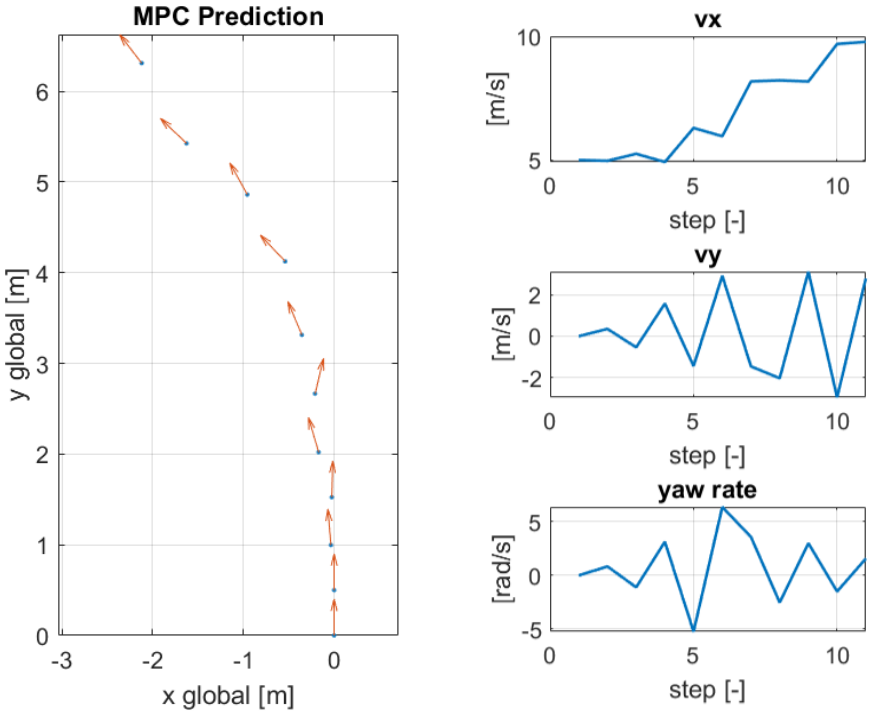

(a) (b)

Figure 5.1: MPC prediction. Sampling time 0.1s, initial speed 5 m/s, wheel torque 100Nm, front steering angles 0.1 rad, rear steering angles -0.05 rad.

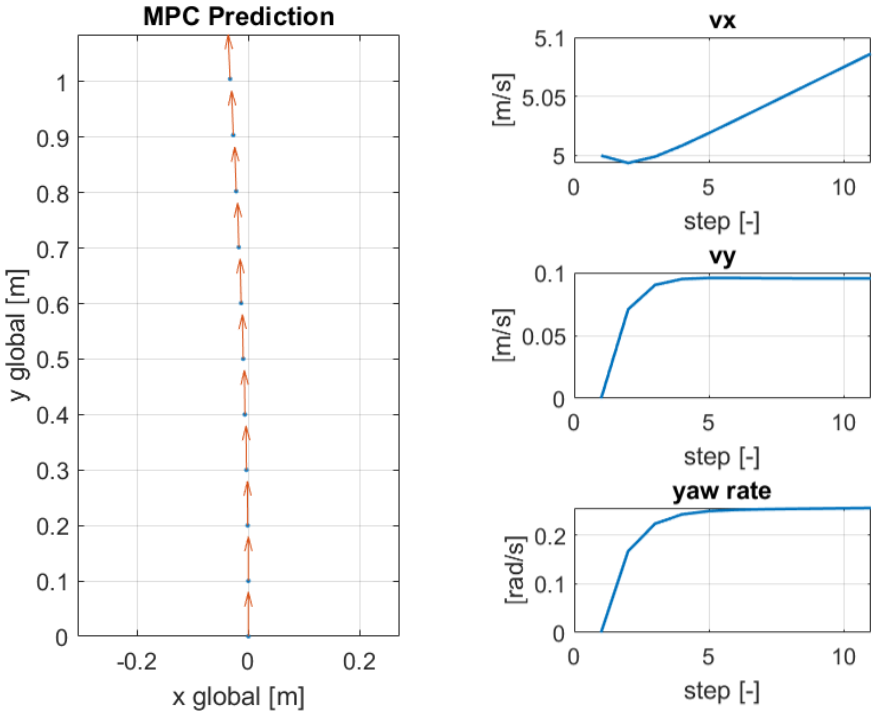

(a) (b)

Figure 5.2: MPC prediction. Sampling time 0.02s, initial speed 5 m/s, wheel torque 100Nm, front steering angles 0.1 rad, rear steering angles -0.05 rad.

Figures 5.1 and 5.2 show that a sampling time (Ts) of $0.1s$ produces some oscillations in the predicted states of the vehicle, whereas with $Ts = 0.02s$ the prediction is smoother. Additional tests showed that by reducing the initial velocity v_x or increasing the sampling time, the oscillations increase until divergence Figure 5.3.

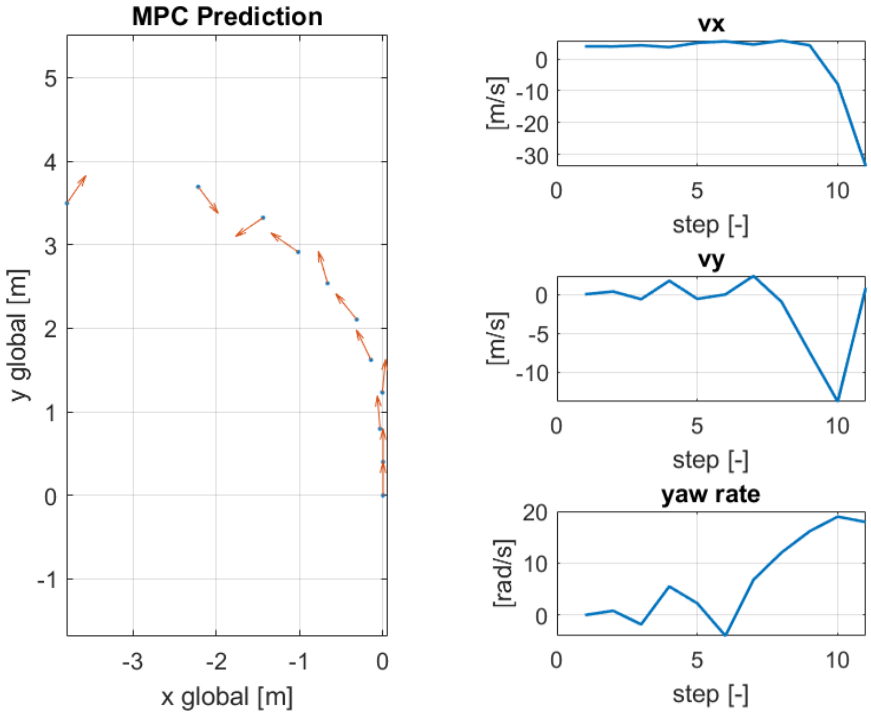

(a) (b)

Figure 5.3: MPC prediction. Sampling time 0.1s, initial speed 4 m/s, wheel torque 100N, front steering angle 0.1 rad, rear steering angle -0.05 rad.

To find an explanation for this phenomenon, the eigenvalues of the velocity system $(v_x, v_y, \dot{\theta})$ are analyzed in different state conditions (Table 5.1).

Condition [m/s, m/s, rad/s]	**eig 1**	**eig 2**	**eig 3**
$v_x = 2, \quad v_y = 0, \quad \dot{\theta} = 0$	0	-70	-84
$v_x = 5, \quad v_y = 0, \quad \dot{\theta} = 0$	0	-29	-33
$v_x = 10, \quad v_y = 0, \quad \dot{\theta} = 0$	0	-15 + 1.6i	-15 - 1.6i
$v_x = 5, \quad v_y = 1, \quad \dot{\theta} = 1$	0.25	-33	-26
$v_x = 15, \quad v_y = 1, \quad \dot{\theta} = 1$	-0.18	-10+1.8i	-10-1.8i

Table 5.1: Eigenvalue of the system $[v_x, v_y, \dot{\theta}]$ linearized in different points.

Table 5.1 shows that the system's eigenvalues are significantly high in absolute value for low car speeds (vx). Consequently, the current system has

too fast dynamics to be controlled at a low rate, and the prediction step must be sufficiently short to be compatible with the rapid dynamics. If this is not the case, considering the system's states constant for a long prediction step generates oscillations in the prediction.
The prediction step of the MPC, on the other hand, cannot be chosen arbitrarily; it must be greater or equal to the control step, and decreasing the control step excessively jeopardizes real-time performance. Besides, the system is expected to follow the reference trajectory for each velocity, and it must guarantee reliability also at a low speed. In particular, the problem derives from the forces generated at the wheels that depend on the sideslip angles and can vary at high frequencies. So, to solve this problem, the control strategy must separate the different dynamics to control them at a different rate.

The idea is to solve the MPC problem using, as control inputs, the forces at the wheels in the vehicle's reference frame (Figure 5.5a). In this way, the MPC can be executed at a low rate, reducing problems in the programming solver, and the system employed is presented in Equation 5.5. A faster low-level controller translates the forces from the vehicle's reference frame into the wheel's frame (Figure 5.5b) and derives the torques and steering angle values (Eq. 5.6).
Figure 5.4 shows the structure of the controller.

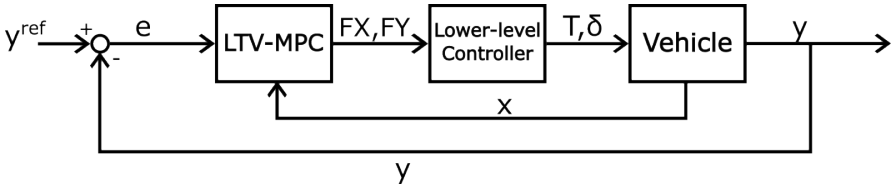

Figure 5.4: Structure of the controller.

Regarding the prediction and control rates of the MPC and the control rate of the lower-level controller, problems are now extinguished. The upper-level system (Eq. 5.5) has zero eigenvalues for each condition, so its variation depends only on the inputs applied and not on its current state. As a result, the prediction step does have to be kept small, and consequently, the control step of the LTV-MPC can be sufficiently high to exploit an optimizer in real-time. These two parameters can be changed depending on the real-time necessities; however, 10 Hz is an appropriate control rate for a controller to have a reaction time slightly better than any driver.
Concerning the lower-level control rate, it is decided to set it at 100 Hz in order to assure a sufficiently fast controller for the wheels' dynamics.

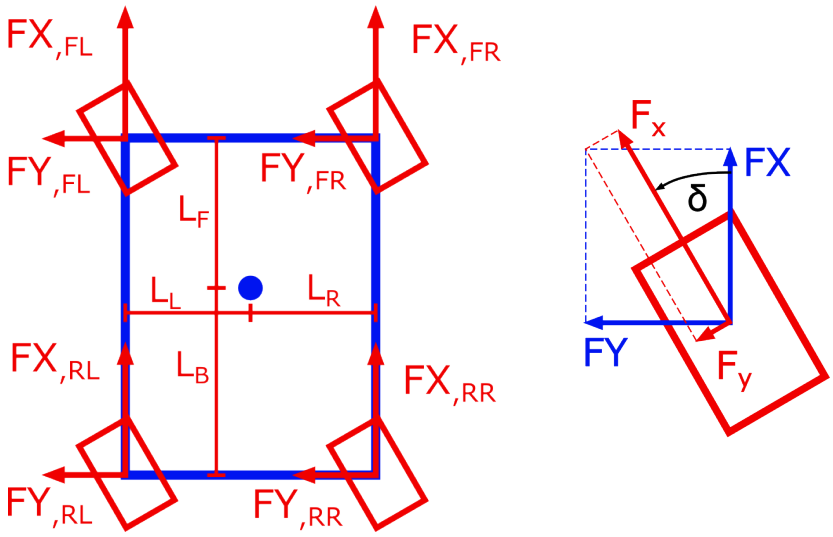

(a) (b)

Figure 5.5: Two-level model. a) Is the model utilized by the LTV-MPC. b) Is the model utilized by the lower level controller to allocate the forces for each wheel.

The upper-level controller system equations are defined as follows,

$$
\begin{aligned}
&\dot{x}_{car} = v_x \cos\theta - v_y \sin\theta \\
&\dot{y}_{car} = v_x \sin\theta + v_y \cos\theta \\
&\dot{\theta} = \dot{\theta} \\
&\dot{v_x} = v_y\dot{\theta} + \frac{F_x}{m} \\
&\dot{v_y} = -v_x\dot{\theta} + \frac{F_y}{m} \\
&\ddot{\theta} = \frac{M_z}{J} \\
&with \\
&F_x = FX_{FL} + FX_{FR} + FX_{RR} + FX_{RL} \\
&F_y = FY_{FL} + FY_{FR} + FY_{RR} + FY_{RL} \\
&M_z = -(FX_{FL} + FX_{RL}) * l_l + (FX_{FR} + FX_{RR}) * l_r + \\
&\qquad (FY_{FL} + FY_{FR}) * l_f - (FY_{RR} + FY_{RL}) * l_b
\end{aligned}
\tag{5.5}
$$

where the control variable $U(k)$ in Equation 5.4 is represented by the term:
$U(k) = [FX_{FL}, FX_{FR}, FX_{RR}, FX_{RL}, FY_{FL}, FY_{FR}, FY_{RR}, FY_{RL}, \ldots, N\ times]^T$

Whereas, the low-level system equations are:

$$
\begin{aligned}
F_{x,i} &= FX_i\ cos(\delta_i) + FY_i\ sin(\delta_i) \\
F_{y,i} &= -FX_i\ sin(\delta_i) + FY_i\ cos(\delta_i) \\
T_i &= F_{x,i} * r_w \\
\delta_i &= \frac{F_{y,i}}{C_\alpha * F_{z_i}} + \alpha_i \\
i &= FL, FR, RR, RL
\end{aligned}
\tag{5.6}
$$

In addition, this approach allows the wheel stability to be considered, in terms of the friction circle (Section 3.4.3), directly in the MPC solution. To include this nonlinear constraint in the LTV-MPC, the friction circle is approximated to an octagon, as in Figure 5.6. The combination of longitudinal and lateral forces in the vehicle's reference frame is bounded to stay inside the octagon to remain in the stable region. The sides of the polygon can be expressed as linear constraints in the cost function.

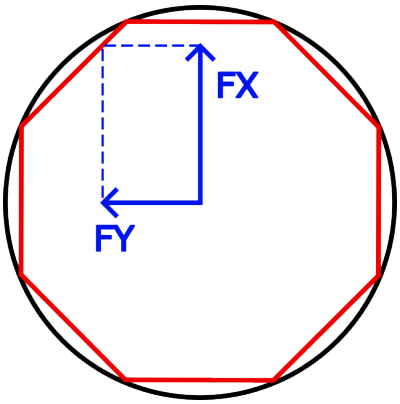

Figure 5.6: Friction circle constraint applied to the wheel's forces in the vehicle's reference frame.

5.3 Results

This Section presents the simulation results obtained to evaluate the controller performance for trajectory-following. The tests are performed in IPG CarMaker [70] (Section 3.1) considering three different maneuvers (Figure 3.6): a) mixed driving that combines braking and acceleration during cornering and straight driving, b) straight driving (acceleration, steady-state

driving, braking), and c) steady-state cornering.
In a), the vehicle travels a profile long 560 m where straight and corner sectors are combined. It should follow a reference speed set at 90 km/h for straight sectors and 40 km/h for curved sectors. The reference path starts on the right lane and, after 20 m, slides to the left, with the reference yaw angle pointing forward, to reach the road's centerline to mimic a partial lane-change maneuver. Then, it continues on the road's centerline to allow a visual assessment of the trajectory-tracking performance in addition to numerical values. Before the vehicle reaches the end of the track, the reference speed drops from 90 km/h to 0 km/h in 30 m.
In b), the reference speed changes from 0 km/h to 100 km/h in 20 m, and the reference path performs a double lane-change maneuver starting after 50 m for 130 m to mimic an overpass. Besides, the reference speed increases to 130 km/h, and the vehicle travels at steady-state until 800 m, where the speed reference decreases to 0 km/h in 50 m.
In c), only the sector at steady-state cornering long 80 m is analyzed. The vehicle faces the 30m-radius curve at the required speed of 50 km/h.

These tests assess the Lateral Deviation (LD) from the desired trajectory and the tracking of the reference Longitudinal Velocity (VEL) and Yaw angle (YAW). For each of these components, the RMSE and the maximum values of the difference between the references and the vehicle's output are provided. In particular, to better mimic the behavior of cars' cruise control, where the driver can set any desired velocity, the speed reference given to the vehicle during these tests is not always constant and does not match the vehicle's thrust limits. Therefore, the maximum value of the difference between the vehicle's speed and the desired one loses meaning, and won't be considered.
To validate better the LTV-MPC, six combinations of the prediction horizon are analyzed.
1) A prediction horizon (Th) of 2 s with a sampling time (Ts) of 0.2 s and 10 samples (N).
2) A prediction horizon of 1.5 s with a sampling time of 0.15 s and 10 samples.
3) A prediction horizon of 1 s with a sampling time of 0.1 s and 10 samples.
4) A prediction horizon of 1.4 s with a sampling time of 0.2 s and 7 samples.
5) A prediction horizon of 1.5 s with a sampling time of 0.3 s and 5 samples.
6) A prediction horizon of 1 s with a sampling time of 0.2 s and 5 samples.

As a quadratic programming optimizer to solve the cost function of the LTV-MPC, DAQP [80, 81] was used. The reasons that led to the use of this

software aim to solve embedding necessities, as explained in Section 7.1, and for coherence, the same optimizer employed on the RCV-E is adopted in the simulation.

Table 5.2, 5.3, and 5.4 show the results.

Mixed Road Fig. 3.6a					
MPC params.	**LD RMSE**	**LD MAX**	**YAW RMSE**	**YAW MAX**	**VEL RMSE**
Th=2.0s, Ts=0.20s, N=10	0.193	0.411	0.024	0.148	2.20
Th=1.5s, Ts=0.15s, N=10	0.171	0.362	0.019	0.134	2.22
Th=1.0s, Ts=0.10s, N=10	0.124	0.371	0.014	0.092	2.66
Th=1.4s, Ts=0.20s, N= 7	0.217	0.417	0.022	0.158	2.26
Th=1.5s, Ts=0.30s, N= 5	0.307	0.598	0.034	0.191	2.26
Th=1.0s, Ts=0.20s, N= 5	0.176	0.363	0.021	0.134	2.60

Table 5.2: Results of the two-level controller for the trajectory following performance on the Mix Road Fig. 3.6a.

Straight Road Fig. 3.6b					
MPC params.	**LD RMSE**	**LD MAX**	**YAW RMSE**	**YAW MAX**	**VEL RMSE**
Th=2.0s, Ts=0.20s, N=10	0.087	0.455	0.006	0.021	2.23
Th=1.5s, Ts=0.15s, N=10	0.076	0.399	0.010	0.050	2.61
Th=1.0s, Ts=0.10s, N=10	0.078	0.397	0.053	0.290	3.51
Th=1.4s, Ts=0.20s, N= 7	0.086	0.452	0.019	0.098	2.67
Th=1.5s, Ts=0.30s, N= 5	0.110	0.523	0.027	0.128	2.50
Th=1.0s, Ts=0.20s, N= 5	0.075	0.432	0.050	0.265	3.43

Table 5.3: Results of the two-level controller for the trajectory following performance on the Straight Road Fig. 3.6b.

Circle Road Fig. 3.6c					
MPC params.	**LD RMSE**	**LD MAX**	**YAW RMSE**	**YAW MAX**	**VEL RMSE**
Th=2.0s, Ts=0.20s, N=10	0.347	0.348	0.007	0.012	1.51
Th=1.5s, Ts=0.15s, N=10	0.268	0.270	0.005	0.009	1.35
Th=1.0s, Ts=0.10s, N=10	0.176	0.193	0.004	0.009	1.19
Th=1.4s, Ts=0.20s, N= 7	0.382	0.383	0.010	0.013	1.40
Th=1.5s, Ts=0.30s, N= 5	0.561	0.562	0.016	0.020	1.48
Th=1.0s, Ts=0.20s, N= 5	0.279	0.289	0.014	0.020	1.28

Table 5.4: Results of the two-level controller for the trajectory following performance for steady-state cornering condition long 80 m on the Circle Road Fig. 3.6c.

From Tables 5.2, 5.3, and 5.4, it is possible to notice that lateral deviation mostly depends on the sampling time of the MPC. When the samples are closer to one another, the vehicle tends to cut less of the path, and the lateral deviation is smaller. The prediction horizon has some impact as well, though less. When the MPC's vision field is shorter, it tries to stick as close as possible to the path just ahead of it, disregarding points farther away; therefore, it does not jeopardize the tracking of the near points for the remote ones. Although a driver may be tempted to cut corners, the vehicle is expected to follow the path accurately, especially since no upper limits on lateral deviation are considered. Therefore, the optimal choice regarding lateral deviation is for a prediction horizon of 1 s with 10 samples, and during cornering (Table 5.4), it has the best performance.
Regarding yaw angle tracking, the same behavior affects the result. The more the vehicle cuts corners, the less tangent its direction will be to the trajectory. However, beyond this, another phenomenon affects the results. When severe braking is required, as in Straight driving where the desired velocity drops from 130 km/h to 0 km/h in 50 m, the vehicle loses the desired direction. The reason is that the MPC tries to reduce the longitudinal velocity by changing the direction of the car despite the reference yaw angle. By increasing the weight of the desired yaw angle, this problem can be decreased but not totally removed, especially for high speed. However, the longer the prediction horizon, the lower this problem, and for the 2s-prediction horizon, it becomes irrelevant. A solution that solves this problem even for lower horizons is presented in Section 5.4; even if for lower velocity, such as braking from

90 km/h to 0 km/h (Mixed Road), this problem is no more present for every value of Th.
The best performance between the corners cut and heavy brakes are provided by a higher number of samples (N=10), and Th=1.5 s represents a good trade-off regarding yaw rate tracking performance.
Regarding speed tracking, the differences during steady-state cornering (Circle road) are due to the fact that if the vehicle keeps a more inner path, it will have lower velocity, whereas if it does not cut turns, it will travel a little bigger circles and consequently can keep the speed higher. Beyond this, if the MPC has a longer prediction horizon (Th), it can predict before the variation of the reference velocity along the trajectory, and consequently, it will have an earlier response and better tracking. However, analyzing the case when the vehicle is at steady-state during straight driving, as on a Straight road, when it is required to track 130 km/h for more than 400 m (Figure 5.7), a small error in the velocity at steady-state is present. Table 5.5 shows the longitudinal speed of the vehicle during steady-state straight driving and cornering. For the straight driving situation, it is considered the car's speed at the end of the steady-state sector at 650 m, as in Figure 5.7, which remains constant within this section. For cornering, the section considered is the turn (80 m long) while the vehicle has a constant speed, which is measured at the end of the steady-state sector.

Steady-state speed		
MPC params.	**Straight driving**	**Cornering**
Th=2.0s, Ts=0.20s, N=10	128.80 km/h	44.37 km/h
Th=1.5s, Ts=0.15s, N=10	128.78 km/h	45.13 km/h
Th=1.0s, Ts=0.10s, N=10	128.64 km/h	45.70 km/h
Th=1.4s, Ts=0.20s, N= 7	128.72 km/h	44.98 km/h
Th=1.5s, Ts=0.30s, N= 5	128.67 km/h	44.65 km/h
Th=1.0s, Ts=0.20s, N= 5	128.57 km/h	45.40 km/h

Table 5.5: Steady-state velocity of the vehicle during straight driving and cornering. During straight driving the reference velocity is 130 km/h, during cornering is 50 km/h.

50 km/h for cornering is a speed quite at the limits of the vehicle friction, but even lowering the reference, the error remains substantially high. Failure to reach the appropriate speed during stationary driving is due to unmodeled

opposing forces (air drag and rolling resistance). To compensate for these disturbances, an integral action is added to the LTV-MPC and discussed in Section 5.4.

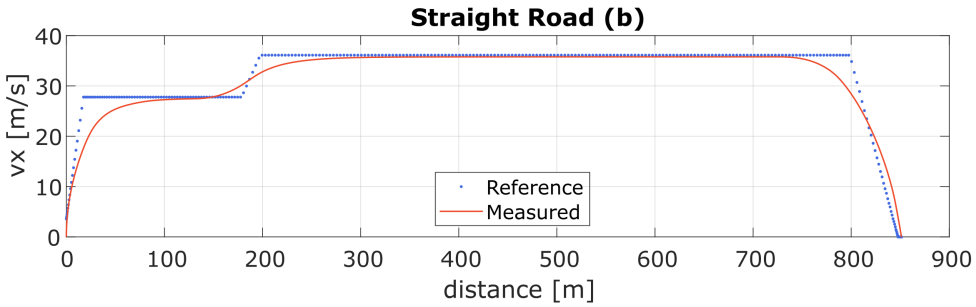

Figure 5.7: Vehicle velocity and reference velocity during Straight driving maneuver.

5.4 Integral action on the the longitudinal velocity

The integral action introduced to the LTV-MPC to improve velocity tracking is discussed below, and Figure 5.8 depicts the system's new structure.

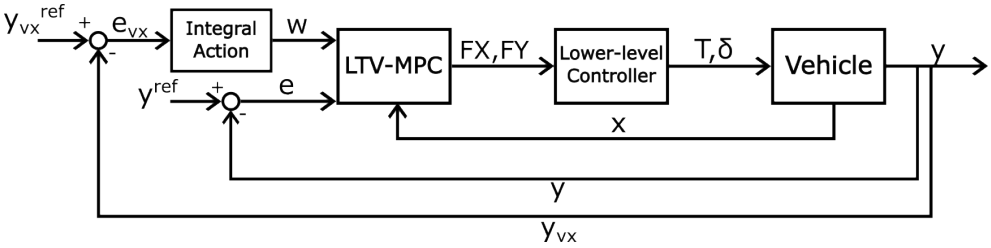

Figure 5.8: System structure with the integral action to the LTV-MPC.

From the system in Equation B.9, the new system is enlarged with an additional state w representing the integral of the velocity error e_{vx}, and the state equations are:

$$
\begin{cases} x(k+i+1) = A_{k+i}x(k+i) + B_{k+i}u(k+i) + G_{k+i} \\ w(k+i+1) = w(k+i) + K\ e_{vx}(k+i+1) \\ e_{vx}(k+i+1) = y_{vx}^{ref} - y_{vx}(k+i) \end{cases}
$$

$$
\begin{cases} x(k+i+1) = A_{k+i}x(k+i) + B_{k+i}u(k+i) + G_{k+i} \\ w(k+i+1) = w(k+i) + K\ (y_{vx}^{ref}(k+i+1) - \\ \qquad\qquad -C_v A_{k+i}x(k+i) - C_v B_{k+i}u(k+i) - C_v G_{k+i}) \end{cases} \tag{5.7}
$$

$$
\begin{aligned} &where\ \ i = 0,\ \dots, N-1 \\ &\qquad C_v = \begin{bmatrix} 0 & 0 & 0 & 1 & 0 & 0 \end{bmatrix} \end{aligned}
$$

K is a tuning parameter for the integral action set to 0.25 and the state x is as in Equation 3.1.

The enlarged system, in the equivalent form of Eq. B.9, that is directly implementable into code is:

$$
\begin{aligned} \begin{bmatrix} x(k+i+1) \\ w(k+i+1) \end{bmatrix} &= \begin{bmatrix} A_{k+i} & 0 \\ -KC_v A_{k+i} & I \end{bmatrix} \begin{bmatrix} x(k+i) \\ w(k+i) \end{bmatrix} + \\ &+ \begin{bmatrix} B_{k+i} \\ -KC_v B_{k+i} \end{bmatrix} u(k+i) + \begin{bmatrix} I & 0 \\ -KC_v & K \end{bmatrix} \begin{bmatrix} G_{k+i} \\ y_{vx}^{ref}(k+i+1) \end{bmatrix} \\ y(k+i) &= \begin{bmatrix} C_{k+i} & 0 \\ 0 & I \end{bmatrix} \begin{bmatrix} x(k+i) \\ w(k+i) \end{bmatrix} \end{aligned} \tag{5.8}
$$

The C matrix is as defined in Equation 3.4, and the state w, as additional output, is required to be minimized to zero in the LTV-MPC cost function, and the reference vector from Equation 5.10 becomes:

$$
r^i = \begin{bmatrix} -x_r^i \sin\theta_r^i + y_r^i \cos\theta_r^i \\ \theta_r^i \\ v_{xr}^i \\ 0 \end{bmatrix} \tag{5.9}
$$

A basic anti-wind-up solution is also employed. The integral error is decreased to small values when the velocity error (reference minus measured velocity) changes sign. The integral error is not zeroed in order to prevent heavy reductions in the control action. It was important to consider an anti-

wind-up solution to reduce overshoots in the vehicle's velocity and the risk of the car exceeding the speed limit.
Besides, the integral control action improves the car's capacity to follow the reference velocity; however, it also aggravates the problem of yaw angle tracking during hard braking, as reported in Section 5.3. The MPC tries to reduce the longitudinal velocity by turning the car and crabbing laterally during braking. A simple and effective solution to this problem is to set a reference to the lateral vehicle velocity equal to zero when the car faces heavy brakes. As a result, the new output, the C matrix, and reference of the system in Equation 5.8 and 5.9 becomes:

$$y(k+i) = \begin{bmatrix} C_{k+i} & 0 \\ 0 & I \end{bmatrix} \begin{bmatrix} x(k+i) \\ w(k+i) \end{bmatrix}$$

$$r^i = \begin{bmatrix} -x_r^i \sin\theta_r^i + y_r^i \cos\theta_r^i \\ \theta_r^i \\ v_{xr}^i \\ 0 \\ 0 \end{bmatrix} \tag{5.10}$$

$$with \quad C_i = \begin{bmatrix} -\sin\theta_r^i & \cos\theta_r^i & 0 & 0 & 0 & 0 \\ 0 & 0 & 1 & 0 & 0 & 0 \\ 0 & 0 & 0 & 1 & 0 & 0 \\ 0 & 0 & 0 & 0 & 1 & 0 \end{bmatrix}$$

The performances of this solution are reported in Table 5.6 and are obtained in the same way as Table 5.5.

Steady-state speed with Integral Action			
MPC parameters	**Straight driving**	**Yaw Max during braking**	**Cornering**
Th=2.0s, Ts=0.20s, N=10	130 km/h	0.021 rad	50.00 km/h
Th=1.5s, Ts=0.15s, N=10	130 km/h	0.041 rad	49.99 km/h
Th=1.0s, Ts=0.10s, N=10	130 km/h	0.117 rad	50.02 km/h
Th=1.4s, Ts=0.20s, N= 7	130 km/h	0.036 rad	49.87 km/h
Th=1.5s, Ts=0.30s, N= 5	130 km/h	0.043 rad	49.32 km/h
Th=1.0s, Ts=0.20s, N= 5	129.97 km/h	0.046 rad	49.64 km/h

Table 5.6: Steady-state velocity of the vehicle during straight driving and cornering when an integral action is applied. During straight driving the reference velocity is 130 km/h, during cornering is 50 km/h. The Yaw Max value is the maximum yaw angle that the vehicle has during hard braking from 130 km/h to 0 km/h.

A comparison with Table 5.5 shows significant improvements in velocity tracking. During straight driving, the vehicle achieves a steady-state speed of 130 km/h for all controllers. Regarding cornering, the same improvements are obtained. At the beginning of the turn, the vehicle's speed drops around 48 km/h for all the controllers despite the constant reference at 50 km/h, and the integral action successfully takes the car at the desired speed within a short distance.
In addition, the null lateral velocity reference during hard braking keeps the yaw angle limited, especially with the integral action that provides additional control efforts for velocity tracking also during braking.

Chapter 6

Energy minimization control strategy

This Chapter introduces the control strategy that exploits Over-Actuation redundancy (4WD, 4WS) for energy minimization and includes it in the solution presented in Chapter 5. From Section 3.3, two principal sources of energy consumption are derived: due to the wheel slip (longitudinal σ_x and lateral α) and due to the engine power losses.
This strategy minimizes these two components by introducing an additional allocation step, and the solution is presented in Section 6.1. Section 6.2 presents the results on energy minimization obtained in simulation.

6.1 Control strategy

Regarding slip power losses, they depend on the wheel slip squared values, as in Equations 3.16 and 3.22. It is clear that the minimum value of the power losses due to cornering resistance and longitudinal sliding of the contact patch is minimized when the slips at the wheels are similar for all four wheels. This result can be obtained from the solution of the following optimization problems.

$$\begin{aligned} &\min_{\alpha_i} \sum_{i=1}^{4} C_\alpha F_{z,i} v_x \alpha_i^2 \\ &s.t. \qquad \sum_{i=1}^{4} -C_\alpha F_{z,i} \alpha_i = F_y^{des} \end{aligned} \tag{6.1}$$

$$\begin{aligned} &\min_{\alpha_{x,i}} \sum_{i=1}^{4} C_\sigma F_{z,i} r \omega_i \sigma_{x,i}^2 \\ &s.t. \qquad \sum_{i=1}^{4} C_\sigma F_{z,i} \sigma_{x,i} = F_x^{des} \end{aligned} \tag{6.2}$$

To create this condition, the requested forces (FX_i, FY_i) at the wheels (Figure 5.5a) must be proportional to the normal ones ($F_{z,i}$). In [38], shifting the torque request to the outer wheels reduces cornering resistance because the outer wheels stand the higher normal forces.
To achieve this result, the weighting term R_0 of the quadratic cost function (Eq. 5.4) should have its terms inversely proportional to the normal forces ($F_{z,i}$) on the wheels, as follows:

$$\begin{aligned} R_0 = diag(&\frac{1}{F_{z,FL}}, \frac{1}{F_{z,FR}}, \frac{1}{F_{z,RR}}, \frac{1}{F_{z,RL}}, \frac{1}{F_{z,FL}}, \frac{1}{F_{z,FR}}, \frac{1}{F_{z,RR}}, \frac{1}{F_{z,RL}}, \dots \\ &\dots, N\ times) \end{aligned} \tag{6.3}$$

In addition, this solution, allocating the forces proportionally to $F_{z,i}$, allows for exploiting better tire availability maximizing the distance of the wheel's forces (FX_i, FY_i) to the friction circle limit. The result is less wheel saturation and higher wheel stability.
The results on energy reduction are reported in Section 6.2.

Concerning the power losses due to the engine efficiency, the ideal solution is to model and include them inside the LTV-MPC cost function. In this way, the MPC solution minimizes the energy consumed along the horizon. The goal is to allocate the torques at the wheels such that the overall vehicle torque remains unchanged and the engine efficiencies, dependent on the operating condition (T, ω), are maximized. However, the nonlinear efficiency characteristic of the engines must be linearized to be included in the cost function, with consequent loss of information. The MPC's solution does not find convenient points of the engine characteristic but reduces the energy lost along the prediction horizon by minimizing the torques and the speeds of all the engines. The consequence is a reduction in the vehicle velocity and a worse pursuit of the reference. Therefore, an additional allocation step is required to incorporate the engine's nonlinear efficiency characteristic into the controller

(Figure 6.1). This step redistributes the FX forces provided by the LTV-MPC between the front and rear axles of the vehicle based on the nonlinear efficiency characteristic. The two sides are independent to preserve the yaw moment provided by the longitudinal forces, and the friction circle constraint is still satisfied.
This allocation step is explained below.

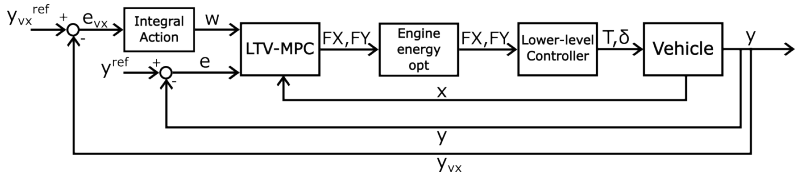

Figure 6.1: System structure with the engine energy optimization step.

The LTV-MPC provides FX and FY forces for each wheel, and the normal ones ($F_{z,i}$) are estimated as in [82]. From these, the reallocation of the FX forces is bounded by the friction circle, as follows:

$$\begin{aligned} FX_{i,max} &= \sqrt{\mu\, F_{z,i}^2 \;-\; FY_i^2} \\ i &= FL, FR, RR, RL \end{aligned} \tag{6.4}$$

This technique is only activated if the sum of the two FX forces per side is positive; otherwise, this phase is skipped because braking does not require engine power.
Now, considering one side, the k value is defined as the distributed ratio of the desired FX_{des} force with respect to the front wheel. $k = 0$ if the desired total FX_{des} (per side) is applied only on the rear wheel, and $k = 1$ if applied only on the front wheel. The k value is bounded by the constraint in Equation 6.5, as follows:

$$\begin{aligned} k_i &= (\max(1 - \frac{FX_{max,rear,i}}{FX_{des,i}},\ 0)\ ,\ \min(\frac{FX_{max,front,i}}{FX_{des,i}}, 1)) \\ i &= left, right \end{aligned} \tag{6.5}$$

Optimizing the power consumed by the engine as a function of the k parameter, the optimal k^{opt} value is derived, and the new allocation on the

front and rear wheels is as follows:

$$\begin{aligned} FX_{front,i} &= k_i^{opt}\ FX_{des,i} \\ FX_{rear,i} &= (1 - k_i^{opt})\ FX_{des,i} \\ i &= left, right \end{aligned} \tag{6.6}$$

The optimization of the power consumed by the engine is obtained by minimizing the used electric power ($T\omega/\eta$), which assumes that the FX forces are directly linked to the torque as $FX = T/r_w$. This assumption is valid for small steering angles δ. However, thanks to the four steering wheels, the vehicle can turn by limiting the steering angles to small values(<0.1 rad). Hence, this approximation can stand and the electric power is approximated to $FX \cdot VX/\eta$.
The wheels' velocity is known and can be assumed constant within a control step of 0.1 s. The electric power consumed by one side of the car depends only on the forces $FX_{front,i}$ and $FX_{rear,i}$ of that side, which are constrained by the desired force $FX_{des,i}$. Therefore, the nonlinear-optimization deals with only one variable (k) and does not affect the real-time performance of the vehicle. This solution has a side effect that does not consider the previous allocation step of the FX forces, increasing the energy lost by the longitudinal slip of the tires. However, as analyzed in Section 3.3.1, the energy lost due to engine efficiency is significantly greater than that wasted due to sliding of the wheels' contact point, so preferring the former brings better results in terms of energy consumption. In addition, this solution keeps the distribution of lateral forces of the wheels unchanged, keeping the same attention to the energy lost due to cornering resistance.
Results on the advantage of this solution in terms of energy minimization are reported in section 6.2.

6.2 Results on energy minimization

This section presents the results obtained from this solution regarding energy minimization. In particular, it is relevant to distinguish between the contribution generated by the vehicle's weight distribution on the wheels and the strategy investigated to reduce the power lost in the engines. The two solutions act on vehicle losses from different perspectives. The first reduces the losses produced by the tires due to cornering and slipping, and the second

reallocates the forces to maximize the overall efficiency of the four engines. Simulation results are produced by investigating five different maneuvers:

a) The vehicle travels a mixed-profile road long 560 m where straight and corner sectors are combined, as shown in Figure 3.6a. It should follow a reference speed set at 90 km/h for straight sectors and 40 km/h for curved sectors. The reference path starts on the right lane and, after 20 m, slides to the left, with the reference yaw angle pointing forward, to reach the road's centerline to mimic a partial lane-change maneuver. Then, it continues on the road's centerline to allow a visual assessment of the trajectory-tracking performance in addition to numerical values. Before the vehicle reaches the end of the track, the reference speed drops from 90 km/h to 0 km/h in 30 m.

b) The vehicle follows a straight trajectory where the reference speed changes from 0 m/h to 100 km/h in 100 m. As soon as the car reaches the desired speed of 100 km/h, the maneuver ends.

c) The vehicle follows a straight trajectory where the reference speed changes from 0 m/h to 100 km/h in 40 m. As soon as the car reaches the desired speed of 100 km/h, the maneuver ends.

d) The vehicle follows a straight trajectory where the reference speed changes from 0 km/h to 100 km/h in 15 m. As soon as the car reaches the desired speed of 100 km/h, the maneuver ends.

e) The vehicle follows a 30m-radius right-curved trajectory where the required speed is 50 km/h. The maneuver investigated is for steady-state cornering long 80 m.

At the end of these maneuvers, five power source measurements were obtained.

1. The electric power requested by the engines.
2. The power lost in the motors, computed using the engine efficiency characteristic.
3. The mechanical power at the shaft of the four engines.
4. The power lost due to wheel slipping, computed according to Equation 3.15, only for positive longitudinal forces at the wheels F_x since braking is not considered.

5. The power lost due to wheel cornering, computed according to Equation 3.17.

For each of the five terms, the energy was computed as the time integral of the power during the maneuvers. The different MPC configurations, analyzed in Section 5.3, are investigated from the energetic perspective by varying the prediction horizon parameters: prediction horizon (Th), prediction sampling time (Ts), and the number of samples (N). However, only the case (Th=1.5 s, Ts=0.15 s, N=10) is reported in Table 6.1 for brevity, whereas the entire set of simulations is provided in Appendix C.
The tests are performed to compare the cases when no energy minimization strategy is implemented (B), when only the vehicle's weight distribution on the wheels is considered (W), and when, in addition to weight distribution, also the engine efficiency optimization strategy is included (E).

The main objective of this research is to minimize the electric energy provided to the engines from the batteries. Table 6.1 shows that the two solutions investigated (W and E) can successfully contribute to the goal by reducing multiple energy losses. However, further considerations are required. The vehicle weight distribution impacts mainly, as expected, on the losses at the wheels (longitudinal and lateral sliding) in all the maneuvers, reducing, consequently, the mechanical energy at the motor shaft.
The losses caused by longitudinal slip increase with vehicle acceleration, as it can be observed by comparing maneuvers c) and d). In addition, when the car acceleration is higher, case d), the weight distribution has more impact on the slip losses. The average reduction of energy losses due to longitudinal slip among all the MPC variations investigated is 8% for maneuver c) and 11% for maneuver d). Whereas, regarding maneuver a), where the vehicle accelerates several times and has short traits to reach the desired velocity, the improvements are even better; among all the MPC set-ups, the energy losses due to longitudinal slip are reduced by 36%.
The objective of the vehicle weight distribution, as explained in Section 6.1, is to produce an equal longitudinal slip ratio (σ_x) at the four wheels, and this achievement is the reason for energy minimization, as in Equations 6.2. Figure 6.2 shows the slip ratio at the wheels during maneuver d), before and after considering vehicle weight distribution.

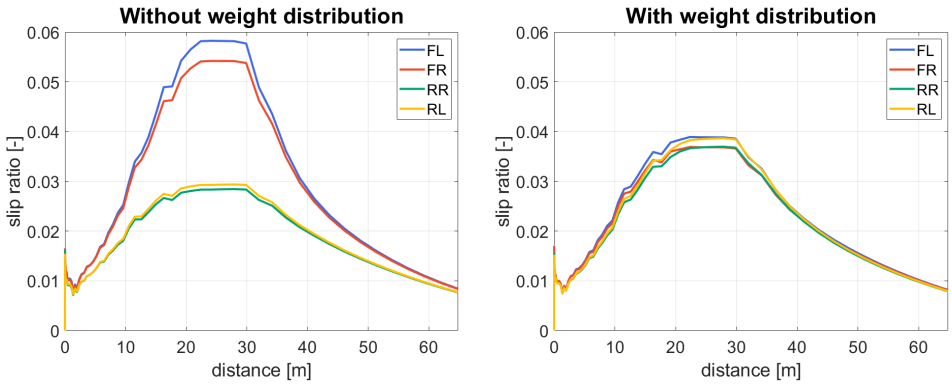

(a) (b)

Figure 6.2: Comparison of the tire longitudinal slip ratio during maneuver d) when the vehicle weight distribution is considered b) and when it is not a).

During steady-state conditions, the longitudinal slip is almost null, and the losses are irrelevant, as it can be observed during steady-state cornering e). In addition, the torque distribution, proportional to the wheel's vertical forces, is not optimized for the energy wasted in the engines, as a result, during straight driving, this component partially compensates for the energy saved due to slip losses and results in an almost null advantage in the electric energy consumed. For cornering resistance losses, similar results are obtained. In all cases, the vehicle weight distribution helps to reduce the energy wasted by lateral sliding. During steady-state cornering, maneuver e), the average energy loss reduction, due to this term, is around 29%. Besides, the wheel sideslip angles (α) have similar values, Figure 6.3, to fulfill the solution of Equation 6.1.

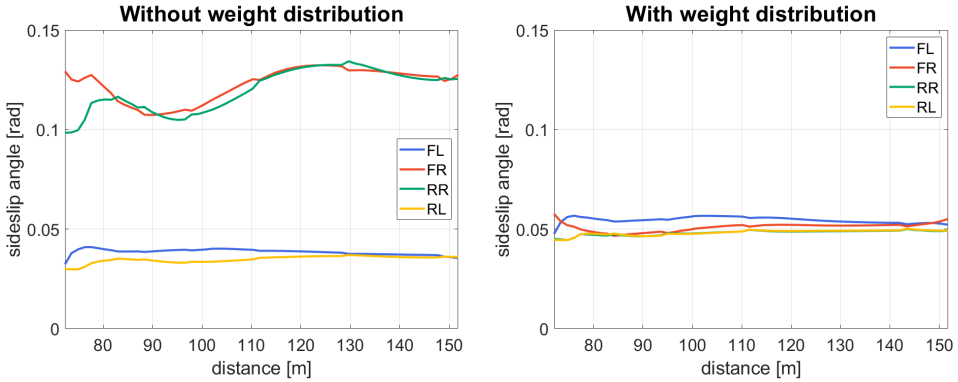

(a) (b)

Figure 6.3: Comparison of the tire sideslip angles during maneuver e) when the vehicle weight distribution is considered b) and when it is not a).

Regarding the second step for energy minimization, which considers the losses due to motor efficiency, the results assert further improvements. In particular, they are more evident when the overall longitudinal force is not sufficiently high to employ all four wheels to generate it. In this case, the optimization step allocates the torques only on the rear wheels. The reason lies in the shape of the engine efficiency characteristic, which has higher values at higher torques (see Appendix A). Therefore, using only two engines rather than four allows for exploiting more efficient working points at the same overall torque. As a result, the greatest benefits, between the several maneuvers, occur during low accelerations, maneuver b), and steady-state cornering, maneuver e), when the torque necessary to keep the vehicle speed is not high and can be distributed only on two wheels. This method, however, is less efficient during rapid acceleration, when all four wheels must produce the thrust and no room for reallocation is allowed.
During maneuvers b) and e), the reduction of the energy wasted in the engines is 23% and 37%, respectively, which corresponds to an overall electric energy reduction of 2% and 13%.

In the end, this strategy presents a drawback. Allocating the torques only on two wheels, rather than four, increases the slip ratio of these and, consequently, the longitudinal slip losses. This phenomenon is visible in all the maneuvers investigated, although the reduction of the engine power losses overcomes the increased losses due to longitudinal slip, which results in lower electric energy consumption.
Despite this, energy consumption does not represent the only cost of a vehicle, both from an economic and resource perspective. Tire wearing represents another factor, and increasing the slip ratio might affect this aspect with more problems than benefits from energy saving. Moving beyond the scope of this project, additional research may be needed to determine the limits of this approach from this point of view.

Maneuver a)					
Case	**Elect. En**	**Eng. Loss**	**Mech. En**	**Slip loss**	**Cor. Res.**
B	2580.7 kJ	393.9 kJ	2186.8 kJ	104.86 kJ	72.79 kJ
W	2542.0 kJ	390.3 kJ	2151.7 kJ	58.00 kJ	67.59 kJ
E	2502.7 kJ	349.7 kJ	2153.0 kJ	68.68 kJ	68.36 kJ
Maneuver b)					
Case	**Elect. En**	**Eng. Loss**	**Mech. En**	**Slip loss**	**Cor. Res.**
B	1075.4 kJ	163.7 kJ	911.7 kJ	12.03 kJ	0.00 kJ
W	1075.1 kJ	163.5 kJ	911.6 kJ	11.91 kJ	0.00 kJ
E	1052.6 kJ	126.0 kJ	926.6 kJ	28.29 kJ	0.00 kJ
Maneuver c)					
Case	**Elect. En**	**Eng. Loss**	**Mech. En**	**Slip loss**	**Cor. Res.**
B	1030.5 kJ	122.2 kJ	908.3 kJ	27.34 kJ	0.00 kJ
W	1028.8 kJ	122.5 kJ	906.3 kJ	25.09 kJ	0.00 kJ
E	1025.1 kJ	114.8 kJ	910.3 kJ	29.27 kJ	0.00 kJ
Maneuver d)					
Case	**Elect. En**	**Eng. Loss**	**Mech. En**	**Slip loss**	**Cor. Res.**
B	1029.6 kJ	116.2 kJ	913.4 kJ	36.28 kJ	0.01 kJ
W	1028.8 kJ	118.5 kJ	910.3 kJ	32.27 kJ	0.01 kJ
E	1028.7 kJ	115.9 kJ	912.8 kJ	35.14 kJ	0.01 kJ
Maneuver e)					
Case	**Elect. En**	**Eng. Loss**	**Mech. En**	**Slip loss**	**Cor. Res.**
B	197.5 kJ	72.9 kJ	124.6 kJ	0.70 kJ	79.28 kJ
W	154.0 kJ	55.5 kJ	98.6 kJ	0.16 kJ	54.90 kJ
E	134.7 kJ	35.3 kJ	99.4 kJ	0.45 kJ	55.60 kJ

Table 6.1: Energy consumed by the LTV-MPC with parameters (Th=1.5 s, Ts=0.15 s, N=10) during the different Maneuvers a)-e). Three cases are reported: B) the base version with no energy minimization implementation, W) when only the vehicle's weight distribution is considered, E) when also the engine efficiency optimization is included.

Chapter 7

Implementation on the RCV

This Chapter examines the implementation of the controller on the RCV-E. In particular, Section 7.1 talks about the problem faced to embed the controller on dSPACE - MicroAutoBox II, whereas Section 7.2 tests the controller's performance and limits on the platform from a real-time point of view.

7.1 Implementation of the LTV-MPC in dSPACE

To integrate the controller into the dSPACE platform, a Simulink model containing the vehicle architecture is provided with dSPACE. Here, the communication between sensors, actuators, and vehicle control is managed. Therefore, to integrate the controller in dSPACE, the simplest procedure is to write it in Simulink and integrate it in the pre-existing dSPACE-Simulink environment. The Simulink environment must be built into C-code before it can be uploaded to MicroAutoBox II and run on the vehicle.
However, the Matlab version implemented on the RCV-E is the 2016b and does not support the built-in optimization functions, like quadprog [83], for standalone code generation. As a result, a third-party optimization solver is necessary. In addition, to integrate a third-party software in the Simulink environment and build it into C-code, the solver must be provided with its source code which must be added to the Simulink environment and compiled in C-code along with the entire environment using Simulink Coder, like DAQP [80, 81]. An alternative is for an already tested procedure to be provided along with the solver to cross-compile the software libraries with dSPACE so that the optimization problem can be formulated and linked to the software, like acados [84, 85].
The software utilized to solve the quadratic problem of the LTV-MPC is DAQP,

which provides both the source code and an S-function, written in C-code, that can be integrated into the Simulink environment and built along with it.
The S-function requires as input the matrices (H, f, A, ub, lb) to solve the following quadratic problem.

$$\begin{aligned} &\min_{x} \frac{1}{2} x^T H x + f^T x \\ &s.t. \quad lb < A\, x < ub \end{aligned} \tag{7.1}$$

Besides, the S-function is provided in the 2021a Matlab version and must be downgraded to the 2016b version. The structure of the S-function includes an Initialization and Termination step where the variables are allocated and deallocated. Automatically downgrading it to the 2016b version would include these two steps in the Output function, which is called at each iteration step. This result reduces the computation time needed to execute the solver at each iteration, because beyond providing the optimal output, it must also allocate and deallocate the variables. To solve this issue, the S-function must be reformulated using the legacy code tool [86]. In such a way, the Initialize and Terminate functions in the original S-function are kept unchanged and not automatically included in the Output function.

Next, the engine's efficiency optimization step, described in Section 6.1, exploits a nonlinear optimization problem to find the solution. However, it is a nonlinear optimization on one optimization variable, so to include the nonlinear problem in dSPACE, it was easier and more straightforward to rewrite it in vector form. The k value, defined as the distributed ratio of the desired FX_{des} force with respect to the front wheel per each side, is discretized within its boundaries (defined in Equation 6.5) with a step of 0.01 and consequently, the electric power $FX \cdot VX/\eta$ is discretized and written in the vectorial form. To obtain the optimal value is sufficient to find the minimum value of the array and then find the corresponding optimal distributed ratio k^{opt}.

This approach used to embed the controller on the RCV-E, is also used in simulation to obtain the results presented in Section 6.2.

7.2 Real-time performance of the controller

The real-time performance of the controller on the RCV-E is evaluated without driving the vehicle. The controller receives a fictitious state of the vehicle, and while running on MicroAutoBox II, it must provide the expected control action, without it being connected to the actuation.
The real-time performance is affected only by the prediction horizon (N) chosen for the LTV-MPC. It affects both the time to generate the matrices (H, f, A, ub, lb) for the quadratic problem and the time to solve the optimization problem.
Multiple prediction horizons of the LTV-MPC have been tested to assess the limits of the solution. The execution time of the controller is measured by logging from the dSPACE interface the execution time of the controller Task. Results are reported in Table 7.1.

Prediction Horizon N	**Execution time**
N = 5	0.005 s
N = 7	0.014 s
N = 10	0.033 s
N = 12	0.086 s
N = 13	0.113 s
N = 15	0.129 s

Table 7.1: Execution time of the controller on dSPACE - MicroAutoBox II.

Results in Table 7.1 show that the controller does not suffer from execution problems in real-time. In particular, the control sample time used in the simulations for the LTV-MPC is 0.1 s, which would limit the prediction horizon of the controller to 12 samples. This value is sufficiently high to guarantee excellent performance of trajectory following and energy minimization in simulation. As presented in Chapters 5 and 6, the tests on the controller performance were obtained with a maximum of 10 prediction samples, which means that the implementation in MicroAutoBox II does not limit the controller during its real-time functioning.
In conclusion, methods requiring higher computational efforts might be examined in future studies to optimize the RCV-E execution availability. Nonetheless, the control strategy investigated in this study is relatively conservative in terms of the vehicle's computational efforts, and as a result, it may be suitable for even more computationally limited platforms.

Chapter 8

Conclusions and Future works

This chapter draws conclusions on the results obtained from this research project. In particular, Section 8.1 describes the achievements obtained to answer the research question in Chapter 1, and Section 8.2 proposes alternative ways to investigate the problem and build upon this research study.

8.1 Conclusions

In this project, a control strategy that exploits the redundancy of the vehicle's Over-Actuation (4WD, 4WS) to minimize energy consumption in addition to autonomous trajectory-following is presented.
The investigated control strategy is evaluated considering the trajectory-following performance, the energy reduction results, and its ability to run in real-time on an embedded platform.

8.1.1 Trajectory-following

The control strategy for trajectory-following employs an LTV-MPC, and to assess its performance, multiple time horizons are compared. Results show that a higher number of predicted samples (N=10) along with a short prediction step (Ts=0.1 s) have the best results in reducing the lateral deviation from the desired path and tracking the reference yaw angle. However, during heavy braking, this prediction horizon combination suffers more from tracking the desired yaw angle, and a higher prediction horizon helps to improve it. This problem affects, in different ways, all the considered prediction horizons and is reduced by setting a reference on the lateral velocity during hard braking.
An integral action is also considered to null the effect of unmodeled forces,

such as aerodynamic and wheel rolling loss, and guarantee a perfect tracking of the longitudinal velocity at steady-state conditions.

8.1.2 Energy minimization

From an initial analysis of the sources of energy consumption that can be affected by the over-actuation considered within this project, two terms are identified: the energy wasted by the tires due to longitudinal and lateral sliding and the energy wasted in the motors. Different control techniques are integrated into the control strategy to minimize these sources of energy loss: the first considers the vehicle weight distribution to allocate the forces at the wheels, and the second reallocates the longitudinal forces optimizing the engine efficiency characteristic. Regarding the first control technique, it allocates the longitudinal and lateral forces at the wheels proportionally to the vertical ones to reduce the energy consumed by the tires due to sliding and improve vehicle stability by ensuring a higher safety margin while generating the forces. As expected, this control strategy affects more maneuvers where the wheels' sideslip angle and slip ratio are higher, so during cornering and longitudinal acceleration. Results show that during high acceleration the reduction of the energy wasted due to longitudinal slip reaches 11%; nevertheless, the torque distribution, proportional to the wheel's vertical forces, is not optimized for the energy wasted in the engines, which results in a null advantage in the electric energy consumed. During steady-state cornering at a constant speed, the reduction of the energy wasted due to lateral sliding is 29% for the case investigated, and since the engine torque is less affected, this reduction impacts more on the electric energy provided to the engines, which decreases by 19%. Concerning the second control technique, results show that when the total requested torque is sufficiently low, the reallocation step is better exploited, and the overall torque is delivered only by the rear wheels that work at more efficient engine conditions. In this regard, this technique affects more low accelerations and steady-state cornering, reducing the overall electric energy by 2% during straight acceleration and by 13% during steady-state cornering. However, along with the electric energy reduction, this technique presents a drawback. When allocating the forces only on two wheels rather than four, the tire's longitudinal slip increases with the consequence of an increase in the energy consumed by it. Results show a higher reduction of the energy lost in the engines compared to the one increased due to higher longitudinal slips. Nonetheless, other problems, such as tire wearing, may be affected, with a possible increase in costs and resources used.

8.1.3 Real-time performance

The controller presents excellent performance on MicroAutoBox II regarding real-time performance. Tests were conducted with the vehicle still, without connecting the controller's output to the actuation. A fictitious state of the vehicle was provided to the controller to test its correct functioning.
Results show that the critical factor is the number of samples (N) along the prediction horizon, which increase the computational time required to find the control action. Nevertheless, with a control sample time of 0.1 s, the maximum number of samples to prevent overrun error is N=12, which is a high value for the trajectory tracking performance in simulation.

8.2 Future works

The results obtained from the controller implementation on the RCV-E show margins to exploit and develop a more computationally expensive control action. Research may be oriented to study additional solutions that solve the autonomous driving problem and exploit the actuation redundancy to achieve better performance in energy saving and trajectory following while sacrificing computational efficiency.
The model's complexity can be increased by including more DoF, such as roll and pitch angles, which can be exploited for a better estimation of the vehicle weight distribution on the wheels.
Regenerative braking may also be investigated. In particular, a further step may be to investigate the optimal braking torques at the wheels that provide the highest energy recovery in the four engines and compare them to the stability and braking performance. The next step after this research project is to evaluate the performance of the controller regarding trajectory following and energy minimization directly on the RCV-E to confirm the results obtained in the simulation and face the problem of a real application.

References

[1] A. Gasparetto, P. Boscariol, A. Lanzutti, and R. Vidoni, *Path Planning and Trajectory Planning Algorithms: A General Overview*. Cham: Springer International Publishing, 2015, pp. 3–27. ISBN 978-3-319-14705-5. [Online]. Available: https://doi.org/10.1007/978-3-319-14705-5_1 [Page 1.]

[2] G. Liu, H. Ren, S. Chen, and W. Wang, "The 3-dof bicycle model with the simplified piecewise linear tire model," in *Proceedings 2013 International Conference on Mechatronic Sciences, Electric Engineering and Computer (MEC)*, 2013. doi: 10.1109/MEC.2013.6885617 pp. 3530–3534. [Pages 3 and 39.]

[3] T. Liu, L. N. Jia, N. Yang, and C. S. Li, "Research on the handling stability of four-wheel steering vehicle," *Journal of Physics: Conference Series*, vol. 1213, no. 5, p. 052039, jun 2019. doi: 10.1088/1742-6596/1213/5/052039. [Online]. Available: https://dx.doi.org/10.1088/1742-6596/1213/5/052039 [Pages 3 and 37.]

[4] N. Hamzah, M. K. Aripin, Y. M. Sam, H. Selamat, and M. F. Ismail, "Yaw stability improvement for four-wheel active steering vehicle using sliding mode control," in *2012 IEEE 8th International Colloquium on Signal Processing and its Applications*, 2012. doi: 10.1109/CSPA.2012.6194704 pp. 127–132. [Pages 3 and 37.]

[5] KTH-ITRL. RCV-E - Research Concept Vehicle model E. [Online]. Available: https://www.itrl.kth.se/research/completed-projects/research-concept-vehicle-model-e-1.917925 [Pages 4, 6, 8, and 39.]

[6] dSPACE, "MicroAutoBox II." [Online]. Available: https://www.dspace.com/en/inc/home/products/hw/micautob/microautobox2.cfm [Pages 4, 6, and 10.]

[7] European Union. (2022) Infographic - fit for 55: why the eu is toughening co2 emission standards for cars and vans. Last reviewed: 12 Dec 2022, accessed: 8 Feb 2023. [Online]. Available: https://www.consilium.europa.eu/en/infographics/fit-for-55-emissions-cars-and-vans/ [Pages 5 and 7.]

[8] P. Sun, "Improving energy-efficiency of electric vehicles by over-actuation," Ph.D. dissertation, Royal Institute of Technology (KTH), Stockholm, Sweden, 2020. [Pages 7 and 13.]

[9] J. Edrén, "Motion modelling and control strategies of over-actuated vehicles," Ph.D. dissertation, Royal Institute of Technology (KTH), Stockholm, Sweden, 2014. [Pages 7, 13, and 39.]

[10] A. Håkansson, "Portal of research methods and methodologies for research projects and degree projects," in *Proceedings of the International Conference on Frontiers in Education: Computer Science and Computer Engineering, FECS'13*. CSREA Press U.S.A., Jul. 2013. ISBN 1-60132-243-7 pp. 67–73. [Pages 8 and 9.]

[11] R. Baggi, E. Franco, and A. Serrani, *Dynamic Control Allocation for a Class of Over-actuated Aircraft*, 2020. [Online]. Available: https://arc.aiaa.org/doi/abs/10.2514/6.2020-0841 [Page 11.]

[12] K. F. Prochazka, H. Eduardo, and S. R. Klein, "Integrated fault-tolerant control of an over-actuated aircraft using optimal control allocation and robust sliding mode observers," in *2018 IEEE Conference on Control Technology and Applications (CCTA)*, 2018. doi: 10.1109/CCTA.2018.8511538 pp. 171–178. [Page 11.]

[13] M. W. Oppenheimer, D. B. Doman, and M. A. Bolender, "Control allocation for over-actuated systems," in *2006 14th Mediterranean Conference on Control and Automation*, 2006. doi: 10.1109/MED.2006.328750 pp. 1–6. [Pages 11 and 12.]

[14] T. A. Johansen and T. I. Fossen, "Control allocation—a survey," *Automatica*, vol. 49, no. 5, pp. 1087–1103, 2013. doi: https://doi.org/10.1016/j.automatica.2013.01.035. [Online]. Available: https://www.sciencedirect.com/science/article/pii/S0005109813000368 [Pages 12 and 13.]

[15] D. Doman and M. Oppenheimer, *Improving Control Allocation Accuracy for Nonlinear Aircraft Dynamics*, 2002. [Online]. Available: https://arc.aiaa.org/doi/abs/10.2514/6.2002-4667 [Page 13.]

[16] P. Sun, A. Trigell, L. Drugge, and J. Jerrelind, "Energy efficiency and stability of electric vehicles utilising direct yaw moment control," *Vehicle System Dynamics*, vol. 60, pp. 1–21, 11 2020. doi: 10.1080/00423114.2020.1841903 [Page 13.]

[17] P. Sun, A. Stensson Trigell, L. Drugge, and J. Jerrelind, "Energy-efficient direct yaw moment control for in-wheel motor electric vehicles utilising motor efficiency maps," *Energies*, vol. 13, no. 3, 2020. doi: 10.3390/en13030593. [Online]. Available: https://www.mdpi.com/1996-1073/13/3/593 [Page 13.]

[18] J. Edrén, M. Jonasson, J. Jerrelind, A. Stensson Trigell, and L. Drugge, "Energy efficient cornering using over-actuation," *Mechatronics*, vol. 59, pp. 69–81, 2019. doi: https://doi.org/10.1016/j.mechatronics.2019.02.006. [Online]. Available: https://www.sciencedirect.com/science/article/pii/S0957415819300182 [Pages 14, 16, 31, and 41.]

[19] J. Edrén, "Exploring force allocation control of over actuated vehicles," Licentiate Thesis, Royal Institute of Technology (KTH), Stockholm, Sweden, 2011. [Page 14.]

[20] S. Bhat, "An investigation into the optimal control methods in over-actuated vehicles: With focus on energy loss in electric vehicles," p. 76, 2016. [Page 14.]

[21] MathWorks. (2022) Model predictive control toolbox. Accessed: 8 Feb 2023. [Online]. Available: https://se.mathworks.com/help/mpc/index.html [Page 14.]

[22] KTH-ITRL. RCV - Research Concept Vehicle. Last changed: Jan 07, 2021. [Online]. Available: https://www.itrl.kth.se/about-us/labs/rcv-1.476469 [Page 14.]

[23] M. M. Davari, "Exploiting over-actuation to reduce tyre energy losses in vehicle manoeuvres," Ph.D. dissertation, Royal Institute of Technology (KTH), Stockholm, Sweden, 2017. [Page 14.]

[24] M. Davari, J. Jerrelind, A. Trigell, and L. Drugge, "Extended brush tyre model to study rolling loss in vehicle dynamics simulations," *International Journal of Vehicle Design*, vol. 73, p. 255, 01 2017. doi: 10.1504/IJVD.2017.083418 [Page 14.]

[25] M. M. Davari, J. Jerrelind, and A. Stensson Trigell, "Energy efficiency analysis of a vehicle in modal and transient driving cycles including longitudinal and vertical dynamics," *Transportation Research Part D: Transport and Environment*, vol. 53, pp. 263–275, 2017. doi: https://doi.org/10.1016/j.trd.2017.04.019. [Online]. Available: https://www.sciencedirect.com/science/article/pii/S1361920917300287 [Page 14.]

[26] M. Davari, M. Jonasson, J. Jerrelind, A. Trigell, and L. Drugge, *Rolling loss analysis of combined camber and slip angle control*, 12 2016, pp. 713–716. ISBN 978-1-138-02992-7 [Page 14.]

[27] M. Davari, M. Jonasson, J. Jerrelind, and A. Stensson Trigell, "An energy oriented control allocation strategy for over-actuated road vehicles," 2017, (submitted for publication). [Page 14.]

[28] M. Davari, M. Jonasson, L. Drugge, J. Jerrelind, and A. Stensson Trigell, "Rolling loss optimisation of an over-actuated vehicle using predictive control of steering and camber actuators," 2017, (submitted for publication). [Page 14.]

[29] K. Yoshimura, M. Davari, L. Drugge, J. Jerrelind, and A. Trigell, "Studying road roughness effect on rolling resistance using brush tyre model and self-affine fractal surfaces," 01 2015. doi: 10.1201/b21185-31. ISBN 978-1-138-02885-2 [Page 14.]

[30] J. Brembeck and P. Ritzer, "Energy optimal control of an over actuated robotic electric vehicle using enhanced control allocation approaches," in *2012 IEEE Intelligent Vehicles Symposium*, 2012. doi: 10.1109/IVS.2012.6232147 pp. 322–327. [Pages 15, 33, and 36.]

[31] X. Jiang, L. Chen, X. Xu, Y. Cai, Y. Li, and W. Wang, "Analysis and optimization of energy efficiency for an electric vehicle with four independent drive in-wheel motors," *Advances in Mechanical Engineering*, vol. 10, p. 168781401876554, 03 2018. doi: 10.1177/1687814018765549 [Pages 15 and 33.]

[32] R. Wang, Y. Chen, D. Feng, X. Huang, and J. Wang, "Development and performance characterization of an electric ground vehicle with independently actuated in-wheel motors," *Journal of Power Sources*, vol. 196, no. 8, pp. 3962–3971, 2011. doi: https://doi.org/10.1016/j.jpowsour.2010.11.160. [Online]. Available: https://www.sciencedirect.com/science/article/pii/S037877531002152X [Pages 15 and 33.]

[33] A. Pennycott, L. De Novellis, A. Sabbatini, P. Gruber, and A. Sorniotti, "Reducing the motor power losses of a four-wheel drive, fully electric vehicle via wheel torque allocation," *Proceedings of the Institution of Mechanical Engineers, Part D: Journal of Automobile Engineering*, vol. 228, 06 2014. doi: 10.1177/0954407013516106 [Pages 15, 33, and 46.]

[34] H. Fujimoto, S. Egami, J. Saito, and K. Handa, "Range extension control system for electric vehicle based on searching algorithm of optimal front and rear driving force distribution," in *IECON 2012 - 38th Annual Conference on IEEE Industrial Electronics Society*, 2012. doi: 10.1109/IECON.2012.6389204 pp. 4264–4269. [Pages 15 and 33.]

[35] S. Koehler, A. Viehl, O. Bringmann, and W. Rosenstiel, "Energy-efficient torque distribution for axle-individually propelled electric vehicles," in *2014 IEEE Intelligent Vehicles Symposium Proceedings*, 2014. doi: 10.1109/IVS.2014.6856499 pp. 1109–1114. [Pages 15 and 33.]

[36] J. Gu, M. Ouyang, D. Lu, J. Li, and L. Lu, "Energy efficiency optimization of electric vehicle driven by in-wheel motors," 2013. doi: 10.1007/s12239-013-0084-1. ISSN 1976-3832 pp. 763–772. [Pages 15, 16, and 33.]

[37] B. Lenzo, G. De Filippis, A. M. Dizqah, A. Sorniotti, P. Gruber, S. Fallah, and W. De Nijs, "Torque Distribution Strategies for Energy-Efficient Electric Vehicles With Multiple Drivetrains," *Journal of Dynamic Systems, Measurement, and Control*, vol. 139, no. 12, 08 2017. doi: 10.1115/1.4037003 121004. [Online]. Available: https://doi.org/10.1115/1.4037003 [Pages 15, 16, and 46.]

[38] G. Rill, "Reducing the cornering resistance by torque vectoring," *Procedia Engineering*, vol. 199, pp. 3284–3289, 2017. doi: https://doi.org/10.1016/j.proeng.2017.09.393 X International

Conference on Structural Dynamics, EURODYN 2017. [Online]. Available: https://www.sciencedirect.com/science/article/pii/S1877705817338845 [Pages 16, 31, 41, and 70.]

[39] N. Sina, M. R. H. Yazdi, and V. Esfahanian, "A novel method to improve vehicle energy efficiency: Minimization of tire power loss," *Proceedings of the Institution of Mechanical Engineers, Part D: Journal of Automobile Engineering*, vol. 234, no. 4, pp. 1153–1166, 2020. doi: 10.1177/0954407019861241. [Online]. Available: https://doi.org/10.1177/0954407019861241 [Pages 16 and 31.]

[40] B. Zhao, N. Xu, H. Chen, K. Guo, and Y. Huang, "Stability control of electric vehicles with in-wheel motors by considering tire slip energy," *Mechanical Systems and Signal Processing*, vol. 118, pp. 340–359, 2019. doi: https://doi.org/10.1016/j.ymssp.2018.08.037. [Online]. Available: https://www.sciencedirect.com/science/article/pii/S0888327018305764 [Pages 16 and 46.]

[41] A. Erke, "Effects of electronic stability control (esc) on accidents: A review of empirical evidence," *Accident Analysis Prevention*, vol. 40, no. 1, pp. 167–173, 2008. doi: https://doi.org/10.1016/j.aap.2007.05.002. [Online]. Available: https://www.sciencedirect.com/science/article/pii/S0001457507000851 [Page 16.]

[42] A. Høye, "The effects of electronic stability control (esc) on crashes—an update," *Accident Analysis Prevention*, vol. 43, no. 3, pp. 1148–1159, 2011. doi: https://doi.org/10.1016/j.aap.2010.12.025. [Online]. Available: https://www.sciencedirect.com/science/article/pii/S0001457510004021 [Page 16.]

[43] R. Rajamani, *Vehicle Dynamics and Control*, 2nd ed., ser. Mechanical engineering series. New York, NY: Springer-Verlag, 2012. ISBN 1461414326 [Pages 16, 31, 32, 36, and 43.]

[44] X. Ding, Z. Wang, L. Zhang, and J. Liu, "A comprehensive vehicle stability assessment system based on enabling tire force estimation," *IEEE Transactions on Vehicular Technology*, vol. 71, no. 11, pp. 11 571–11 588, 2022. doi: 10.1109/TVT.2022.3193139 [Page 17.]

[45] W. Zhang, "Exploiting over-actuation for improved active safety of autonomous electric vehicles," Ph.D. dissertation, Royal Institute of Technology (KTH), Stockholm, Sweden, 05 2022. [Pages 17 and 41.]

[46] W. Zhang, Z. Wang, L. Drugge, and M. Nybacka, "Evaluating model predictive path following and yaw stability controllers for over-actuated autonomous electric vehicles," *IEEE Transactions on Vehicular Technology*, vol. 69, 10 2020. doi: 10.1109/TVT.2020.3030863 [Page 17.]

[47] W. Zhang, L. Drugge, M. Nybacka, and Z. Wang, "Active camber for enhancing path following and yaw stability of over-actuated autonomous electric vehicles," *Vehicle System Dynamics*, vol. 59, pp. 1–22, 02 2020. doi: 10.1080/00423114.2020.1723653 [Page 17.]

[48] T. Bächle, K. Graichen, M. Buchholz, and K. Dietmayer, "Vehicle dynamics control in challenging driving situations using nonlinear model predictive control allocation," in *2014 IEEE Conference on Control Applications (CCA)*, 2014. doi: 10.1109/CCA.2014.6981370 pp. 346–351. [Page 17.]

[49] M. Polesel, B. Shyrokau, M. Tanelli, D. Savitski, V. Ivanov, and A. Ferrara, "Hierarchical control of overactuated vehicles via sliding mode techniques," in *53rd IEEE Conference on Decision and Control*, 2014. doi: 10.1109/CDC.2014.7040026 pp. 4095–4100. [Page 17.]

[50] H. Alipour, M. Sabahi, and M. B. Bannae Sharifian, "Lateral stabilization of a four wheel independent drive electric vehicle on slippery roads," *Mechatronics*, vol. 30, pp. 275–285, 2015. doi: https://doi.org/10.1016/j.mechatronics.2014.08.006. [Online]. Available: https://www.sciencedirect.com/science/article/pii/S0957415814001275 [Page 17.]

[51] L. Zhai, T. Sun, and J. Wang, "Electronic stability control based on motor driving and braking torque distribution for a four in-wheel motor drive electric vehicle," *IEEE Transactions on Vehicular Technology*, vol. 65, no. 6, pp. 4726–4739, 2016. doi: 10.1109/TVT.2016.2526663 [Page 18.]

[52] M. Kissai, X. Mouton, B. Monsuez, and A. Tapus, "Extensible control architecture for over-actuated vehicles," in *2019 19th International Conference on Control, Automation and Systems (ICCAS)*, 2019. doi: 10.23919/ICCAS47443.2019.8971522 pp. 263–269. [Page 18.]

[53] T. Bächle, K. Graichen, M. Buchholz, and K. Dietmayer, "Slip-constrained model predictive control allocation for an all-wheel driven electric vehicle," *IFAC Proceedings Volumes*, vol. 47, no. 3, pp. 12 042–12 047, 2014. doi: https://doi.org/10.3182/20140824-6-ZA-1003.01287 19th IFAC World Congress. [Online]. Available: https://www.sciencedirect.com/science/article/pii/S1474667016435329 [Page 18.]

[54] B. Ren, H. Chen, H. Zhao, and L. Yuan, "Mpc-based yaw stability control in in-wheel-motored ev via active front steering and motor torque distribution," *Mechatronics*, vol. 38, pp. 103–114, 2016. doi: https://doi.org/10.1016/j.mechatronics.2015.10.002. [Online]. Available: https://www.sciencedirect.com/science/article/pii/S0957415815001622 [Page 18.]

[55] M. Jalali, A. Khajepour, S. ken Chen, and B. Litkouhi, "Integrated stability and traction control for electric vehicles using model predictive control," *Control Engineering Practice*, vol. 54, pp. 256–266, 2016. doi: https://doi.org/10.1016/j.conengprac.2016.06.005. [Online]. Available: https://www.sciencedirect.com/science/article/pii/S0967066116301265 [Page 18.]

[56] L. Yuan, H. Zhao, H. Chen, and B. Ren, "Nonlinear mpc-based slip control for electric vehicles with vehicle safety constraints," *Mechatronics*, vol. 38, pp. 1–15, 2016. doi: https://doi.org/10.1016/j.mechatronics.2016.05.006. [Online]. Available: https://www.sciencedirect.com/science/article/pii/S0957415816300356 [Page 18.]

[57] P. Falcone, H. E. Tseng, J. Asgari, F. Borrelli, and D. Hrovat, "Integrated braking and steering model predictive control approach in autonomous vehicles," *IFAC Proceedings Volumes*, vol. 40, no. 10, pp. 273–278, 2007. doi: https://doi.org/10.3182/20070820-3-US-2918.00038 5th IFAC Symposium on Advances in Automotive Control. [Online]. Available: https://www.sciencedirect.com/science/article/pii/S1474667015319364 [Page 18.]

[58] J. Wang and R. G. Longoria, "Coordinated and reconfigurable vehicle dynamics control," *IEEE Transactions on Control Systems Technology*, vol. 17, no. 3, pp. 723–732, 2009. doi: 10.1109/TCST.2008.2002264 [Page 18.]

[59] Z. Shuai, H. Zhang, J. Wang, J. Li, and M. Ouyang, "Lateral motion control for four-wheel-independent-drive electric vehicles using optimal torque allocation and dynamic message priority scheduling," *Control Engineering Practice*, vol. 24, pp. 55–66, 2014. doi: https://doi.org/10.1016/j.conengprac.2013.11.012. [Online]. Available: https://www.sciencedirect.com/science/article/pii/S0967066113002165 [Page 18.]

[60] ——, "Combined afs and dyc control of four-wheel-independent-drive electric vehicles over can network with time-varying delays," *IEEE Transactions on Vehicular Technology*, vol. 63, no. 2, pp. 591–602, 2014. doi: 10.1109/TVT.2013.2279843 [Page 18.]

[61] H. Jing, F. Jia, H. Liu, and J. Sun, "Multi-objective optimal control allocation for a four-wheel-independent-drive electric vehicle," in *2017 36th Chinese Control Conference (CCC)*, 2017. doi: 10.23919/ChiCC.2017.8028880 pp. 9543–9547. [Pages 19, 33, and 46.]

[62] H. Jing, F. Jia, and Z. Liu, "Multi-objective optimal control allocation for an over-actuated electric vehicle," *IEEE Access*, vol. 6, pp. 4824–4833, 2018. doi: 10.1109/ACCESS.2017.2788941 [Pages 19 and 46.]

[63] T. Bächle, K. Graichen, M. Buchholz, and K. Dietmayer, "Model predictive control allocation in electric vehicle drive trains," *IFAC-PapersOnLine*, vol. 48, no. 15, pp. 335–340, 2015. doi: https://doi.org/10.1016/j.ifacol.2015.10.048 4th IFAC Workshop on Engine and Powertrain Control, Simulation and Modeling E-COSM 2015. [Online]. Available: https://www.sciencedirect.com/science/article/pii/S2405896315019242 [Pages 19, 33, and 46.]

[64] J. Hu, J. Tao, F. Xiao, X. Niu, and C. Fu, "An optimal torque distribution control strategy for four-wheel independent drive electric vehicles considering energy economy," *IEEE Access*, vol. 7, pp. 141 826–141 837, 2019. doi: 10.1109/ACCESS.2019.2944479 [Pages 19 and 33.]

[65] D. Xia, B. Li, J. Zhang, B. Zhang, and N. Zhang, "Ecological cooperative adaptive cruise control of over-actuated electric vehicles with in-wheel motor in traffic flow," *IET Intelligent Transport Systems*, vol. 15, 06 2021. doi: 10.1049/itr2.12059 [Page 19.]

[66] Y. Chen and J. Wang, "Adaptive energy-efficient control allocation for planar motion control of over-actuated electric ground vehicles," *IEEE*

Transactions on Control Systems Technology, vol. 22, no. 4, pp. 1362–1373, 2014. doi: 10.1109/TCST.2013.2287560 [Page 19.]

[67] ——, "Fast and global optimal energy-efficient control allocation with applications to over-actuated electric ground vehicles," *IEEE Transactions on Control Systems Technology*, vol. 20, no. 5, pp. 1202–1211, 2012. doi: 10.1109/TCST.2011.2161989 [Page 19.]

[68] ——, "A global optimization algorithm for energy-efficient control allocation of over-actuated systems," in *Proceedings of the 2011 American Control Conference*, 2011. doi: 10.1109/ACC.2011.5990899 pp. 5300–5305. [Page 19.]

[69] ——, "Design and experimental evaluations on energy efficient control allocation methods for overactuated electric vehicles: Longitudinal motion case," *IEEE/ASME Transactions on Mechatronics*, vol. 19, no. 2, pp. 538–548, 2014. doi: 10.1109/TMECH.2013.2249591 [Page 19.]

[70] IPG Automotive, "IPG carmaker." [Online]. Available: https://ipg-automotive.com/en/products-solutions/software/carmaker/ [Pages 21 and 59.]

[71] M. CarMaker. Carmaker for simulink. Accessed: 18 Mar 2023. [Online]. Available: https://se.mathworks.com/products/connections/product_detail/carmaker.html [Page 21.]

[72] G. C. Pereira, "Lateral model predictive control for autonomous heavy-duty vehicles: Sensor, actuator, and reference uncertainties," Licentiate Thesis, Royal Institute of Technology (KTH), Stockholm, Sweden, 2020. [Page 26.]

[73] Y. Gao, A. Gray, J. V. Frasch, T. Lin, E. H. Tseng, J. K. Hedrick, and F. Borrelli, "Spatial predictive control for agile semi-autonomous ground vehicles," 2012. [Page 26.]

[74] S. Kamat, "Lane keeping of vehicle using model predictive control," in *2019 IEEE 5th International Conference for Convergence in Technology (I2CT)*, 2019. doi: 10.1109/I2CT45611.2019.9033958 pp. 1–6. [Page 26.]

[75] H. Guo, D. Cao, H. Chen, Z. Sun, and Y. Hu, "Model predictive path following control for autonomous cars considering a measurable

disturbance: Implementation, testing, and verification," *Mechanical Systems and Signal Processing*, vol. 118, pp. 41–60, 2019. doi: https://doi.org/10.1016/j.ymssp.2018.08.028. [Online]. Available: https://www.sciencedirect.com/science/article/pii/S0888327018305582 [Page 27.]

[76] R. Abousleiman and O. Rawashdeh, "Energy consumption model of an electric vehicle," in *2015 IEEE Transportation Electrification Conference and Expo (ITEC)*, 2015. doi: 10.1109/ITEC.2015.7165773 pp. 1–5. [Page 29.]

[77] H. Pacejka, *Tire and Vehicle Dynamics, 3rd Edition*. Morgan Kaufmann, 2012. ISBN 0080970168 [Page 30.]

[78] S. Sano, Y. Furukawa, and S. Shiraishi, "Four wheel steering system with rear wheel steer angle controlled as a function of sterring wheel angle," *SAE Transactions*, vol. 95, pp. 880–893, 1986. [Online]. Available: http://www.jstor.org/stable/44725442 [Page 37.]

[79] G. C. Pereira, L. Svensson, P. F. Lima, and J. Mårtensson, "Lateral model predictive control for over-actuated autonomous vehicle," in *2017 IEEE Intelligent Vehicles Symposium (IV)*, 2017. doi: 10.1109/IVS.2017.7995737 pp. 310–316. [Page 37.]

[80] D. Arnström. DAQP Webpage. Accessed: 27 Mar 2023. [Online]. Available: https://darnstrom.github.io/daqp/ [Pages 60 and 78.]

[81] ——, "DAQP Software." [Online]. Available: https://github.com/darnstrom/daqp [Pages 60 and 78.]

[82] K. Jiang, A. Pavelescu, A. Victorino, and A. Charara, "Estimation of vehicle's vertical and lateral tire forces considering road angle and road irregularity," in *17th International IEEE Conference on Intelligent Transportation Systems (ITSC)*, 2014. doi: 10.1109/ITSC.2014.6957714 pp. 342–347. [Page 71.]

[83] MathWorks. quadprog. Accessed: 4 Apr 2023. [Online]. Available: https://se.mathworks.com/help/optim/ug/quadprog.html [Page 78.]

[84] syscop, "acados." [Online]. Available: https://github.com/acados/acados [Page 78.]

[85] ——. acados Webpage. Accessed: 27 Mar 2023. [Online]. Available: https://docs.acados.org/embedded_workflow/index.html [Page 78.]

[86] MathWorks. legacy_code tool. Accessed: 3 Apr 2023. [Online]. Available: https://se.mathworks.com/help/simulink/slref/legacy_code.html [Page 79.]

Appendix A

RCV's engine efficiency characteristic

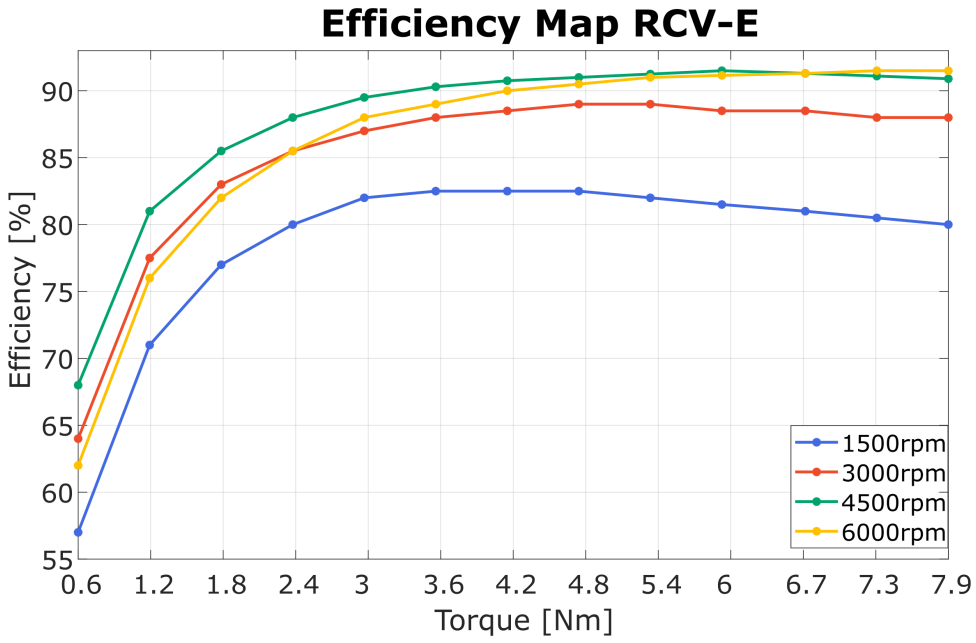

Figure A.1: RCV-E PMSM efficiency map.

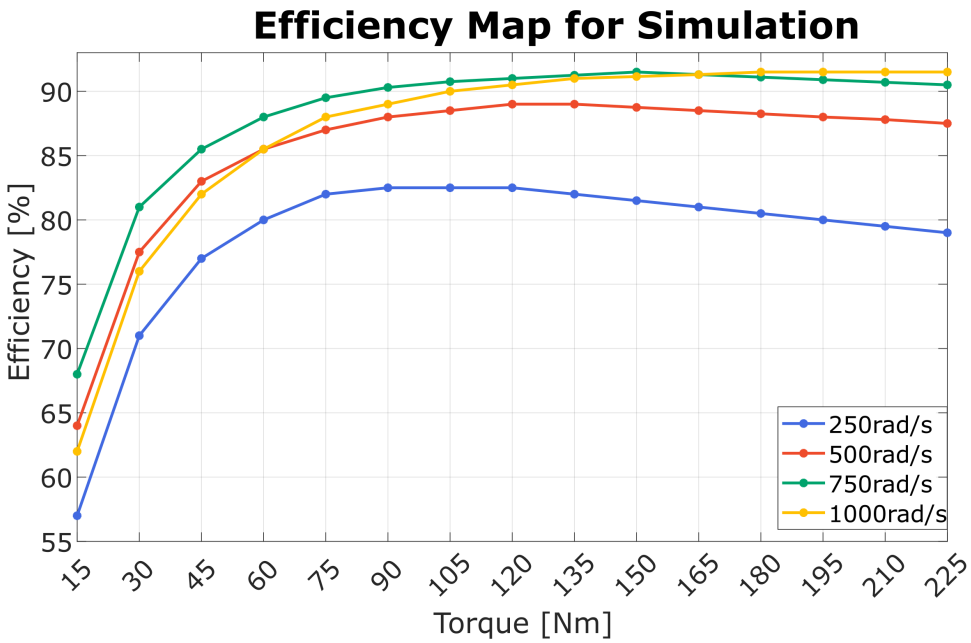

Figure A.2: Variation of the RCV-E engines efficiency map for the Tesla motors used in simulation.

Appendix B

LTV-MPC equations

In here, form the LTV-MPC's equations, the H and f matrices are derived such that they can be immediately implemented in any quadratic programming solver in the form:

$$\min_x \frac{1}{2} x^T H x + f^T x \tag{B.1}$$

Given the discrete-time nonlinear system:

$$\begin{cases} x(k+1) = f(x(k), u(k)) \\ y = g(x(k)) \end{cases} \tag{B.2}$$

At time $k-1$ the optimal control sequence has been computed:

$$\begin{aligned} &u^o(k-1 : k+N-2|k-1) = \\ &= [u^o(k-1|k-1), u^o(k|k-1), ..., u^o(k+N-2|k-1)] \end{aligned} \tag{B.3}$$

Now, at time k, consider the future control sequence:

$$\begin{aligned} &\bar{u}^o(k-1 : k+N-1|k-1) = \\ &= [u^o(k|k-1), ..., u^o(k+N-2|k-1), u^o(k+N-2|k-1)] \end{aligned} \tag{B.4}$$

Using this control sequence $\bar{u}^o$, the current state $\hat{x}(k)$, and the nonlinear model, it is possible to predict the state trajectory.

$$\hat{x}(k+i+1|k) = f(\hat{x}(k+i|k), \bar{u}^o(k+i|k-1)) \; i = 0, \; ... \, , N-1 \tag{B.5}$$

This predicted state trajectory is used to linearize the system.

Define

$$\begin{aligned}\tilde{\delta}\hat{x}(k+i|k) &= x(k+i) - \hat{x}(k+i|k)\\ \tilde{\delta}u(k+i|k-1) &= u(k+i) - \bar{u}^o(k+i|k-1)\end{aligned} \qquad i = 0,\ \dots, N-1 \tag{B.6}$$

Then

$$\begin{aligned}x(k+i+1) = f(\hat{x}(k+i|k), \bar{u}^o(k+i|k-1)) + \\ + A_{k+i}\tilde{\delta}\hat{x}(k+i|k) + B_{k+i}\tilde{\delta}u(k+i|k)\end{aligned}$$

$$\begin{aligned}A(k+i) &= \left.\frac{\delta f}{\delta x}\right|_{\substack{\hat{x}(k+i|k),\\ \bar{u}^o(k+i|k-1)}} \qquad B(k+i) = \left.\frac{\delta f}{\delta u}\right|_{\substack{\hat{x}(k+i|k),\\ \bar{u}^o(k+i|k-1)}}\\ C(k+i) &= \left.\frac{\delta g}{\delta x}\right|_{\substack{\hat{x}(k+i|k),\\ \bar{u}^o(k+i|k-1)}} \qquad i = 0,\ \dots, N-1\end{aligned} \tag{B.7}$$

Define

$$\begin{aligned}G_{k+i} = f(\hat{x}(k+i|k), u^o(k+i|k-1)) - \\ - (A_{k+i}\hat{x}(k+i|k) + B_{k+i}u^o(k+i|k)),\end{aligned} \qquad i = 0,\ \dots, N-1 \tag{B.8}$$

Then

$$\begin{aligned}x(k+i+1) &= A_{k+i}x(k+i) + B_{k+i}u(k+i) + G_{k+i}\\ y(k+i) &= C_{k+i}x(k+i) \qquad\qquad i = 0,\ \dots, N-1\end{aligned} \tag{B.9}$$

Now, we have to rewrite $y(k+i)$ as a function of the N inputs along the prediction horizon, $u(k+i)$ with $i = 0, ..., N-1$, and the current state at time k, $x(k)$.

$$
\begin{aligned}
y(k+1) &= C_{k+1}x(k+1) = C_{k+1}(A_k x(k) + B_k u(k) + G_k) = \\
&= C_{k+1}A_k x(k) + C_{k+1}B_k u(k) + C_{k+1}G_k
\end{aligned}
$$

$$
\begin{aligned}
y(k+2) &= C_{k+2}x(k+2) = \ ... \ = \\
&= C_{k+2}A_{k+1}A_k x(k) + \\
&+ [C_{k+2}A_{k+1}B_k,\ C_{k+2}B_{k+1}] \begin{bmatrix} u(k) \\ u(k+1) \end{bmatrix} + \\
&+ [C_{k+2}A_{k+1},\ C_{k+2}] \begin{bmatrix} G_k \\ G_{k+1} \end{bmatrix}
\end{aligned}
\tag{B.10}
$$

... and so on until $y(k+N)$.

To make the process more feasible from the code point of view, the output vector $Y(k)$ can be written in the matrix form as a function of the current state $x(k)$ and the input vector $U(k)$ as follows:

$$Y(k) = A_c\, x(k) + B_c\, U(k) + E_c\, G(k)$$

$$Y(k) = \begin{bmatrix} y(k+1) \\ y(k+2) \\ \vdots \\ y(k+N-1) \\ y(k+N) \end{bmatrix} \quad U(k) = \begin{bmatrix} u(k) \\ u(k+1) \\ \vdots \\ u(k+N-2) \\ u(k+N-1) \end{bmatrix} \quad G(k) = \begin{bmatrix} G_k \\ G_{k+1} \\ \vdots \\ G_{k+N-2} \\ G_{k+N-1} \end{bmatrix}$$

$$R(k) = \begin{bmatrix} r(k+1) \\ r(k+2) \\ \vdots \\ r(k+N-1) \\ r(k+N) \end{bmatrix} \quad A_c = \begin{bmatrix} C_{k+1}A_k \\ C_{k+2}A_{k+1}A_k \\ \vdots \\ C_{k+N-1}\sum_{i=0}^{N-2} A_{k+i} \\ C_{k+N}\sum_{i=0}^{N-1} A_{k+i} \end{bmatrix}$$

$$B_c = \begin{bmatrix} C_{k+1}B_k & 0 & \dots & 0 \\ C_{k+2}A_{k+1}B_k & C_{k+2}B_{k+1} & \dots & 0 \\ C_{k+3}A_{k+2}A_{k+1}B_k & C_{k+3}A_{k+2}B_{k+1} & \dots & 0 \\ \vdots & \vdots & \ddots & \vdots \\ C_{k+N}\sum_{i=1}^{N-1} A_{k+i}\, B_k & C_{k+N}\sum_{i=2}^{N-1} A_{k+i}\, B_{k+1} & \dots & C_{k+N}B_{k+N-1} \end{bmatrix}$$

$$E_c = \begin{bmatrix} C_{k+1} & 0 & 0 & \dots & 0 \\ C_{k+2}A_{k+1} & C_{k+2} & 0 & \dots & 0 \\ C_{k+3}A_{k+2}A_{k+1} & C_{k+3}A_{k+2} & C_{k+3} & \dots & 0 \\ \vdots & \vdots & \vdots & \ddots & \vdots \\ C_{k+N}\sum_{i=1}^{N-1} A_{k+i} & C_{k+N}\sum_{i=2}^{N-1} A_{k+i} & C_{k+N}\sum_{i=3}^{N-1} A_{k+i} & \dots & C_{k+N} \end{bmatrix} \tag{B.11}$$

The quadratic cost function becomes as follows:

$$J = [R(k) - Y(k)]^T Q_0 [R(k) - Y(k)] + U(k)^T R_0 U(k) \tag{B.12}$$

Minimizing J as a function of the control input $U(k)$, given the current state $x(k)$, the reference vector $R(k)$, and the matrices in Equation B.11, one obtains:

$$\begin{aligned}
&\min_{U(k)} J = \min_{U(k)} [R(k) - Y(k)]^T Q_0 \, [R(k) - Y(k)] + U(k)^T R_0 \, U(k) = \\
&= \ \ldots \ = \\
&= \min_{U(k)} 2 \, (x(k)^T A_c^T + G^T E_c^T - R(k)^T) \, Q_0 \, B_c \, U(k) \\
&\quad + U(k)^T (B_c^T \, Q_0 \, B_c^T + R_0) \, U(k)
\end{aligned} \tag{B.13}$$

Therefore, the matrices H and f in Equation B.1 are:

$$\begin{aligned}
H \ &= 2 \, (B_c^T Q_0 \, B_c + R_0) \\
f^T &= 2 \, (x(k)^T A_c^T + G^T E_c^T - R(k)^T) \, Q_0 \, B_c
\end{aligned} \tag{B.14}$$

Appendix C

Energy minimization strategy: full simulation results tables

Here, all the results of the simulations to assess the control strategy for energy minimization are reported. The tests consider the five maneuvers specified in Section 6.2, a)-e), for which the following power components are measured, and the energy is computed as the time integral of the power during the maneuvers.

1. The electric power requested by the engines.
2. The power lost in the motors, computed using the engine efficiency characteristic.
3. The mechanical power at the shaft of the four engines.
4. The power lost due to wheel slipping, computed according to Equation 3.15, only for positive longitudinal forces at the wheels F_x since braking is not considered.
5. The power lost due to wheel cornering, computed according to Equation 3.17.

The tests are performed to compare the cases when no energy minimization strategy is implemented (B), when only the vehicle's weight distribution on the wheels is considered (W), and when, in addition to weight distribution, also the engine efficiency optimization strategy is included (E).

Maneuver a)					
Th=2s, Ts=0.2s, N=10					
Case	**Elect. En**	**Eng. Loss**	**Mech. En**	**Slip loss**	**Cor. Res.**
B	2507.5 kJ	388.4 kJ	2119.1 kJ	83.61 kJ	74.64 kJ
W	2466.3 kJ	382.5 kJ	2083.8 kJ	52.62 kJ	68.39 kJ
E	2436.6 kJ	342.7 kJ	2094.0 kJ	62.81 kJ	69.01 kJ
Th=1.5s, Ts=0.15s, N=10					
Case	**Elect. En**	**Eng. Loss**	**Mech. En**	**Slip loss**	**Cor. Res.**
B	2580.7 kJ	393.9 kJ	2186.8 kJ	104.86 kJ	72.79 kJ
W	2542.0 kJ	390.3 kJ	2151.7 kJ	58.00 kJ	67.59 kJ
E	2502.7 kJ	349.7 kJ	2153.0 kJ	68.68 kJ	68.36 kJ
Th=1s, Ts=0.1s, N=10					
Case	**Elect. En**	**Eng. Loss**	**Mech. En**	**Slip loss**	**Cor. Res.**
B	2633.1 kJ	388.7 kJ	2244.4 kJ	165.09 kJ	79.84 kJ
W	2553.2 kJ	381.8 kJ	2171.4 kJ	63.19 kJ	71.02 kJ
E	2530.9 kJ	352.4 kJ	2178.5 kJ	70.93 kJ	71.57 kJ
Th=1.4s, Ts=0.2s, N=7					
Case	**Elect. En**	**Eng. Loss**	**Mech. En**	**Slip loss**	**Cor. Res.**
B	2471.2 kJ	382.9 kJ	2088.4 kJ	76.87 kJ	68.57 kJ
W	2439.4 kJ	382.8 kJ	2056.6 kJ	49.79 kJ	62.98 kJ
E	2406.7 kJ	340.4 kJ	2066.3 kJ	59.99 kJ	63.74 kJ
Th=1.5s, Ts=0.3s, N=5					
Case	**Elect. En**	**Eng. Loss**	**Mech. En**	**Slip loss**	**Cor. Res.**
B	2412.9 kJ	373.5 kJ	2039.4 kJ	59.38 kJ	62.77 kJ
W	2403.8 kJ	374.7 kJ	2029.1 kJ	46.38 kJ	58.72 kJ
E	2377.8 kJ	337.4 kJ	2040.4 kJ	58.51 kJ	59.75 kJ
Th=1s, Ts=0.2s, N=5					
Case	**Elect. En**	**Eng. Loss**	**Mech. En**	**Slip loss**	**Cor. Res.**
B	2470.5 kJ	378.8 kJ	2091.7 kJ	59.76 kJ	76.81 kJ
W	2471.2 kJ	384.0 kJ	2087.2 kJ	49.46 kJ	67.47 kJ
E	2443.0 kJ	344.5 kJ	2098.5 kJ	61.17 kJ	67.91 kJ

Table C.1: Energy consumed by the LTV-MPC with different combinations of the prediction horizon during Maneuver a). Three cases are reported: B) the base version with no energy minimization implementation, W) when only the vehicle's weight distribution is considered, E) when also the engine efficiency optimization is included.

Maneuver b)					
Th=2s, Ts=0.2s, N=10					
Case	**Elect. En**	**Eng. Loss**	**Mech. En**	**Slip loss**	**Cor. Res.**
B	1088.8 kJ	169.5 kJ	919.3 kJ	11.60 kJ	0.00 kJ
W	1088.5 kJ	169.3 kJ	919.1 kJ	11.50 kJ	0.00 kJ
E	1062.0 kJ	127.3 kJ	934.6 kJ	29.23 kJ	0.00 kJ
Th=1.5s, Ts=0.15s, N=10					
Case	**Elect. En**	**Eng. Loss**	**Mech. En**	**Slip loss**	**Cor. Res.**
B	1075.4 kJ	163.7 kJ	911.7 kJ	12.03 kJ	0.00 kJ
W	1075.1 kJ	163.5 kJ	911.6 kJ	11.91 kJ	0.00 kJ
E	1052.6 kJ	126.0 kJ	926.6 kJ	28.29 kJ	0.00 kJ
Th=1s, Ts=0.1s, N=10					
Case	**Elect. En**	**Eng. Loss**	**Mech. En**	**Slip loss**	**Cor. Res.**
B	1078.2 kJ	159.5 kJ	918.6 kJ	13.01 kJ	0.00 kJ
W	1078.1 kJ	159.6 kJ	918.5 kJ	12.86 kJ	0.00 kJ
E	1056.9 kJ	125.7 kJ	931.2 kJ	26.67 kJ	0.00 kJ
Th=1.4s, Ts=0.2s, N=7					
Case	**Elect. En**	**Eng. Loss**	**Mech. En**	**Slip loss**	**Cor. Res.**
B	1078.0 kJ	164.3 kJ	913.7 kJ	12.02 kJ	0.00 kJ
W	1082.4 kJ	165.8 kJ	916.6 kJ	11.82 kJ	0.00 kJ
E	1059.1 kJ	126.7 kJ	932.4 kJ	29.65 kJ	0.00 kJ
Th=1.5s, Ts=0.3s, N=5					
Case	**Elect. En**	**Eng. Loss**	**Mech. En**	**Slip loss**	**Cor. Res.**
B	1091.3 kJ	170.6 kJ	920.7 kJ	11.55 kJ	0.00 kJ
W	1090.9 kJ	170.4 kJ	920.6 kJ	11.45 kJ	0.00 kJ
E	1064.1 kJ	127.8 kJ	936.3 kJ	29.20 kJ	0.00 kJ
Th=1s, Ts=0.2s, N=5					
Case	**Elect. En**	**Eng. Loss**	**Mech. En**	**Slip loss**	**Cor. Res.**
B	1080.0 kJ	163.2 kJ	916.7 kJ	12.27 kJ	0.00 kJ
W	1079.7 kJ	163.0 kJ	916.6 kJ	12.14 kJ	0.00 kJ
E	1056.7 kJ	126.2 kJ	930.5 kJ	26.84 kJ	0.00 kJ

Table C.2: Energy consumed by the LTV-MPC with different combinations of the prediction horizon during Maneuver b). Three cases are reported: B) the base version with no energy minimization implementation, W) when only the vehicle's weight distribution is considered, E) when also the engine efficiency optimization is included.

Maneuver c)					
Th=2s, Ts=0.2s, N=10					
Case	**Elect. En**	**Eng. Loss**	**Mech. En**	**Slip loss**	**Cor. Res.**
B	1033.1 kJ	122.8 kJ	910.4 kJ	26.52 kJ	0.00 kJ
W	1031.6 kJ	123.0 kJ	908.6 kJ	24.49 kJ	0.00 kJ
E	1028.6 kJ	115.1 kJ	913.5 kJ	29.39 kJ	0.00 kJ
Th=1.5s, Ts=0.15s, N=10					
Case	**Elect. En**	**Eng. Loss**	**Mech. En**	**Slip loss**	**Cor. Res.**
B	1030.5 kJ	122.2 kJ	908.3 kJ	27.34 kJ	0.00 kJ
W	1028.8 kJ	122.5 kJ	906.3 kJ	25.09 kJ	0.00 kJ
E	1025.1 kJ	114.8 kJ	910.3 kJ	29.27 kJ	0.00 kJ
Th=1s, Ts=0.1s, N=10					
Case	**Elect. En**	**Eng. Loss**	**Mech. En**	**Slip loss**	**Cor. Res.**
B	1028.7 kJ	119.1 kJ	909.6 kJ	29.28 kJ	0.00 kJ
W	1026.7 kJ	119.5 kJ	907.2 kJ	26.68 kJ	0.00 kJ
E	1026.2 kJ	114.5 kJ	911.7 kJ	30.72 kJ	0.00 kJ
Th=1.4s, Ts=0.2s, N=7					
Case	**Elect. En**	**Eng. Loss**	**Mech. En**	**Slip loss**	**Cor. Res.**
B	1040.7 kJ	126.7 kJ	914.0 kJ	25.78 kJ	0.00 kJ
W	1041.0 kJ	128.6 kJ	912.3 kJ	23.28 kJ	0.00 kJ
E	1032.8 kJ	116.5 kJ	916.3 kJ	27.59 kJ	0.00 kJ
Th=1.5s, Ts=0.3s, N=5					
Case	**Elect. En**	**Eng. Loss**	**Mech. En**	**Slip loss**	**Cor. Res.**
B	1041.6 kJ	127.9 kJ	913.6 kJ	23.59 kJ	0.00 kJ
W	1040.8 kJ	128.2 kJ	912.6 kJ	22.16 kJ	0.00 kJ
E	1033.2 kJ	115.9 kJ	917.2 kJ	27.23 kJ	0.00 kJ
Th=1s, Ts=0.2s, N=5					
Case	**Elect. En**	**Eng. Loss**	**Mech. En**	**Slip loss**	**Cor. Res.**
B	1047.0 kJ	129.9 kJ	917.1 kJ	24.78 kJ	0.00 kJ
W	1045.8 kJ	130.2 kJ	915.6 kJ	22.95 kJ	0.00 kJ
E	1037.0 kJ	116.9 kJ	920.1 kJ	27.94 kJ	0.00 kJ

Table C.3: Energy consumed by the LTV-MPC with different combinations of the prediction horizon during Maneuver c). Three cases are reported: B) the base version with no energy minimization implementation, W) when only the vehicle's weight distribution is considered, E) when also the engine efficiency optimization is included.

Maneuver d)					
Th=2s, Ts=0.2s, N=10					
Case	**Elect. En**	**Eng. Loss**	**Mech. En**	**Slip loss**	**Cor. Res.**
B	1033.6 kJ	116.5 kJ	917.1 kJ	36.74 kJ	0.12 kJ
W	1033.3 kJ	118.8 kJ	914.5 kJ	32.54 kJ	0.05 kJ
E	1033.2 kJ	116.3 kJ	916.9 kJ	35.21 kJ	0.06 kJ
Th=1.5s, Ts=0.15s, N=10					
Case	**Elect. En**	**Eng. Loss**	**Mech. En**	**Slip loss**	**Cor. Res.**
B	1029.6 kJ	116.2 kJ	913.4 kJ	36.28 kJ	0.01 kJ
W	1028.8 kJ	118.5 kJ	910.3 kJ	32.27 kJ	0.01 kJ
E	1028.7 kJ	115.9 kJ	912.8 kJ	35.14 kJ	0.01 kJ
Th=1s, Ts=0.1s, N=10					
Case	**Elect. En**	**Eng. Loss**	**Mech. En**	**Slip loss**	**Cor. Res.**
B	1038.2 kJ	118.1 kJ	920.0 kJ	35.24 kJ	0.00 kJ
W	1037.6 kJ	120.5 kJ	917.0 kJ	31.46 kJ	0.00 kJ
E	1036.3 kJ	116.8 kJ	919.5 kJ	34.22 kJ	0.00 kJ
Th=1.4s, Ts=0.2s, N=7					
Case	**Elect. En**	**Eng. Loss**	**Mech. En**	**Slip loss**	**Cor. Res.**
B	1042.5 kJ	125.4 kJ	917.1 kJ	31.70 kJ	0.00 kJ
W	1046.2 kJ	130.0 kJ	916.2 kJ	28.01 kJ	0.00 kJ
E	1038.1 kJ	118.3 kJ	919.8 kJ	32.00 kJ	0.00 kJ
Th=1.5s, Ts=0.3s, N=5					
Case	**Elect. En**	**Eng. Loss**	**Mech. En**	**Slip loss**	**Cor. Res.**
B	1044.7 kJ	125.1 kJ	919.6 kJ	31.35 kJ	0.00 kJ
W	1044.7 kJ	127.5 kJ	917.1 kJ	28.22 kJ	0.00 kJ
E	1038.6 kJ	117.6 kJ	921.0 kJ	32.56 kJ	0.00 kJ
Th=1s, Ts=0.2s, N=5					
Case	**Elect. En**	**Eng. Loss**	**Mech. En**	**Slip loss**	**Cor. Res.**
B	1039.0 kJ	126.2 kJ	912.8 kJ	30.19 kJ	0.00 kJ
W	1039.0 kJ	128.7 kJ	910.4 kJ	27.23 kJ	0.00 kJ
E	1032.3 kJ	117.2 kJ	915.1 kJ	32.48 kJ	0.00 kJ

Table C.4: Energy consumed by the LTV-MPC with different combinations of the prediction horizon during Maneuver d). Three cases are reported: B) the base version with no energy minimization implementation, W) when only the vehicle's weight distribution is considered, E) when also the engine efficiency optimization is included.

Maneuver e)					
Th=2s, Ts=0.2s, N=10					
Case	**Elect. En**	**Eng. Loss**	**Mech. En**	**Slip loss**	**Cor. Res.**
B	199.5 kJ	73.5 kJ	126.0 kJ	0.75 kJ	80.59 kJ
W	156.1 kJ	55.8 kJ	100.3 kJ	0.17 kJ	55.32 kJ
E	136.9 kJ	35.4 kJ	101.4 kJ	0.47 kJ	56.01 kJ
Th=1.5s, Ts=0.15s, N=10					
Case	**Elect. En**	**Eng. Loss**	**Mech. En**	**Slip loss**	**Cor. Res.**
B	197.5 kJ	72.9 kJ	124.6 kJ	0.70 kJ	79.28 kJ
W	154.0 kJ	55.5 kJ	98.6 kJ	0.16 kJ	54.90 kJ
E	134.7 kJ	35.3 kJ	99.4 kJ	0.45 kJ	55.60 kJ
Th=1s, Ts=0.1s, N=10					
Case	**Elect. En**	**Eng. Loss**	**Mech. En**	**Slip loss**	**Cor. Res.**
B	196.4 kJ	72.6 kJ	123.7 kJ	0.69 kJ	78.10 kJ
W	153.7 kJ	55.4 kJ	98.2 kJ	0.16 kJ	54.60 kJ
E	134.5 kJ	35.3 kJ	99.2 kJ	0.44 kJ	55.27 kJ
Th=1.4s, Ts=0.2s, N=7					
Case	**Elect. En**	**Eng. Loss**	**Mech. En**	**Slip loss**	**Cor. Res.**
B	197.1 kJ	73.0 kJ	124.1 kJ	0.65 kJ	74.81 kJ
W	158.2 kJ	56.8 kJ	101.4 kJ	0.17 kJ	52.42 kJ
E	138.4 kJ	35.9 kJ	102.5 kJ	0.48 kJ	53.07 kJ
Th=1.5s, Ts=0.3s, N=5					
Case	**Elect. En**	**Eng. Loss**	**Mech. En**	**Slip loss**	**Cor. Res.**
B	190.7 kJ	71.0 kJ	119.7 kJ	0.54 kJ	71.30 kJ
W	160.4 kJ	57.4 kJ	103.0 kJ	0.18 kJ	51.10 kJ
E	140.4 kJ	36.0 kJ	104.4 kJ	0.50 kJ	51.69 kJ
Th=1s, Ts=0.2s, N=5					
Case	**Elect. En**	**Eng. Loss**	**Mech. En**	**Slip loss**	**Cor. Res.**
B	185.4 kJ	69.0 kJ	116.4 kJ	0.48 kJ	66.25 kJ
W	156.1 kJ	56.7 kJ	99.4 kJ	0.16 kJ	50.17 kJ
E	136.2 kJ	35.8 kJ	100.4 kJ	0.45 kJ	50.70 kJ

Table C.5: Energy consumed by the LTV-MPC with different combinations of the prediction horizon during Maneuver e). Three cases are reported: B) the base version with no energy minimization implementation, W) when only the vehicle's weight distribution is considered, E) when also the engine efficiency optimization is included.